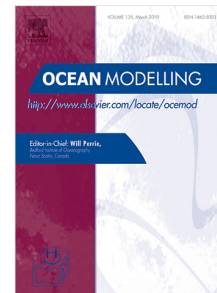


Journal Pre-proof

An assessment of the Indian Ocean mean state and seasonal cycle in a suite of interannual CORE-II simulations

H. Rahaman, U. Srinivasu, S. Panickal, J.V. Durgadoo, S.M. Griffies, M. Ravichandran, A. Bozec, A. Cherchi, A. Voldoire, D. Sidorenko, E.P. Chassignet, G. Danabasoglu, H. Tsujino, K. Getzlaff, M. Ilicak, M. Bentsen, M.C. Long, P.G. Fogli, R. Farneti, S. Danilov, S.J. Marsland, S. Valcke, S.G. Yeager, Q. Wang



PII: S1463-5003(19)30111-8
DOI: <https://doi.org/10.1016/j.ocemod.2019.101503>
Reference: OCEMOD 101503

To appear in: *Ocean Modelling*

Received date: 2 April 2019
Revised date: 11 October 2019
Accepted date: 14 October 2019

Please cite this article as: H. Rahaman, U. Srinivasu, S. Panickal et al., An assessment of the Indian Ocean mean state and seasonal cycle in a suite of interannual CORE-II simulations. *Ocean Modelling* (2019), doi: <https://doi.org/10.1016/j.ocemod.2019.101503>.

This is a PDF file of an article that has undergone enhancements after acceptance, such as the addition of a cover page and metadata, and formatting for readability, but it is not yet the definitive version of record. This version will undergo additional copyediting, typesetting and review before it is published in its final form, but we are providing this version to give early visibility of the article. Please note that, during the production process, errors may be discovered which could affect the content, and all legal disclaimers that apply to the journal pertain.

© 2019 Published by Elsevier Ltd.

1 **An assessment of the Indian Ocean mean state and seasonal cycle**
2 **in a suite of interannual CORE-II simulations**

3 H.Rahaman^{a*}, U.Srinivasu^a, S.Panickal^b, J.V.Durgadoo^c, S.M. Griffies^d, M.Ravichandran^e, A.
4 Bozec^f, A. Cherchi^{g,q}, A. Voltaire^h, D. Sidorenkoⁱ, E.P. Chassignet^f, G. Danabasoglu^j, H.
5 Tsuji^k, K. Getzlaff^c, M. Ilicak^l, M.Bentsen^m, M.C. Long^j, P.G. Fogli^e, R. Farnetiⁿ, S.Danilovⁱ,
6 S.J. Marsland^o, S. Valcke^p, S.G. Yeager^j, Q. Wangⁱ

7 a Indian National Centre for Ocean Information Services (INCOIS), Hyderabad, India

8 b Centre for Climate Change Research, Indian Institute of Tropical Meteorology
9 (IITM), Pune, India

10 c GEOMAR Helmholtz Centre for Ocean Research Kiel, Kiel, Germany

11 d NOAA Geophysical Fluid Dynamics Laboratory (GFDL) and Princeton University
12 Atmospheric and Oceanic Sciences Program, Princeton, USA.

13 e National Centre for Polar and Ocean Research (NCPOR) Goa, India.

14 f Center for Ocean-Atmospheric Prediction Studies (COAPS), Florida State University,
15 Tallahassee, FL, USA

16 g Fondazione Centro Euro-Mediterraneo sui Cambiamenti Climatici, Bologna, Italy

17 h Centre National de Recherches Météorologiques (CNRM-GAME), Toulouse, France.

18 i Alfred Wegener Institute (AWI) for Polar and Marine Research, Bremerhaven, Germany

19 j National Center for Atmospheric Research, Boulder, USA

20 k Meteorological Research Institute (MRI), Japan Meteorological Agency, Tsukuba, Japan

21 l Eurasia Institute of Earth Sciences, Istanbul Technical University, Istanbul, Turkey.

22 m University of Bergen, Bergen, Norway

23 n International Centre for Theoretical Physics (ICTP), Trieste, Italy.

24 o CSIRO Climate Science Centre, Aspendale, Australia

25 p Centre Européen de Recherche et de Formation Avancée en Calcul Scientifique (CERFACS),
26 URA 1875, CNRS/INSU, Toulouse, France

27 q Istituto Nazionale di Geofisica e Vulcanologia, Bologna, Italy

28
29
30
31
32
33 *Corresponding Author
34
35

36

Abstract

37 We present an analysis of annual and seasonal mean characteristics of the Indian Ocean
38 circulation and water masses from 16 global ocean-sea-ice model simulations that follow the
39 Coordinated Ocean-ice Reference Experiments (CORE) interannual protocol (CORE-II). All
40 simulations show a similar large-scale tropical current system, but with differences in the
41 Equatorial Undercurrent. Most CORE-II models simulate the structure of the Cross Equatorial
42 Cell (CEC) in the Indian Ocean. We uncover a previously unidentified secondary pathway of
43 northward cross-equatorial transport along 75 °E, thus complementing the pathway near the
44 Somali Coast. This secondary pathway is most prominent in the models which represent
45 topography realistically, thus suggesting a need for realistic bathymetry in climate models. When
46 probing the water mass structure in the upper ocean, we find that the salinity profiles are closer
47 to observations in geopotential (level) models than in isopycnal models. More generally, we find
48 that biases are model dependent, thus suggesting a grouping into model lineage, formulation of
49 the surface boundary, vertical coordinate and surface salinity restoring. Refinement in model
50 horizontal resolution (one degree versus ¼ degree) does not significantly improve simulations,
51 though there are some marginal improvements in the salinity and barrier layer results. The results
52 in turn suggest that a focus on improving physical parameterizations (e.g. boundary layer
53 processes) may offer more near-term advances in Indian Ocean simulations than refined grid
54 resolution.

55

56

57

58

59

60

61

62

63

64 1. Introduction

65 The tropical Indian Ocean covers the largest part of the warm pool in the global ocean
66 apart from the west Pacific. It is a key ingredient in the Asian monsoons, which are a lifeline for
67 billions of people in the rim countries (Webster et al., 1998). The Indian Ocean has unique
68 features compared to the Pacific and Atlantic Oceans. Most notably, it is bounded to the north by
69 the Asian continent, thus preventing the northward export of heat into the extratropical region
70 (between 30 and 60 °N). This geographical constraint leads to a basin-wide meridional
71 overturning circulation (MOC) (a full list of abbreviations is presented in the appendix) and a
72 corresponding transport of heat and mass that play a distinctive role in variability of the global
73 climate system (Chirokova and Webster, 2006). Schott and McCreary (2001) and then Schott et
74 al. (2009) provided systematic reviews of Indian Ocean circulation. In particular, Schott et al.
75 (2009) noted that much of the literature pertaining to simulations of the Indian Ocean is focused
76 on specific aspects rather than unifying across the range of features. They also pointed out that
77 one hindrance to progress is that existing models are deficient in a number of ways, such as the
78 existence of spurious convective overturning, enhanced numerical mixing, and unrealistic
79 horizontal diffusion. If subsurface mixing is not adequately parameterized, the simulated
80 thermocline becomes too diffuse. This error affects the temperature of the water that upwells and
81 hence the sea surface temperature (SST).

82
83 During recent years, increases in observational data have been available under the Indian
84 Ocean observing system IndOOS program (<http://www.clivar.org/clivar-panels/indian/IndOOS>).
85 This is a sustained observing system operated and supported by various national agencies and
86 coordinated internationally through the Climate Variability and Predictability
87 (CLIVAR)/Intergovernmental Oceanographic Commission (IOC)-Global Ocean Observing
88 System (GOOS) Indian Ocean Regional Panel. Unlike for the observations, a comprehensive
89 analysis of the basin-scale oceanographic features from a suite of ocean models for the Indian
90 Ocean has not been documented. The historical simulations using a suite of 16 global ocean-ice
91 models forced by the Coordinated Ocean Reference Experiments (CORE-II) provide an
92 opportunity to study the dynamics of Indian Ocean under a coordinated modeling framework.

93 This manuscript endeavors to describe and evaluate the mean state and seasonal variations of
94 important oceanographic features such as the SST, Sea Surface Salinity (SSS), currents,
95 thermocline and barrier layer (BL). We do so with a suite of 16 state-of-the-art global ocean/sea-
96 ice model simulations with bulk formula based boundary forcing generated from the same
97 atmospheric state. There are examples of a number of successful inter-comparison activities for
98 the Pacific, Atlantic, Arctic, and Southern Oceans (Tseng et al., 2017; Danabasoglu et al., 2014,
99 2016; Farneti et al., 2015; Ilicak et al., 2016). However, such coordinated modeling efforts have
100 generally been lacking for the Indian Ocean. We therefore aim here at assessing the simulations
101 from forced global ocean models for the Indian Ocean.

102
103 SST is one of the most important parameters for the evolution and prediction of the
104 Indian Summer Monsoon Rainfall (ISMR) as it represents the integrated ocean response to the
105 atmosphere in terms of various feedbacks (Sahai et al., 2007; Rajeevan et al., 2007, 2012; Yang
106 et al., 2007). Accurate simulations of Indian Ocean SST are challenging given the wide variety
107 of intraseasonal, seasonal and interannual variability (Schott et al., 2001, 2009). In addition to
108 variability intrinsic to the Indian Ocean, there are impacts from *El Niño* Southern Oscillation
109 (ENSO) that connect from the Pacific Ocean (Annamalai et al., 2005). In the North Indian Ocean
110 (NIO hereafter), ENSO affects SST variability through an atmospheric bridge that changes
111 cloud cover and thus modifies surface heat fluxes (e.g., Klein et al., 1999; Murtugudde and
112 Busalacchi, 1999). Over the southwestern Indian Ocean, ENSO forced SST variability arises
113 from oceanic Rossby waves generated by anomalous easterly winds that propagate from the east
114 (e.g. Xie et al., 2002; Huang and Kinter, 2002). Errors in simulated Indian Ocean SST adversely
115 affect the ability of coupled prediction models to accurately forecast ISMR (Chowdary et al.,
116 2015, 2016; Chaudhari et al., 2013; Levine and Turner, 2012). The CORE-II simulations do not
117 use explicit relaxation to observed SST. However, since air temperature is specified as part of the
118 CORE-II atmospheric state, there is an effective restoring flux (Haney, 1971; Murtugudde and
119 Busalacchi, 1999; Griffies et al., 2009). Hence, the CORE-II simulations are more constrained
120 than coupled climate models. Our analysis of CORE-II SST biases thus offers a means to

121 determine that portion of the coupled climate model errors that can be attributed to ocean
122 components.

123
124 SSS and subsurface salinities strongly affect the surface buoyancy and hence the surface
125 and subsurface water mass structures (Weller and Anderson, 1988; Murtugudde et al., 1998).
126 Salinity can thus have a strong influence on the thermodynamic structure of the mixed layer,
127 thermocline and their interactions (Mignot, et al., 2007). Apart from rainfall, salinity
128 distributions in the Indian Ocean are driven by river inflows, especially in the Bay of Bengal
129 (BoB) which receives nearly as much riverine input as rainfall (e.g., Shetye et al., 1996; Howden
130 and Murtugudde 2001; Vinayachandran et al., 2002; Sengupta et al., 2006). The influx of
131 freshwater (FW) through the Indonesian through flow (ITF), and the influx of saltier water from
132 the Persian Gulf and Red Sea also imprint clear signatures on the dynamics and thermodynamics
133 of the Indian Ocean (Murtugudde et al., 1998; Gordon et al., 2010; Gordon and Fine, 1996;
134 McCreary et al., 2001; McCreary et al., 1993; Bray et al., 1997). Many Indian Ocean modelling
135 studies use regional configurations with closed (sponge) boundaries at the east and south (Kurian
136 and Vinayachandran, 2007; Han et al., 2001; Han and McCreary, 2001), often leading to
137 unrealistic salinity properties. Similarly, better representation of BoB freshwater influx is
138 essential for studying the salinity distribution (Sitz et al., 2017). The near surface salinity
139 distribution study by Zhang and Marotzke (1999) using a model configured with open
140 boundaries showed an unrealistic local minimum of salinity in the north- western BoB due to the
141 lack of inclusion of runoff from Ganges and Brahmaputra. The freshwater forcing affects mixed
142 layer depths and surface currents which can advect the freshwater input away from the rivers
143 (Howden and Murtugudde, 2001; Sengupta et al., 2006; Han et al., 2001). Rahaman et al. (2014)
144 showed an improvement in SSS simulations with a nested regional model with salinity bias less
145 than 1 psu in the northern BoB. However, coupled models still show large biases (~ 1.5 psu) over
146 the BoB as well as the NIO (Vinayachandran and Nanjundiah, 2009; Fathrio et al., 2017b). In
147 general, the subsurface salinity bias in models is not documented for the Indian Ocean from a
148 suite of global model simulations. In this study apart from surface salinity we also evaluated the
149 subsurface salinity from the suite of 16 model simulations.

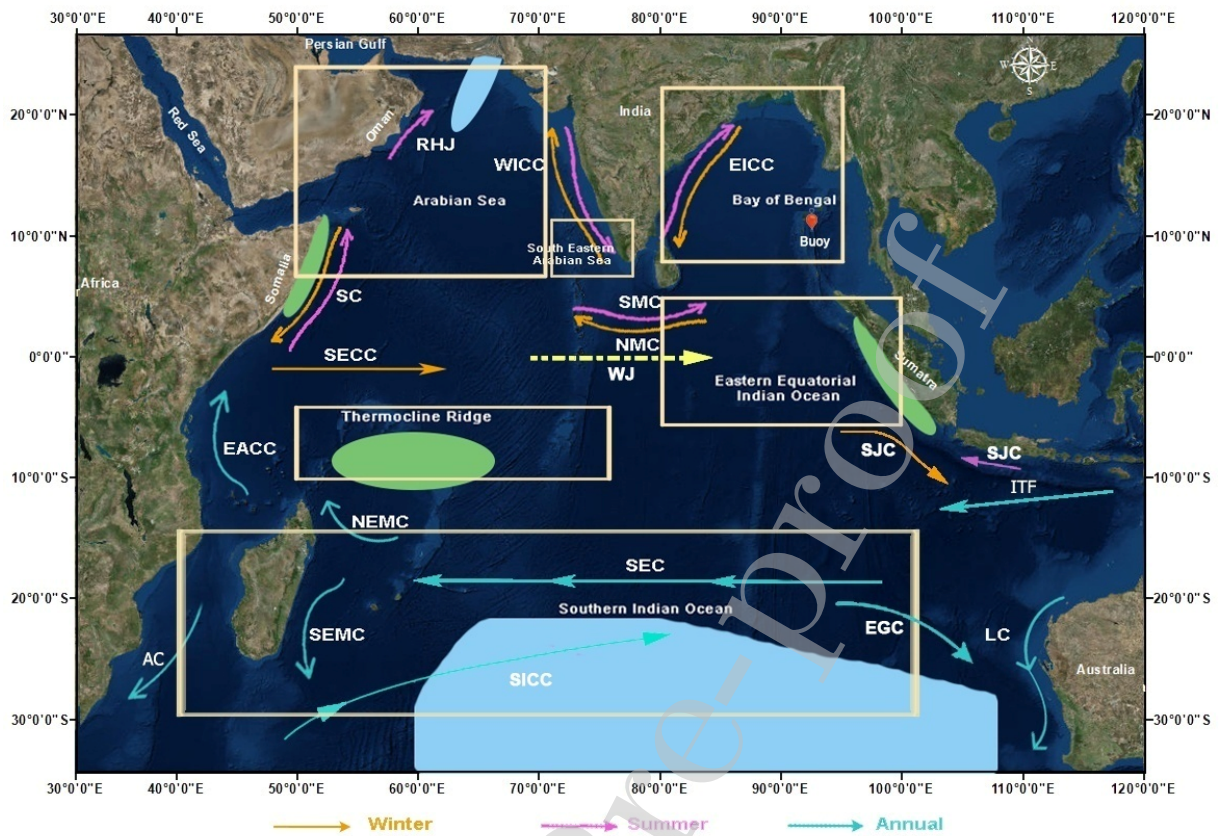
150 The Indian Ocean circulation is dominated by the dramatic seasonally reversing monsoon
151 winds (e.g. Webster et al., 1998). The low-latitude landmass of the Indian subcontinent drives
152 the strong monsoon, thus causing ocean currents and winds to seasonally reverse in the north
153 Indian Ocean (Gadgil et al., 2005; Gadgil, 2003; Schott et al., 2009). Seasonally reversing
154 monsoon winds (southwesterly during summer and northeasterly during winter) give rise to
155 seasonally reversing current systems in the NIO. The semi-annual cycle in the Indian Ocean is
156 also related to the seasonally reversing monsoonal winds. Figure 1a provides a schematic of the
157 horizontal circulation patterns in the Indian Ocean, including the circulations forced by the Asian
158 monsoon. The major NIO current systems exhibiting a reversal in direction with the monsoons
159 (see Figure 1a) include the Somali current (SC), Southwest and Northeast Monsoon Currents
160 (SMC and NMC), West India Coastal current (WICC), and East India Coastal current (EICC).
161 Though the Indian Ocean does not possess an equatorial upwelling system similar to the Pacific
162 or Atlantic, major upwelling regions do occur off the coast of Somalia and Sumatra in the north
163 and southeastern equatorial Indian Ocean, respectively (green shaded portions of Figure 1a).
164 Another unique feature is the open ocean upwelling dome or Seychelles Dome in the southwest
165 of the Indian Ocean. Satellite color images clearly reveal the existence of an open ocean
166 upwelling zone between 5 °S to 12 °S over the southwest Indian Ocean (Xie et al. 2002). The
167 north and south current systems are separated around 10–12 °S by a nearly zonal annually
168 prevailing South Equatorial Current (SEC). The zonal structure of the SEC is maintained by the
169 zero-wind stress curl around 10 °S, which is a consequence of the annually prevailing
170 southeasterly winds to the south of 10 °S and the seasonally reversing monsoon winds to the
171 north. This SEC plays a fundamental role in transporting warm and fresh western Pacific waters
172 westward across the Indian Ocean through ITF. The SEC after reaching to the northern tip of
173 Madagascar bifurcates into the Northeast and Southeast Madagascar Current (SEMC and
174 NEMC) (e.g. Chen et al. (2014) and Yamagami and Tozuka (2015)). The SEMC feeds into the
175 Agulhas Current (AC), which is part of the anticyclonic subtropical gyre similar to those in other
176 ocean basins. However, unlike other basins, this western boundary current overshoots the
177 southern extent of the African continent, with a portion extending westward into the South
178 Atlantic Ocean (a.k.a. Agulhas leakage), and a portion retroflecting and flowing eastward along

179 the equatorward edge of the Antarctic Circumpolar Current (Lutjeharms, 2006). The Leeuwin
180 Current (Waite et al., 2007) is an eastern boundary current along the west coast of Australia.
181 Interestingly, its southward flow is counter to what is expected from the predominant winds.
182 Along the eastern boundary at low latitudes, the Indian Ocean receives additional heat and mass
183 from the Pacific Ocean through the ITF (Godfrey, 1996; Gordon and Fine 1996; Murtugudde et
184 al., 1998). The ITF allows the water from the Pacific Ocean to reach the Indian Ocean. These
185 waters are then transported westward across the Indian Ocean by the westward-flowing SEC. In
186 the southern tip of Madagascar, the SEMC breaks into a series of dipole eddies that propagate
187 downstream into the Agulhas Current system and enters the Atlantic Ocean south of South
188 Africa (Han et al., 2014; Durgadoo et al., 2017; Nauw et al., 2008; Palastanga et al., 2006;
189 Ponsoni et al., 2016; Ridderinkhof et al., 2013). Some part of this water then retroreflects eastward
190 back into the Southern Indian Ocean (SIO) to feed the [South Indian Ocean Counter Current](#)
191 (SICC) (Palastanga et al., 2007; Siedler et al., 2009). In this study we show how the CORE-II
192 models are able to simulate these circulation features with respect to observations.

193
194 In addition to the annual monsoonal cycle, the circulation varies semiannually along the
195 equator with a strong [surface](#) eastward current named Wyrтки jet (WJ; Wyrтки, 1973). WJ appears
196 as a narrow band trapped within 2 °- 3 ° of the equator during the two transition periods of
197 monsoons (April-May and October-[November](#)) driven by the equatorial westerly winds. This WJ
198 [plays](#) an important role in the large-scale heat and freshwater transports in the tropical Indian
199 Ocean (Wyrтки, 1973; Reverdin, 1985; Schott and McCreary, 2001; Schott et al., 2009). The
200 subsurface currents also show seasonal variations in the equatorial Indian Ocean. Observations
201 show the presence of subsurface Equatorial Undercurrent (EUC), which is reported in various
202 studies (e.g., Knox, 1976, 1981; Reppin et al., 1999; Schott and McCreary, 2001; Iskandar et al.,
203 2009). In the Pacific and Atlantic Oceans the EUC is a quasi-permanent feature because of the
204 prevailing easterly trade winds (Philander, 1973; Philander and Pacanowski, 1980; McPhaden,
205 1986; Seidel and Giese, 1999). In the equatorial Indian Ocean, however, it is transient and
206 depends on winds and pressure gradient variations associated with the distinct seasonal cycle due
207 to the Asian monsoon. It is most pronounced in Northern Hemisphere winter (Iskandar et al.,

208 2009), with its presence and absence mainly determined by the weaker and stronger easterlies in
209 late winter and early spring (Cane, 1980; Reppin et al., 1999). The EUC is also present during
210 the southwest monsoon (Reppin et al., 1999). It is associated with equatorial waves driven by the
211 strong seasonally varying surface winds (Schott and McCreary, 2001). The core of this eastward
212 undercurrent is located in the thermocline region above 300 m, beneath which a weak westward
213 counter-flow exists and can last for at least a month during winter and spring. Observations show
214 that the magnitude of the eastward undercurrent can exceed 1.2 m/s during March-June and is
215 comparable to the Pacific Ocean undercurrent magnitude (Swallow, 1964, 1967). Previous
216 studies show that forced model simulations are able to capture the undercurrent reasonably well
217 (Iskandar et al., 2009; Chen et al., 2015). A comprehensive evaluation of how WJ and EUC are
218 represented in global models is still lacking. In this study, we also assessed in detail about how
219 the CORE-II models perform in simulating them.

220



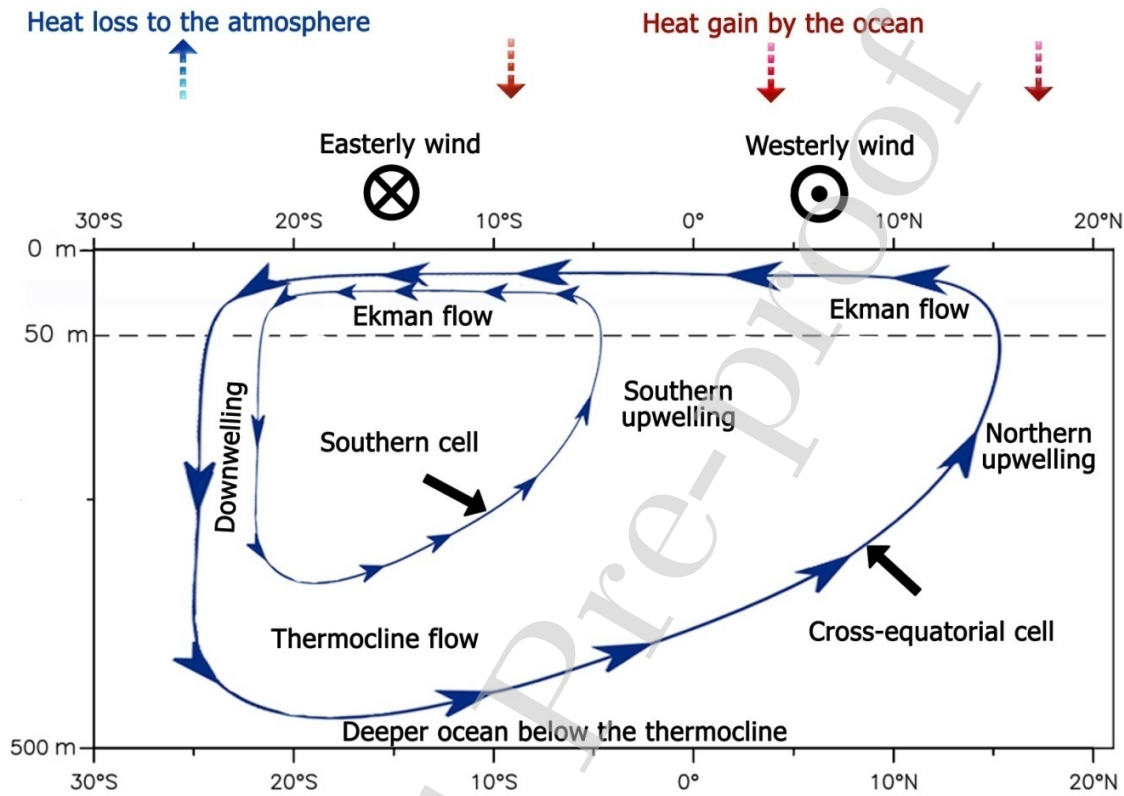
221

222 Figure 1a: Schematic representation of identified current branches over north Indian Ocean
 223 during summer (JJA: pink), winter (DJF: orange) and as annual mean (cyan). Current branches
 224 are the South Equatorial Current (SEC), South Equatorial Countercurrent (SECC), Northeast and
 225 Southeast Madagascar Current (NEMC and SEMC), East African Coastal Current (EACC),
 226 Somali Current (SC), Ras-al-Hadd Jet (RHJ), East India Coastal Current (EICC), West India
 227 Coastal Current (WICC), Southwest and Northeast Monsoon Currents (SMC and NMC), the
 228 Wyrski Jet (WJ), Leeuwin Current (LC), Agulhas Current (AC), South Indian Ocean Counter
 229 Current (SICC), Eastern Gyral Current (EGC), South Java Current (SJC) and Indonesian
 230 Through Flow (ITF). Upwelling and subduction zones are shown in green and blue shades,
 231 respectively. The buoy location at 94°E and 10.5°N is shown as a red dot in the Bay of Bengal.
 232 The different sub-regions used for the time series comparison are evidenced as light-yellow

233 color boxes, and they corresponds to Arabian Sea (AS), Bay of Bengal, South Eastern Arabian
 234 Sea, Eastern Equatorial Indian Ocean, Thermocline Ridge and Southern Indian Ocean.

235

236



237

238

239 Figure 1b: Conceptual illustration of the time-mean meridional overturning circulation of the
 240 upper Indian Ocean (first 500 m) consisting of a southern and a cross-equatorial cell (Based on
 241 Lee, 2004).

242

243 Apart from the surface circulations and equatorial currents discussed in the previous
 244 paragraphs, two cells are active in the Indian Ocean: the cross-equatorial cell (CEC) and the
 245 southern subtropical cell (SSTC) (Lee, 2004; Schott et al., 2004). The CEC is a shallow (~500
 246 m) meridional overturning circulation, consisting of the northward flow of southern-hemisphere
 247 thermocline water, upwelling in the northern hemisphere, and a return flow of surface water

248 (Miyama et al., 2003). A schematic of the meridional circulation of the Indian Ocean in the
249 upper ocean (0-500 m) is given in Figure 1b (from Lee, 2004). The upper Indian Ocean heat
250 balance is achieved by CEC and SSTC (Miyama et al., 2003; Schott et al., 2004). The CEC
251 connects upwelling zones in the NIO to subduction zones in the southeastern Indian Ocean via a
252 southward, cross-equatorial branch concentrated in the upper 50 m and a northward bulk-flow of
253 cooler thermocline water. Miyama et al. (2003) have shown that the sources of water for the
254 subsurface branch of the cross equatorial cell are the subduction zones in the southeastern Indian
255 Ocean, the ITF, and flow into the basin across the southern boundary. This subduction seems to
256 occur predominantly in the southern subtropical Indian Ocean as shown in Figure 1a (blue
257 shading). A small subduction site also exists in the AS. However, the exact location of this
258 northward thermocline flow is not yet known. Both poor sampling of deeper layers of the Indian
259 Ocean and relatively coarse resolution models used to study the dynamics of Indian Ocean have
260 contributed to poor understanding of the subsurface thermocline northward flow in the Indian
261 Ocean. The suite of global ocean circulation models including relatively fine resolution models
262 that participated in the CORE-II simulations (Danabasoglu et al., 2014) used in this paper made
263 it possible to document simulated pathways of the thermocline water into the NIO. The CEC
264 variability accounts for a significant portion of Indian Ocean cross-equatorial heat transport,
265 which is hypothesized to be associated with the Asian monsoon (Chirakova and Webster, 2006;
266 Swapna et al., 2017).

267
268 The Indian Ocean circulation is mainly driven by the seasonal reversal of the monsoon
269 wind. Thus, the mean and variability of wind forcing has a large impact on Indian Ocean
270 simulations (Parekh et al., 2011). More generally, the heat, water, and momentum balances are
271 affected by uncertainties in turbulent and radiative heat fluxes. These uncertainties in the forcing
272 fields can have a major role in the fidelity of OGCM simulations on intra-seasonal, seasonal,
273 inter-annual and longer time-scales (McWilliams, 1996). Hence, accurate near-surface
274 atmospheric fields are essential for realistic simulations in a forced ocean model. Here, we offer
275 a brief overview of how the CORE-II atmospheric state compares to observational based
276 measures. However, a full assessment of these impacts requires comparisons to simulations run

277 with other atmospheric products such as [Japanese 55-year atmospheric reanalysis \(JRA-55\)](#)
278 [based surface dataset for driving ocean–sea-ice models \(JRA55-do\)](#):Tsuji no et al., 2018) and
279 DRAKKAR (Brodeau et al., 2010) forcing. The analysis presented in this paper provides a
280 necessary starting point for that assessment.

281
282 Our study is motivated by the important role of the Indian Ocean in regional and global
283 climate variability, especially in the tropics. This role in turn prompts the need for improved
284 understanding of Indian Ocean circulation dynamics, including its mean state and variability, in
285 support of improved simulations of regional and global climate (e.g., Swapna et al., 2014). We
286 are motivated to perform systematic assessments of Indian Ocean features found in global
287 climate model simulations. Increased awareness of the role of the Indian Ocean for regional and
288 global climate, including its importance for the billions of humans living along its coasts and
289 nearby regions, prompts the need to systematically articulate the problems and prospects with
290 global model simulations for this region.

291
292 The paper is organized as follows. Section 2 describes the [CORE-II simulations and the](#)
293 [main goal of the study](#). Section 3 describes models and observational datasets. Section 4 contains
294 [main results and discussions organized as: \(i\) the evaluation of CORE-II wind speed with in-situ](#)
295 [observation \(Section 4.1\);\(ii\) the time mean features of SST and its seasonal cycle over the key](#)
296 [regions of the Indian Ocean, including the AS, BoB, Eastern Equatorial Indian Ocean \(EEIO\)](#)
297 [and Thermocline Ridge \(TR\) region \(Section 4.2\); \(iii\) surface salinity and BL \(Section 4.3\);](#)
298 [\(iv\)subsurface features of temperature and salinity over AS, south eastern AS \(SEAS\), BoB,](#)
299 [EEIO\(Section 4.4\); \(v\)surface and subsurface equatorial currents in CORE-II models and](#)
300 [observations \(Section 4.5\); \(vi\)Indian Ocean meridional overturning circulation \(Section](#)
301 [4.6\).](#)The impact of increased model resolutions is described in section 5. Major findings from our
302 analysis and its future implications are finally summarized in Section 6.

303
304
305

306 2. CORE-II simulations and the goals of this paper

307 The first phase of the Coordinated Ocean-ice Reference Experiments (CORE) project
308 (CORE-I) made use of a synthetically constructed normal year forcing (NYF; Large and Yeager,
309 2009) with seven modeling groups participated in the study of Griffies et al. (2009). An
310 underlying question pursued with CORE is whether models using the same atmospheric state
311 (atmospheric state is prescribed over a fixed annual cycle) will produce broadly similar
312 simulation features. However analyses showed many differences in the simulated results. For
313 example models are unable to simulate the realistic MOC; also models are unable to reach an
314 equilibrium state after a transient phase that in turn prompted further model development and
315 improvement (see more details in Griffies et al., 2009). The second phase (CORE-II) makes use
316 of the interannually varying atmospheric forcing (IAF) of Large and Yeager (2009) over the 60-
317 year period from 1948 to 2007. Details of the CORE-II protocol are given by Danabasoglu et al.
318 (2014). The CORE-II project is the largest coordinated effort to assess the scientific integrity of
319 global ocean/sea-ice simulations. It is now included as Phase-I of the Ocean Model Inter-
320 comparison Project (OMIP), a part of the World Climate Research Programme Coupled Model
321 Inter-comparison Project-phase 6 (CMIP6; Eyring et al., 2016), as documented by Griffies et al.
322 (2016).

323
324 CORE-II simulations are readily comparable to historical observations given their
325 historical forcing. Hence, CORE-II experiments facilitate the assessment of global ocean/sea-ice
326 simulations and **allow one** to mechanistically probe ocean processes active on sub-seasonal to
327 decadal time scales (e.g., Danabasoglu et al., 2014, 2016; Griffies et al., 2014). At present, there
328 **are nine** CORE-II assessment papers published in the journal Ocean Modelling that provide
329 **detailed analyses** over the Pacific, Atlantic, Southern and Arctic Oceans. We here focus on the
330 Indian Ocean. Since the ISMR prediction is dependent on the mean oceanic and atmospheric
331 conditions, the central question addressed in this paper is: how well do global ocean/sea-ice
332 models capture the mean state and seasonal cycle of the Indian Ocean? Most models employ one
333 to two degrees horizontal grid spacing, though there are two that use finer spacing (~0.25

334 degree), thus admitting mesoscale eddies in the low latitudes and correspondingly fine scale
335 currents.

336

337

338 **3. Model and observational data used in this study**

339

340 **3.1 Models**

341 We provide a summary of 16 global ocean/sea-ice model configurations in Table 1, with further
342 details provided in the CORE-II papers of Danabasoglu et al. (2014) and Farneti et al. (2015).

343 We focus on the 5th CORE-II forcing cycle and use model years corresponding to years of

344 available observations for 1982-2007. The surface fluxes of heat, freshwater/salt, and momentum

345 are determined using the CORE-II inter-annual forcing (IAF) atmospheric data sets, the model's

346 prognostic SST and surface currents, and the bulk formulae described in Large and Yeager

347 (2004) and Large and Yeager (2009). There is no restoring term applied to SST. SSS restoring is

348 used to prevent unbounded salinity trends in all the model simulations used for this study. The

349 NEMO-based models convert SSS restoring to a freshwater flux. All the other models apply SSS

350 restoring as a salt flux. The restoring time scales vary considerably by days to years between the

351 groups. Weak restoring with time scales of about 4 years were used in FSU, KIEL and NCAR,

352 moderate restoring with time scales of 9–12 months were used in AWI, BERGEN, CERFACS,

353 CMCC, CNRM, GFDL-MOM, ICTP and MRI, strong restoring with time scales of 50–150 days

354 were used in ACCESS and GFDL-GOLD (see Appendix C in Danabasoglu et al.,(2014) for

355 more details on SSS restoring technique). [The vertical mixing scheme used in different models](#)

356 [is detailed in Appendix A of Danabasoglu et al. \(2014\).](#)

357

358 For SST, we also make use of nine corresponding climate models (Table 2) from the

359 Coupled Model Inter-comparison Project Phase 5(CMIP5; Taylor et al., 2012), utilizing

360 historical runs forced with natural and anthropogenic radiative gases to simulate climate over

361 years 1850–2005. We use CMIP5 simulations from January 1982 to December 2005 for

362 generating a monthly climatology. There are many studies which show that ISMR variability is

363 mainly governed by the mean state SST in the Indian Ocean (Lee et al., 2010; Li et al., 2001).
364 Most of the coupled models show large cold biases in SST in the Indian Ocean, especially in the
365 AS. The cold bias will have large impacts on the coupled feedbacks and thus the monsoon. Sujith
366 et al. (2019) showed that improvements in mean state of SST in coupled model (CFSv2) has led
367 to realistic simulation of Oceanic modes of variability over IO, Pacific (i.e. ENSO, Indian Ocean
368 Dipole(IOD)) and that lead to improve simulation of ISMR. The very purpose of CORE-II
369 experiments is to see how the ocean models perform with a prescribed atmospheric state. In the
370 coupled models the exact cause of the SST bias is not yet known hence we used SST simulations
371 from both the forced and coupled model with same ocean configuration to delineate the probable
372 source of the SST bias. The comparison between CORE-II and CMIP5 SST patterns offers a
373 means to expose the role of atmosphere-ocean coupling with a dynamical atmospheric model on
374 SST patterns. A more complete comparison of CORE-II and CMIP5 simulations is beyond our
375 scope.

376

377

378

379

380

381

382

383

384

385 Table 1: List of models and their configurations used for the CORE-II inter-annual simulations
 386 following Danabasoglu et al (2014). Note that z^* represents the stretched geopotential vertical
 387 coordinate that absorbs motion of the free surface (see Adcroft and Campin, 2004 for details).

Group	Configuration	Ocean Model	Sea-ice Model	Vertical	Orientation	Horizontal	Resolution nominal
ACCESS	ACCESS-OM	MOMp1	CICE4	z^* (50)	tripolar	360 x 300	1°
AWI	FESOM-COREII	FESOM	FESIM	z (46)	displaced	126000	1°
BERGEN	NorESM	MICOM	CICE4	sigma2 (51+2)	tripolar	360 x 384	1°
CERFACS	ORCA1	NEMO3.2	LIM 2	z (42)	tripolar	360 x 290	1°
CMCC	ORCA1	NEMO3.3	CICE 4	z (46)	tripolar	360 x 290	1°
CNRM	ORCA1	NEMO3.2	Gelato 5	z (42)	tripolar	360 x 290	1°
FSU		HYCOM 2.2	CSIM 5	hybrid (32)	tripolar	320 x 384	1°
FSU-2		HYCOM 2.2	CICE4	hybrid (32)	tripolar	500x382	1°
GFDL-MOM	ESM2M-ocean-ice	MOM 4p1	SIS	z^* (50)	tripolar	360 x 200	1°
GFDL-MOM025	CM2.5-ocean-ice	MOM5	SIS	z^* (50)	tripolar	1440 x 1070	0.25°
GFDL-GOLD	ESM2G-ocean-ice	GOLD	SIS	sigma2 (59+4)	tripolar	360 x 210	1°
ICTP		MOM 4p1	SIS	z^* (30)	tripolar	180 x 96	2°
MRI-F		MRI.COM 3	MK89; CICE	z (50)	tripolar	360 x 364	1° x 0.5°
KIEL	ORCA05	NEMO 3.1.1	LIM 2	z (46)	tripolar	722 x 511	0.5°
KIEL025	ORCA025					1442 x 1021	0.25°
NCAR		POP 2	CICE4	z (60)	displaced	320 x 384	1°

388 Table 2: List of coupled climate models and their configurations used from CMIP5

389

	Atmosphere	Ocean	Modeling Centre	Ocean Resolution
ACCESS1-0	1.25 ⁰ x 1.875 ⁰ L38	ACCESS-OM (MOM4p1)	Commonwealth Scientific and Industrial Research Organization (CSIRO) and Bureau of Meteorology (BOM), Australia	nominal 1°
CCSM4	0.94 ⁰ x 1.25 ⁰ L26	POP2	National Center for Atmospheric Research, USA	nominal 1°
CMCC-CM	T159L31	OPA8.2	Centro Euro-Mediterraneo per I Cambiamenti Climatici, Italy	nominal 1°
CNRM-CM5	T127L31 (256 × 128)	NEMO	Centre National de Recherches Meteorologiques / Centre Europeen de Recherche et Formation Avancees en Calcul Scientifique, France	nominal 1°
GFDL-CM3	2 ⁰ x 2.5 ⁰ L48	MOM4p1	Geophysical Fluid Dynamics Laboratory, USA	nominal 1°
GFDL-ESM2M	2 ⁰ x 2.5 ⁰ L24			nominal 1°
GFDL-ESM2G	2 ⁰ x 2.5 ⁰ L24	GOLD		nominal 1°
MRI-CGCM3	T159L48	MRI.COM3	Meteorological Research Institute, Japan	nominal 1°
NorESM1-M	1.875 ⁰ x 2.5 ⁰ L26	NorESM-Ocean	Norwegian Climate Center, Norway	nominal 1°

390 3.2 Observations and reanalysis data used for the model evaluation

391 We make use of the following observational and reanalysis data to evaluate the CORE-II
392 simulations.

- 393 • Monthly one degree gridded optimum interpolation (OI) SST product (Reynolds
394 et al., 2002) for 1982-2007 is taken from the National Oceanic and Atmospheric
395 Administration (NOAA).
- 396 • The subsurface temperature and salinity are taken from the World Ocean Atlas
397 (WOA09) climatology (Locarnini et al., 2010; Antonov et al., 2010; Boyer et al.,
398 2009). We also use WOA09 for the SSS. In WOA09, data until 2006 were used
399 to compute the climatology. However, more Argo profiling data started in 2007 in
400 the Indian Ocean. Including those years of data in the climatology may represent
401 different mean state as compared to mean state based on data until 2006. Since the
402 CORE-II simulations ran until 2007, hence we used WOA09 for this study.
- 403 • Surface currents are taken from the Ocean Surface Current Analysis (OSCAR,
404 Bonjean and Lagerloef, 2002). The OSCAR product is available at 0.33° spatial
405 resolution and 5 day averaged. For this study, we computed monthly
406 climatologies from the 5-day averaged data for the period 1993-2007. We also use
407 ship drift climatology from Cutler and Swallow (1981) as well as the near-surface
408 current (0 - 15 m) climatology (version 2.07) from satellite-tracked drogued
409 drifter velocities gridded at 0.5x0.5° resolution (Lumpkin and Johnson, 2013). All
410 these data were re-gridded to 1°x1° conforms to the MOM grid for comparison.
- 411 • We employ monthly-mean 1°x1° zonal and meridional subsurface currents from
412 the Operational ocean reanalysis system (ORAS4) (Balmaseda et al., 2013)
413 reanalysis product for 1982-2007. The long-term mean is calculated for this
414 period. Inter-comparison studies of different reanalysis products over Indian
415 Ocean show ORAS4 is performing best among most of the widely used products
416 (Karmakar et al., 2017).
- 417 • Observed long-term monthly mean net heat flux (NHF) was used from National
418 Oceanography Centre Southampton (NOCS; Berry and Kent, 2009) available at

419 1°x1° resolution. We also used monthly-mean TropFlux (Praveen Kumar et al.,
420 2013) NHF for 1982-2007 and computed monthly climatologies for the
421 comparison.

422
423 We note that different observation based products differ among each other and this can
424 adversely affect the assessment of model performance based on single observation. Thereby, by
425 comparing the model simulations with multiple observational products we may achieve robust
426 results.

427

428 **3.3 Data sets used for the wind speed evaluation**

429

430 We used buoy wind speed observational data at 3 m height provided by National Institute
431 of Ocean Technology (NIOT) under National Data Buoy Programme (NDBP) of the Ministry of
432 Earth Sciences, Government of India (Premkumar et al., 2000), to compare the most widely used
433 forcing fields from CORE-II, JRA55-do (Tsujino et al., 2018) and DRAKKAR (Brodeau et al.,
434 2010). The buoy location is at 94 °E, 10.5 °N in the BoB and shown in Figure 1a as red pin.
435 Daily wind speed from buoy is used for the comparison. The 3-hourly 55-km horizontal
436 resolution JRA55-do, and the 6-hourly 75-km resolution DRAKKAR wind speed were used for
437 the comparison. However, daily averages were computed from these 3-hourly and 6-hourly data
438 to compare with daily buoy wind speed. These datasets have been corrected relative to reanalysis
439 product ERA-Interim (Dee et al., 2011) for DRAKKAR and Japanese 55-year Reanalysis
440 (Kobayashi et al., 2015) for JRA55-do products, analogous to how CORE-II has been corrected.
441 We also used Cross-Calibrated Multi-Platform (CCMP; available at
442 <http://rda.ucar.edu/datasets/ds745.1/#!access>) Surface Wind Vector Analyses (Atlas et al., 2009)
443 for the spatial wind speed comparison. Here we provide a comparison of CORE-II with
444 DRAKKAR and JRA55-do to understand the reliability of these products for the Indian Ocean
445 simulation. There are notable differences in spatial resolution (CORE-II: 2° and JRA55-do: 0.5°)
446 as well as differences in temporal resolutions (CORE-II: 6-hourly and JRA55-do: 3-hourly). Yet
447 for the comparison we only considered daily averaged data sets from all products. The corrected

448 CORE-II, JRA55-do and DRAKKAR data are available at 10 m height. For comparison, we
449 interpolate the CORE-II, JRA55-do and DRAKKAR 10 m winds to 3 m using the logarithmic
450 scale given by Stull (2011).

451 **3.4. Assessment in sub-regions of the Indian Ocean**

452 The Indian Ocean variability is very inhomogeneous (e.g. Schott et al., 2009). Hence, we
453 find it useful to examine the simulations within sub-regions as shown in Figure 1a. These regions
454 include the Arabian Sea (AS): 50 - 70 °E and 6 - 25 °N, the Bay of Bengal (BoB): 79.5 – 95.5 °E
455 and 7.5 – 23.5 °N, the South Eastern Arabian Sea (SEAS): 71 - 77 °E and 7 - 13 °N, the Eastern
456 Equatorial Indian Ocean (EEIO): 80 - 100 °E and 5 °S - 5 °N, the Thermocline Ridge (TR): 50 -
457 75 °E and 5 °S - 10 °S and the Southern Indian ocean (SIO): 40 - 100 °E and 15 °S - 30 °S.

458 **4. Results and discussions**

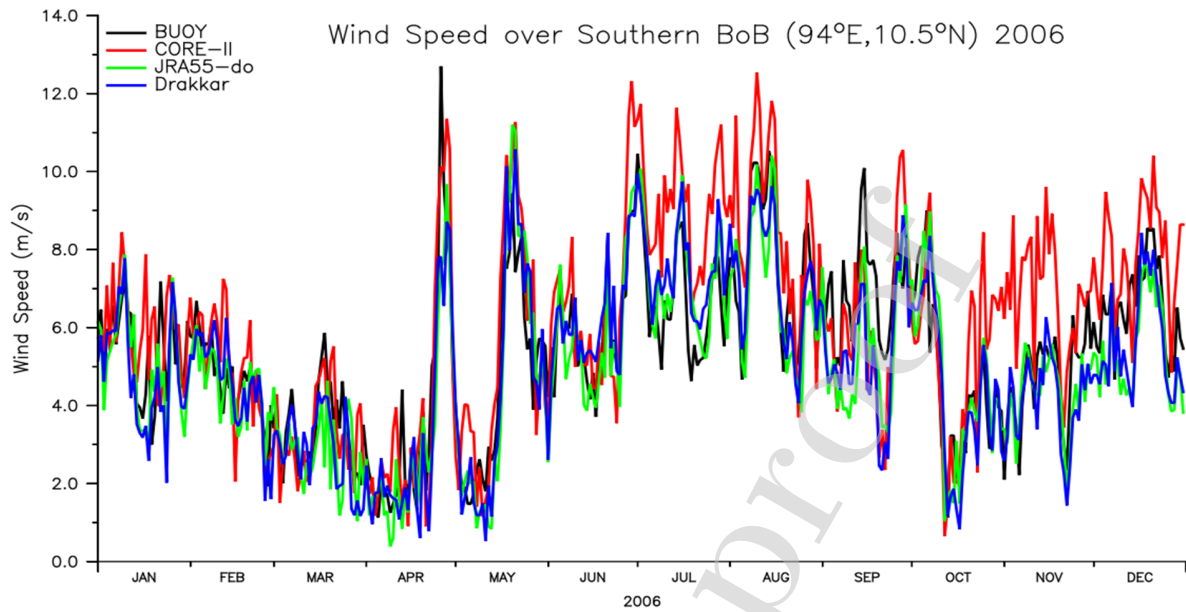
459

460 **4.1. Evaluation of CORE-II forcing fields**

461 **4.1.1 Assessment of the winds and latent heat fluxes**

462 Latent Heat Flux (LHF) is mainly determined by wind speed apart from near-surface air
463 temperature and humidity. Thus, any error in the computation of LHF due to inconsistencies in
464 any of these components would reflect in the [NHF](#). Rahaman and Ravichandran (2013) have
465 documented the evaluation of CORE-II near surface humidity and air temperature. The findings
466 of Rahaman and Ravichandran (2013) [are](#) briefly mentioned in section 4.1.2. In what follows, we
467 therefore restrict our comparison to the wind speed.

468 Figure 2 shows the time series comparison of daily wind speed from corrected CORE-II,
469 JRA55-do and DRAKKAR in 2006 over south BoB. CORE-II winds reproduce the observed
470 seasonal and intra-seasonal variability. However, for most of the year, it overestimates the buoy
471 wind speed (Figure 2). In contrast, JRA55-do and DRAKKAR winds more



472

473

474 Figure 2: Daily wind speed comparison of CORE-II, JRA55-do and DRAKKAR with buoy data
 475 over the south Bay of Bengal at 3 m height for 2006.

476

477 accurately capture the buoy-observed daily wind speed, with at times, slight under estimations.

478 The statistics of wind speed comparison is given in Table 3. The CORE-II mean wind speed bias

479 is 0.8 m/s with a root-mean-square deviation (RMSD) value of 1.75 m/s and a correlation

480 coefficient of 0.8. The underestimation of JRA55-do and DRAKKAR wind speed with respect to

481 buoy observation is reflected with mean bias of -0.40 m/s and -0.35 m/s respectively (Table 3).

482 However, the RMSD values in JRA55-do and DRAKKAR are much lower when compared to

483 CORE-II. CORE-II winds have larger variability as compared to buoy observation with standard

484 deviations of 2.1 m/s in the buoy and 2.6 m/s in CORE-II. JRA55-do and DRAKKAR standard

485 deviation (SD) values are very close to the observed buoy value (Table 3).

486

487

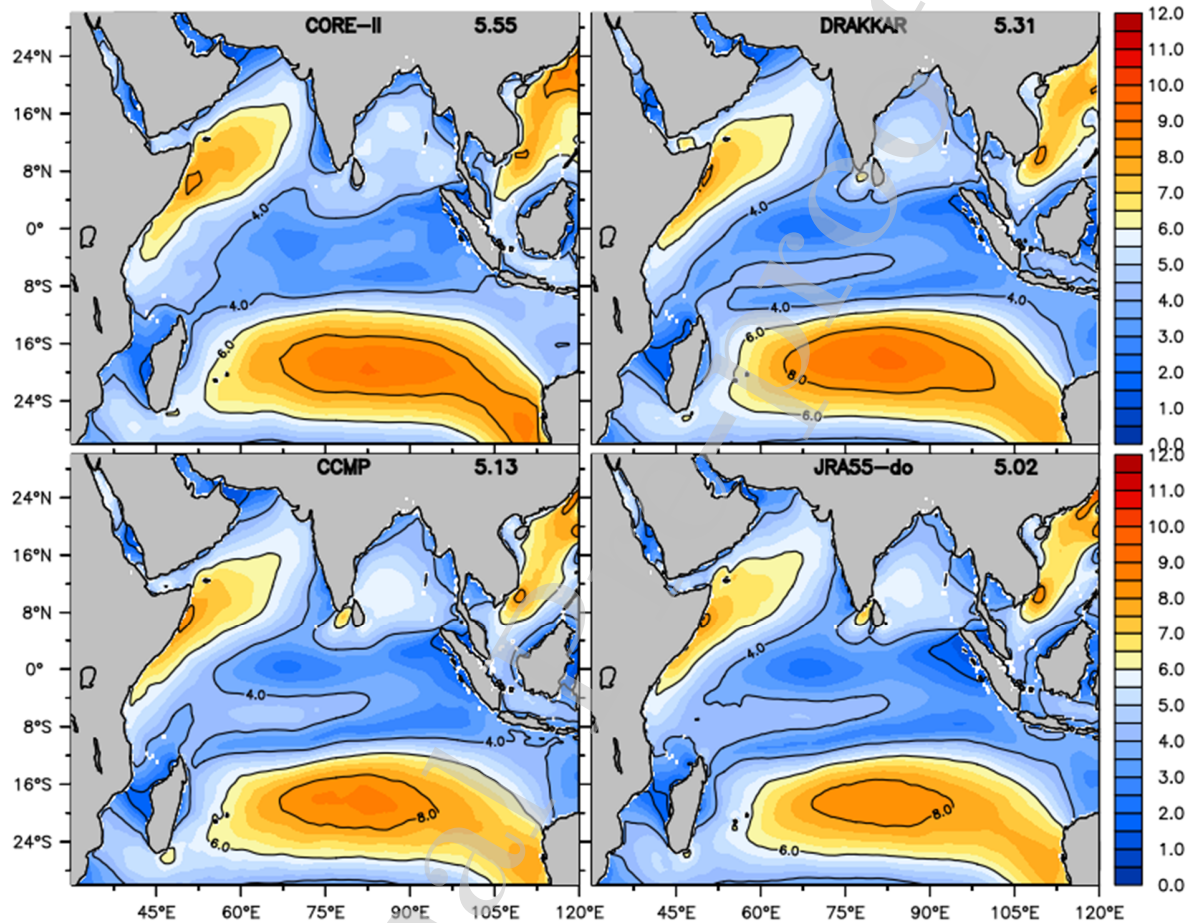
488 Table3: Wind Speed Comparison statistics over Bay of Bengal (Buoy location 94°E, 10.5°N).

	AN3 2006 (no of points 365)				
	Mean (m/s)	Standard Deviation (SD) (m/s)	Bias (m/s)	Correlation Coefficient (CC)	RMSD (m/s)
Buoy	5.38	2.09	-	-	-
CORE-II	6.16	2.64	0.78	0.80	1.75
JRA55-do	4.98	2.17	-0.4	0.84	1.26
DRAKKAR	5.03	2.20	-0.35	0.86	1.20

489

490 Figure 3a shows the 1993-2007 mean spatial distribution of wind speed from CORE-II, CCMP,
491 JRA55-do and DRAKKAR. The basin-average mean wind speed is given within each panel (top
492 right). The values are roughly similar except for CORE-II, which is slightly higher than the other
493 products, which is also seen in the buoy comparison (Figure 2). The mean wind speed structure
494 over the Indian Ocean is **dominated** by the summer monsoon wind. The summer monsoon wind
495 speed over AS is high as compared to BoB and it reflects in the annual mean structure. CORE-II
496 wind speed is higher by ~ 0.5 m/s over the west coast of Australia as compared to the other
497 products. This region also shows the highest wind speed over the entire Indian Ocean. CORE-II
498 wind is corrected by QuikScat wind (Large and Yeager, 2009), but still it shows higher values as
499 compared to buoy and other wind products. Yu et al. (2007) have reported large LHF over this
500 region in NCEP2 product as compared to other products, and attributed this bias to the strong
501 wind. Sanchez-Franks et al. (2018) also noted LHF biases in this region and linked them to dry
502 biases in humidity. The spatial distribution of monthly SD is shown in figure 3b. All wind
503 products show that the variability is highest over the Somalia coast and it is $\sim 4-5$ m/s in CORE-

504 II, DRAKKAR and JRA55-do, but slightly lower values ($\sim 3-4$ m/s) are seen in satellite-based
 505 product, CCMP. The variability is lowest over equatorial Indian Ocean and in a zonal band over
 506 the south Indian Ocean ($20 - 25^\circ\text{S}$) in all products. The SD values over these regions are similar
 507 in DRAKKAR, CCMP and JRA-do, but slightly larger values are seen in CORE-II.

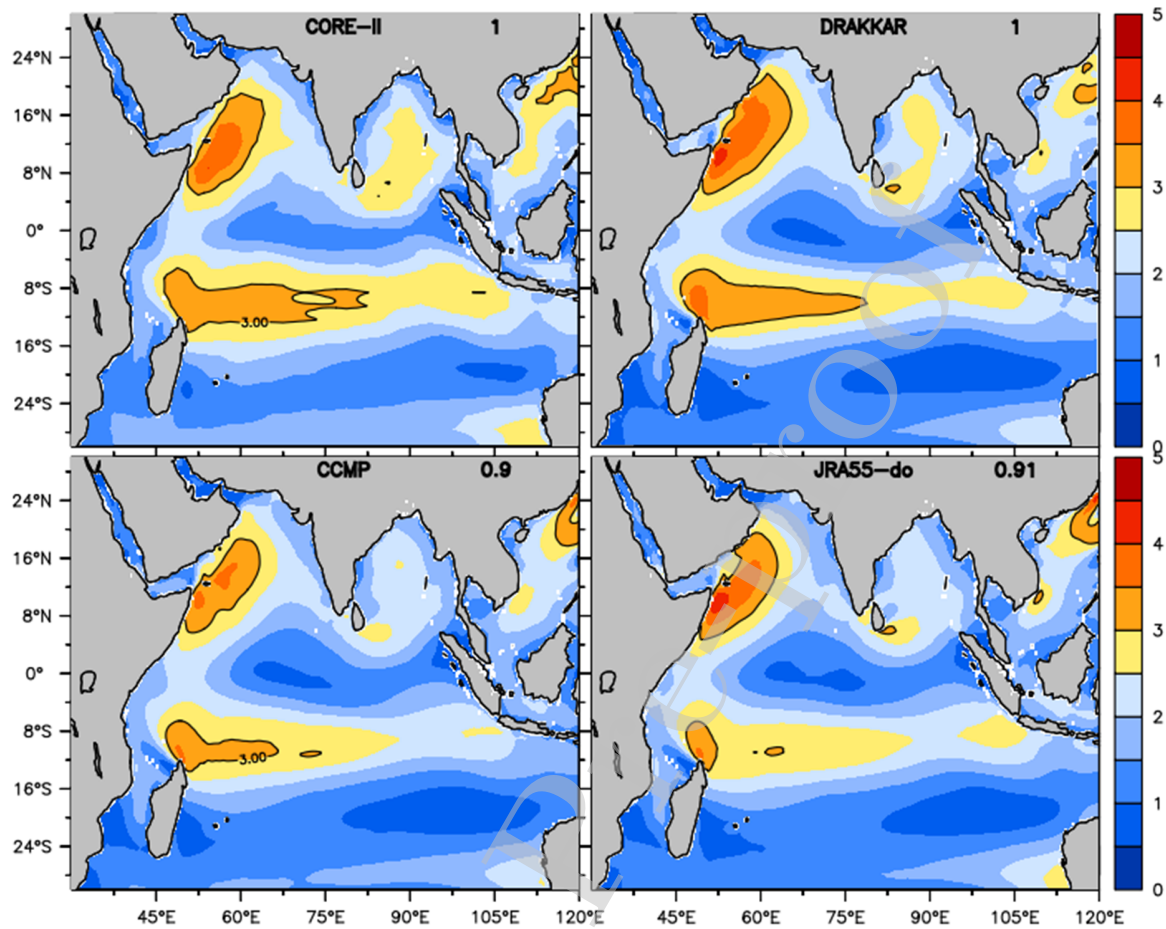


508

509 Figure 3a: Mean wind speed (m/s) at 10 m height from CORE-II, DRAKKAR, CCMP and
 510 JRA55-do. Average over 1993-2007 is taken. The basin-average mean values are given in the
 511 upper right corner of each panel.

512

513

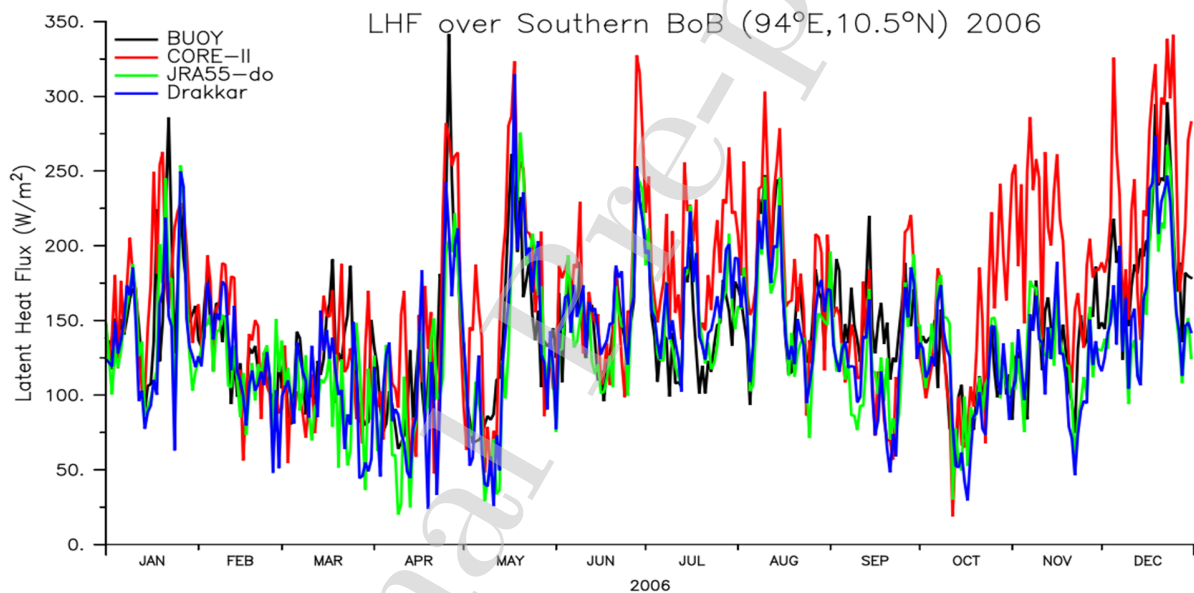


514

515 Figure 3b: Monthly standard deviation (1993-2007) of wind speed (m/s) at 10 m height from
 516 CORE-II, DRAKKAR, CCMP and JRA55-do. The basin averaged mean values are given in the
 517 upper right corner of each panel.

518 To understand the wind impact on LHF, we computed latent heat fluxes using bulk
 519 formula (see details in Rahaman and Ravichandran, 2013) by using buoy observed atmospheric
 520 fields but replacing buoy wind speed with CORE-II, JRA55-do and DRAKKAR wind speed
 521 fields. The daily LHF comparison is shown in Figure 4. The wind impact on LHF shows RMSD
 522 values of $\sim 50 \text{ W/m}^2$ and a mean bias of $\sim 22 \text{ W/m}^2$ in CORE-II. The underestimation of wind

523 speed in JRA55-do and DRAKKAR is reflected as mean LHF bias of -11 W/m^2 and -10 W/m^2
 524 respectively. Sanchez-Franks et al. (2018) found that JRA-55 underestimates buoy wind speed in
 525 the BoB in agreement with results here. Biases in turbulent heat fluxes of the order reported in
 526 their work can have large implications for a product/model to correctly represent monsoon-
 527 related processes. The RMSD values of 36 W/m^2 and 34 W/m^2 are much lower in JRA55-do and
 528 DRAKKAR as compared to CORE-II. These results also corroborate the finding of Swain et al.
 529 (2009). They showed that over the SEAS during monsoon season, 1 m/s RMSD in wind speed
 530 can cause 45 W/m^2 RMSD in LHF. As expected the variability in CORE-II is also large with SD
 531 value 62 W/m^2 as compared to buoy SD value of 44 W/m^2 . The SD in JRA55-do and
 532 DRAKKAR is also very close to the SD derived from buoy observations (Table 4).



533
 534 Figure 4: Latent Heat Flux (LHF) computed from buoy observations (black) and replaced buoy
 535 wind speed with CORE-II (red curve), JRA55-do (green curve) and DRAKKAR (blue curve)
 536 wind speed fields. In the calculation of LHF only wind fields are changed, while all other fields
 537 are from observations. This comparison reveals the impact of wind speed on LHF.

538

539 Table 4: LHF Comparison statistics over Bay of Bengal (Buoy location 94 °E, 10.5°N).

	AN3 2006 (no of points 365)				
	Mean (W/m ²)	Standard Deviation (SD) (W/m ²)	Bias (W/m ²)	Correlation Coefficient(CC)	RMSD (W/m ²)
Buoy	144	44	-	-	-
CORE-II	166	62	22	0.70	50
JRA55-do	133	46	-11	0.72	36
DRAKKAR	134	47	-10	0.75	34

551 4.1.2 Specific humidity, air temperature, and radiative fluxes

552 Rahaman and Ravichandran (2013) evaluated CORE-II specific humidity (Qa) and air
553 temperature (Ta) with independent *in situ* observations over the tropical Indian Ocean. They
554 reported that the RMSD value of Ta is ~0.5 °C, but a large drop in Ta observed during intense
555 rainfall events are not well captured by CORE-II products. They also reported a change in 1
556 g/kg Qa can cause about 11–15 W/m² errors in latent heat flux. Qiu et al. (2004) showed that
557 over the western North Pacific, the synoptic-scale heat fluxes have a large impact on SST and
558 have typical amplitude of ±1°C. The downwelling fluxes of shortwave and longwave radiation
559 from the CORE-II product have been evaluated with the tropical moored buoy observations
560 (Venugopal and Rahaman, 2019). They found the mean bias in CORE-II over the Atlantic Ocean
561 is about zero and a root-mean-square deviation (RMSD) of 43 W/m² and 12 W/m² for
562 downwelling shortwave and longwave radiation, respectively. For the Indian Ocean with respect
563 to Research Moored Array for African-Asian-Australian Monsoon Analysis & Prediction
564 (RAMA) buoy the mean bias is roughly -3 W/m² and -8 W/m² but with large RMSD values of 50

565 W/m^2 and $14 W/m^2$ for downwelling short and longwave radiation, respectively. The variability
566 is also underestimated with standard deviations of $70 W/m^2$ in RAMA for shortwave whereas in
567 CORE-II it is $48 W/m^2$. In the case of longwave, variability is larger in CORE-II ($23 W/m^2$) as
568 compared to buoy values of $18 W/m^2$. CORE-II forcing fields compare reasonably well to
569 observational-based measures as well as other reanalysis products.

570

571 **4.2. Sea Surface Temperature**

572 In this section, we offer a particularly extensive analysis of the SST given its importance
573 for Indian Ocean climate variability and due to its relatively precise observational measures. For
574 the analysis purpose, we regrided all models and observed SST and NHF data set uniformly on a
575 $1^\circ \times 1^\circ$ grid.

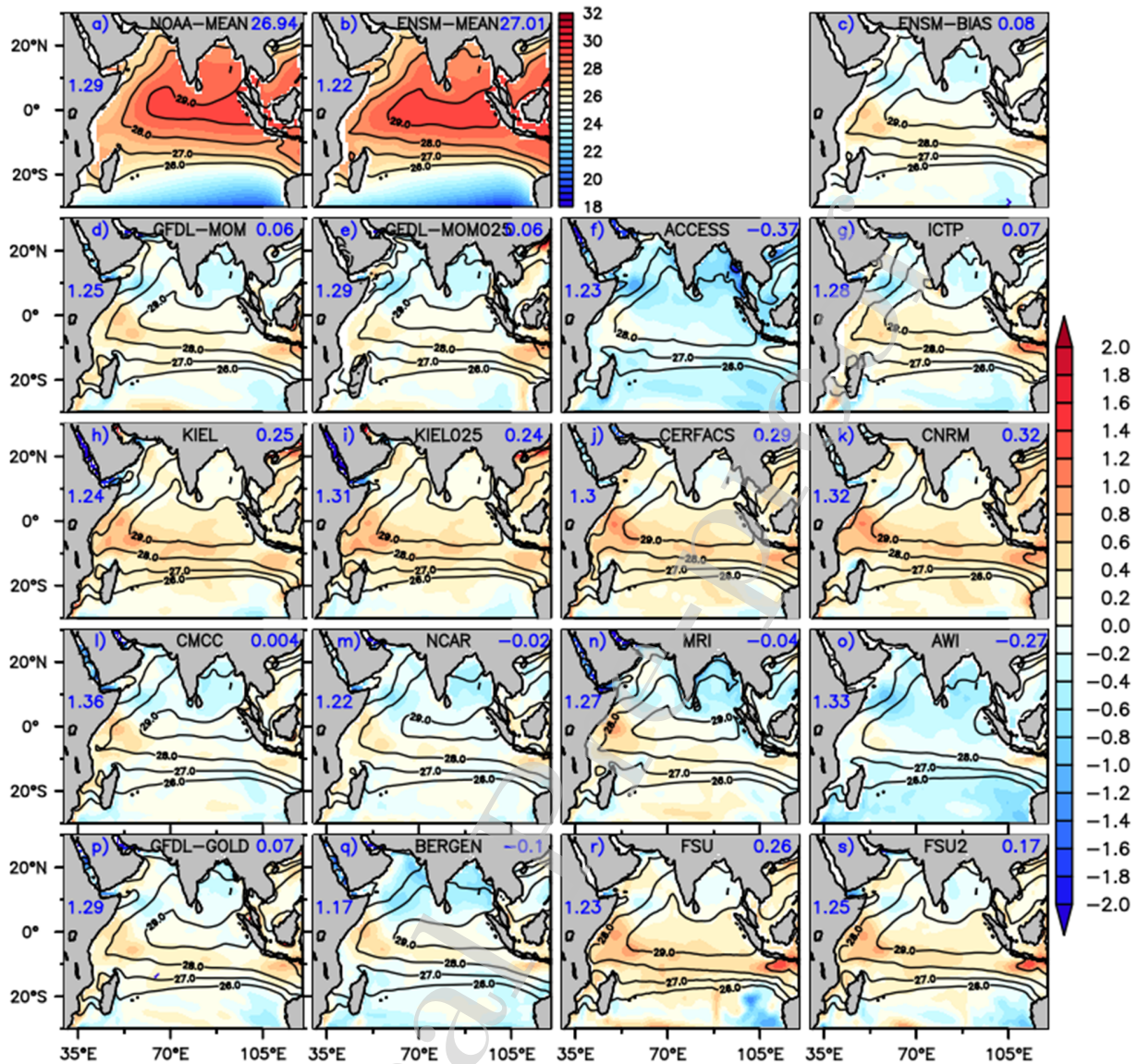
576

577 **4.2.1 Spatial patterns**

578 **4.2.1.1 SST patterns from CORE-II simulations**

579 Figure 5 shows the annual mean SST bias for each model together with the model
580 ensemble mean bias. The observed and model ensemble mean SST is also shown in the upper
581 left corner panels. The annual mean is computed over the period 1982 to 2007 for both
582 observations and models. The OI-SST data is based on advance very high resolution radiometer
583 (AVHRR) satellite data (Reynolds et al. 2002) which is available from April 1981, hence we
584 used 1982 - 2007 to compute monthly climatology. Observations (Fig 5a) show SST cooler in
585 the west and warmer in the east (Murtugudde and Busalacchi, 1999; Schott et al., 2009) and a
586 tongue of relatively warm SST ($>29^\circ C$) in the

587



588

589 Figure 5: Annual mean SST bias (model minus observation) from all model simulations are
 590 shown in color (panels d-s). The contours show the annual mean SST (1982-2007) of the
 591 5thCORE-II cycle. The model ensemble mean bias is shown in the upper right panel (c).
 592 Observed annual mean SST from observation is shown in upper left panel from NOAA-OI
 593 (Reynolds et al 2002) (a). The ensemble mean from CORE-II models is shown in the upper
 594 middle panel (b). Contour levels for the NOAA-OI observation and all models are the same.

595 Units are in degrees Celsius. The basin averaged mean (upper right corner) and its standard
596 deviations (left) are also given in each panel in blue colors.

597
598 equatorial Indian Ocean, forming the Indian Ocean warm pool (Fasullo and Webster, 1999; Rao
599 et al., 2015; Rao and Ramakrishna, 2017). The CORE-II ensemble mean (Fig 5b) reproduces this
600 warm pool structure both in terms of the magnitude and spatial extent. Looking at singular model
601 annual means (Fig. 5d-s, contours) almost all of them reproduce the observed patterns. Two
602 exceptions are AWI and ACCESS, where the maximum SST does not exceed 28 °C, and show a
603 basin-wide cold bias (shaded values) including the warm pool region. Zonal variation of the SST
604 pattern is well reproduced in all the CORE-II simulations. The ensemble mean SST pattern
605 nearly replicates the observed mean SST spatial pattern. Individual models show biases of +/- 1
606 °C with a warm bias over the southwest Indian Ocean and cold bias over the AS and BoB. No
607 significant improvement is seen in the two eddy-permitting models GFDL-MOM025 and
608 KIEL025 as compared to their coarser resolution companion configurations. Therefore, biases
609 may be arising more from improper representation of physical parameterizations (e.g., boundary
610 layer processes) than coarse grid resolution or it may be also due to surface forcing bias.

611 Previous studies have shown that the NHF accounts for most of the tropical Indian Ocean
612 (TIO) SST variability (Murtugudde and Busalacchi, 1999; Klein et al., 1999). Over the AS, apart
613 from the NHF, oceanic processes also play a major role in the SST variability (Shenoi et al.
614 2002). However, SST over BoB is more air-sea flux driven due to the Bay's BL (Vialard et al.,
615 2012). In the tropical southwest Indian Ocean (SWIO), ocean dynamics plays an important role
616 at all timescales due to local and remotely-forced ocean dynamics (Lau and Nath, 2004).
617 Murtugudde and Busalacchi (1999) and Xie et al. (2002, 2009) have shown that SST variability
618 over this region is forced by thermocline variability and mixed layer-thermocline interactions.
619 The warm SST bias over this region is coincident with the warmer thermocline temperature bias
620 over the same region (see Figure 19). The NHF bias computed from model SSTs is uniform
621 throughout the basin (~10 W/m²) in all these models (not shown), which further confirms this
622 finding. The NEMO-based models (CERFACS, CNRM, CMCC and KIEL) show slightly larger
623 warm bias to the south of the equator as compared to other models.



624

625 Figure 6: Mean SST bias (model minus observation) in March from all model simulations are
 626 shown in shade (panels d-s) from the 5th CORE-II cycle. The overlaid contour levels are for the
 627 mean SST in March. The ensemble mean from CORE-II models is shown in the upper middle
 628 panel (b). Ensemble mean bias for all models is shown in upper right panel (c). Observed
 629 mean SST in March from observations is shown in the upper left panel (NOAA-OI) (a). Contour levels
 630 for NOAA-OI observation and all models are same. The basin averaged mean (upper right

631 corner) and its standard deviations (left) are also given in each panel in blue colors. Units are
632 degrees Celsius.

633
634 In the AS and the BoB, almost all simulations show a cold SST bias. The annual mean
635 cold bias over these regions mainly arises from a large cold bias during March (Figure 6).
636 Chowdary et al. (2015, 2016) have shown that the seasonal SST over the BoB is governed by the
637 seasonal NHF. But the observational study of Thangaprakash et al. (2015) show that vertical
638 processes and horizontal advection also play a significant role in the seasonal SST tendency over
639 the BoB. The NHF in CORE-II simulated models does not differ much with the TropFlux
640 observations (see Figure 11b and Section 4.2.2.2). Hence, the different magnitudes for the SST
641 bias in CORE-II simulated models over the BoB could be due to the vertical processes and
642 horizontal advection, thus supporting the finding of Thangaprakash et al. (2015).

643
644 In the AS, the Great Whirl and the southern eddy are two dominant anti-cyclonic eddies
645 present near the Somalia coast. The Great Whirl has been observed to form during late May and
646 early June between 5 °N and 10 °N. A large branch of the East African Coastal Current (EACC)
647 turns offshore after crossing the equator at about 2 °N to 3 °N and forms the Southern Gyre (SG).
648 The SG is a large anticyclonic retroflection cell with a well-marked wedge of cold upwelled
649 water attached to its northern flank (the southern cold wedge). A third anticyclonic eddy named
650 the Socotra Eddy (SE) is frequently present in the northeast of the Island of Socotra (Beal and
651 Donohue, 2013; Beal et al., 2013). The very prominent small circular patch of cold SST bias
652 seen over these regions, found in most of the CORE-II models, represents the presence of these
653 anti-cyclonic eddies in July and October (Figure not shown). Most of the models show a cold
654 bias with ACCESS showing the largest (~ 1.5 °C). GFDL-MOM group of models also shows a
655 fairly large cold bias, whereas this bias is relatively small in the NEMO group of models. Annual
656 mean bias over the BoB in the NEMO models and FSU are least among all the model
657 simulations.

658

659 The region of the equatorial Indian Ocean and latitudes to its south shows a positive bias
660 (~ 0.6 °C) in all simulations except AWI and ACCESS, whose simulations show a small cold
661 bias (~ 0.4 °C). All biases are within observational errors (Bhat et al., 2004; Senan et al., 2001.)
662 Furthermore, the flux errors are larger than the corrective fluxes needed to correct these SST
663 biases which make it difficult to assign any errors in the models (see Murtugudde et al., 1996).
664 However, the high mean SSTs are close to atmospheric convective thresholds and thus even
665 small errors can lead to large errors in a coupled climate model. The CORE-II models
666 realistically simulate the spatial distribution and zonal variation of SST in the Indian Ocean. The
667 basin-wide bias is within ± 1 °C seen in almost all the models, which may arise from
668 problems representing ocean physics as well as atmospheric forcing. We conjecture that the most
669 important physical process is related to vertical mixing, given the importance of upper ocean
670 boundary layer processes for setting the SST. These results suggest that a focus on improved
671 physical parameterizations may, in the near term, offer more advances in Indian Ocean
672 simulations than refinement of the grid resolution. This conclusion is supported by Benshila et al.
673 (2014).

674

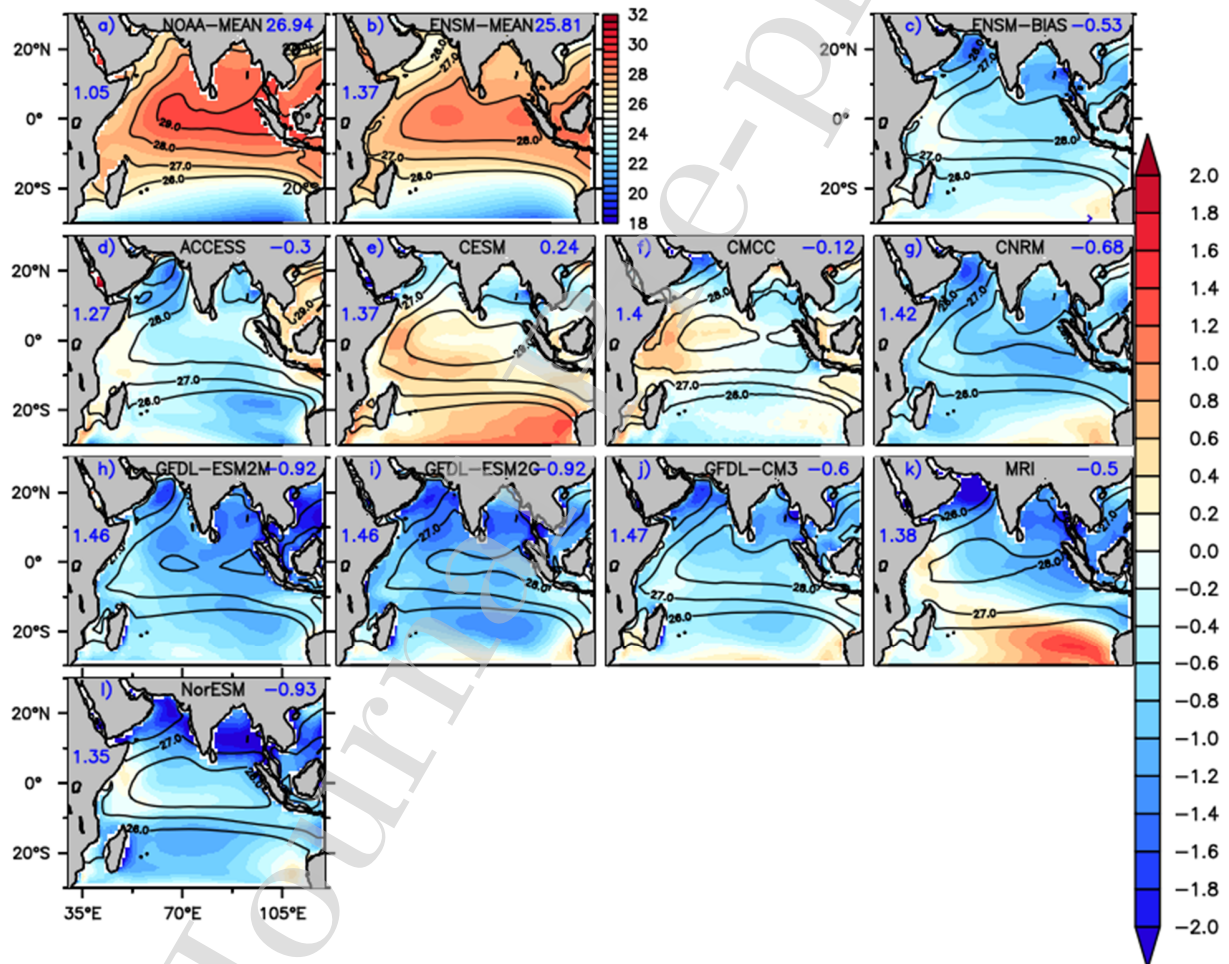
675 **4.2.1.2 Comparing SST from CORE-II and CMIP5 simulations**

676 We here compare SST from CMIP5 coupled models using the same ocean component as
677 the CORE-II models. In particular, we analyze SSTs from CMIP5 historical simulations from the
678 nine models that employ the same ocean configuration used in our CORE-II study (Table
679 2). Compared to forced CORE-II model simulations, coupled CMIP5 simulations show SST
680 biases that are not uniformly distributed across different seasons. They also show a similar
681 pattern to that of the forced simulations described in Section 4.2.1.1, but with larger amplitude.
682 The larger biases suggest the amplification of SST errors that arise from coupling with an
683 interactive atmospheric model.

684

685 Previous studies have identified a cold SST bias in the Indian Ocean in coupled climate
686 models (Pokhrel et al., 2012a,b; Chowdary et al., 2015, 2016; Prasana, 2015). Fathrio et al.
687 (2017a) examined the western Indian Ocean SST biases among CMIP5 models and found that

688 about half of the models show positive SST biases, while others show negative bias. The models
 689 with cold SST biases exhibit a colder bias in the entire tropical Indian Ocean throughout the
 690 year. The positive bias was attributed to relatively weak southwest monsoonal winds over the AS
 691 and an equatorial southeasterly wind bias. The warm SST biases persisted until boreal fall, and
 692 then disappeared in winter (Li et al., 2015). All CMIP5 models show cold SST biases over the
 693 northern AS during the pre-monsoon season (Marathayil et al., 2013; Sandeep and
 694 Ajayamohan, 2014; Levine et al., 2013; Li et al., 2015; Fathrio et al., 2017a). Studies show that
 695 anomalous advection of cold surface air from the south Asian landmass during boreal winter
 696 contributes to the cold SST biases over the north AS (Marathayil et al., 2013; Sandeep and
 697 Ajayamohan, 2014).



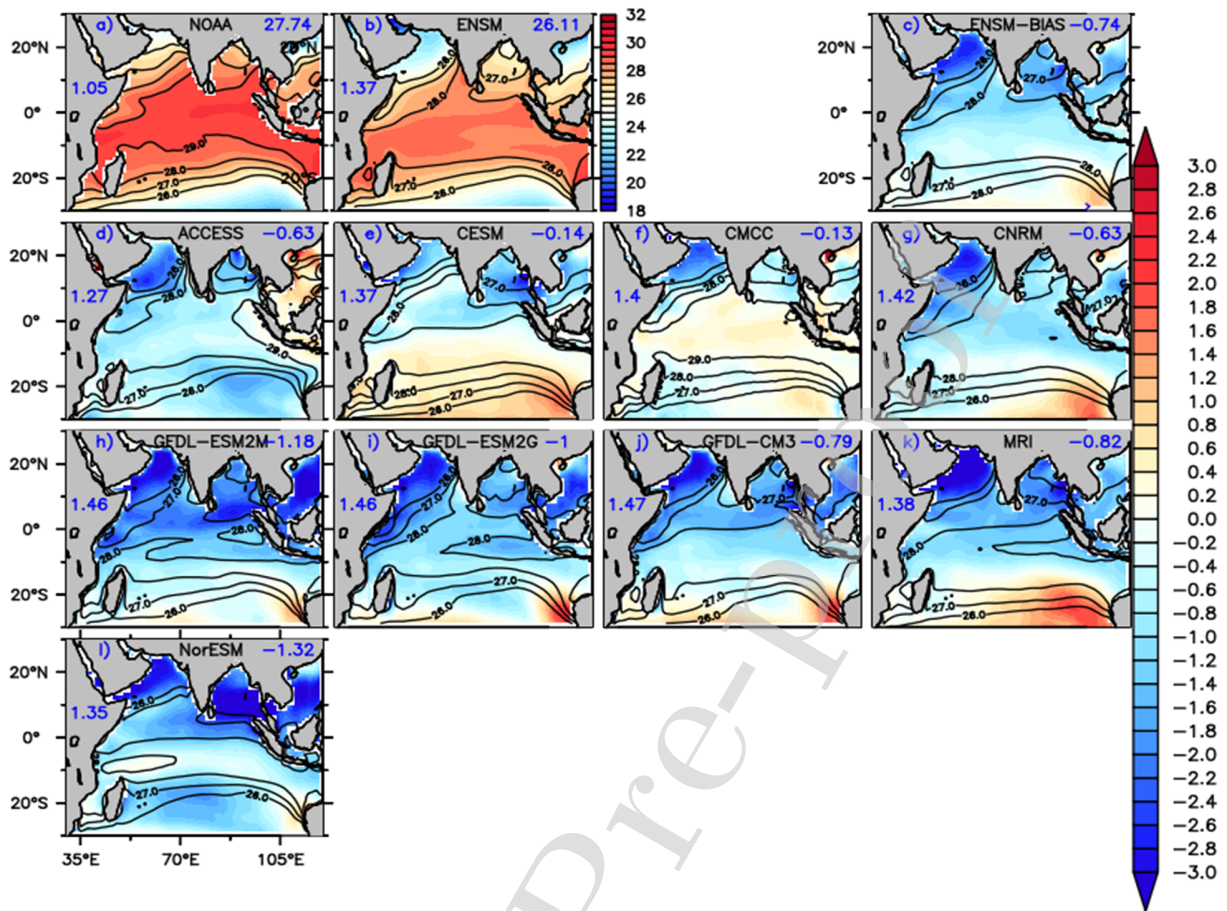
698

699 Figure 7: Annual mean SST bias (model minus observation) from CMIP5 simulations (shade),
700 with contours for the mean SST. The ensemble mean from the CMIP5 models is shown in the
701 upper middle panel (b). The CMIP5 model ensemble mean bias is shown in the upper right
702 panel (c). Observed annual mean SST is shown in upper left panel from NOAA-OI (a). Contour
703 levels for the NOAA-OI observation and all models are the same. The basin averaged mean
704 (upper right corner) and its standard deviations (left) are also given in each panel in blue colors.
705 Units are degrees Celsius.

706 We show the annual mean SST (contour) and bias (colour) from the CMIP5 simulations
707 in Figure 7. Except for CESM and CMCC (which corresponds to the NCAR CORE-II ocean/ice
708 configuration), none of the CMIP5 models reproduce the observed warm pool over the equatorial
709 Indian Ocean (Rao et al., 2015). The majority of the CMIP5 models show a basin-wide cold bias
710 with highest bias in the north AS up to 4 °C. The north AS cold bias is more than 3°C in MRI
711 whereas CESM shows the smaller cold bias of ~0.6 °C. CESM, CMCC and MRI show a warm
712 positive bias (of up to 1.6 °C) over the western equatorial Indian Ocean and southeast Indian
713 Ocean off the Australian Coast. The overall basin wide cold bias is weakest in CMCC (-0.12 °C)
714 and largest in NorESM(-0.93 °C). The largest basin averaged cold bias in CORE-II ocean only
715 simulations is -0.37 °C in ACCESS. Biases in the NCAR CORE-II model are only ~ 0.1-0.2 °C
716 to the south of the equator. However, when coupled as part of CESM, this model shows roughly
717 five to ten times larger biases up to ~1 °C.

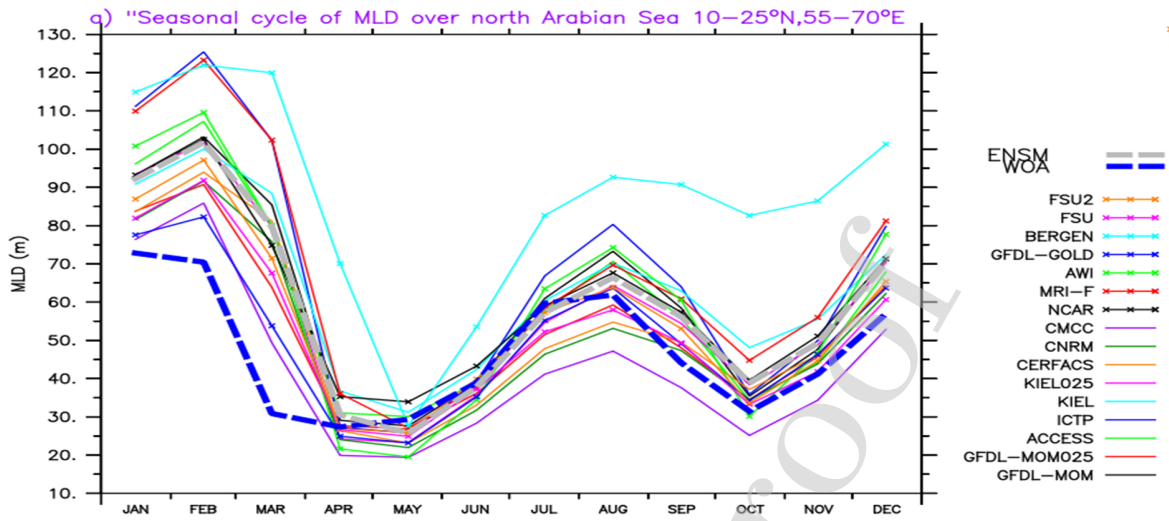
718
719 The large cold bias in the CMIP5 models over the northern AS in the annual mean mostly arises
720 from the cold bias during Feb-April, which peaks in March (Figure 8). The SST cold bias is
721 larger than 3 °C in GFDL-ESM2M, GFDL-ESM2G, GFDL-CM3, NorESM and MRI during
722 March. Sandeep and Ajayamohan (2014) show a similar cold bias, but with larger amplitude
723 over the north AS in all CMIP5 models. They attributed this bias to an equatorward bias in the
724 subtropical jet stream during boreal spring, thus causing excessive cooling of the northern AS
725 and adjoining land regions. This cold bias in coupled models was also attributed to the
726 northeasterly cold air temperature (Marathayil et al., 2013).

727 The cold bias in forced CORE-II simulations is much weaker when compared to coupled
728 models that use the same ocean component (Figure 5 and Figure 7). The cold biases in the
729 CORE-II simulations are ~ 1 °C over the northern AS whereas they are ~ 3 °C in the CMIP5
730 models, with even larger biases in the MRI and NorESM. These results suggest that the large
731 northern AS SST biases in coupled models may arise from coupled dynamical feedbacks that
732 amplify ocean errors. This hypothesis is supported by Figure 9a, which shows the seasonal cycle
733 of the mixed layer depth (MLD) in CORE-II models and WOA observations over the north
734 AS. The CORE-II MLDs are generally deeper than WOA during Feb-March. Figure 9b shows the
735 MLD vs SST bias over the northern AS. It can be seen that larger SST cold biases are associated
736 with deeper MLDs as compared to observations. The correlation coefficient between MLDs and
737 SST bias is 0.64, which is significant at the 99 % confidence level. In figure 9b the BERGEN
738 simulation appears like an outlier. Without this simulation the correlation coefficient value
739 reduces from 0.64 to 0.50 but it is still significant at the 95 % confidence level. Tozuka et al.,
740 (2017) showed in the upstream Kuroshio Extension region in the North West Pacific that the
741 deeper MLD is less sensitive to cooling by surface heat fluxes. However, Roxy et al. (2012)
742 showed a shallow (deep) MLD enhances (suppress) the SST anomaly, thereby amplifying
743 (lessening) the intra-seasonal variability of the monsoon in a coupled model (CFSv2) and argued
744 that a prime focus should be on improving the mixed layer scheme of the ocean component in
745 that model. This confirms the need of improvement of MLD in ocean models for a better
746 simulation of SST over the northern AS.



747

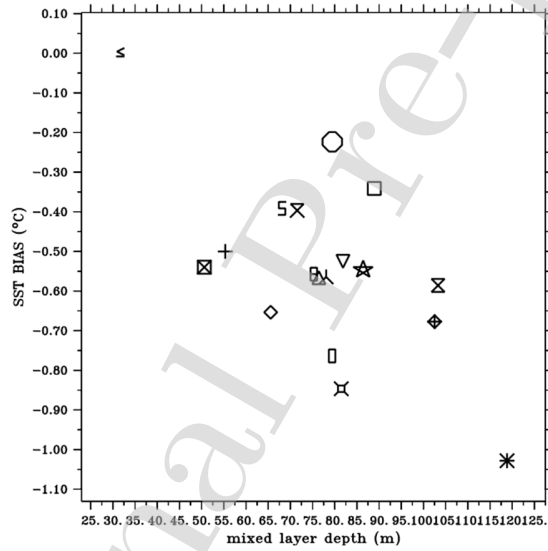
748 Figure 8: March mean SST bias (model minus observation) from CMIP5 simulations are shown
 749 in shade. The ensemble mean from the CMIP5 models is shown in the upper middle panel (b).
 750 Ensemble mean bias for all models is shown in the upper right panel(c). Observed mean March
 751 SST is shown in the upper right panel (NOAA-OI) (a). The basin averaged mean (upper right
 752 corner) and its standard deviations (left) are also given in each panel in blue colors.



753

754

(b)



755

756 Figure 9: (a) Seasonal cycle of MLD from all CORE-II model simulations and WOA
 757 observations averaged over northern AS (10-25 °N, 55-70°E) (b) scatter plot of MLD vs SST
 758 bias over northern AS for the individual models in March. For the observations (NOAA-OI) the
 759 SST bias is just zero while the MLD (32 m) is the reference for that month. The correlation
 760 coefficient between model MLD and SST bias is 0.639, which is significant at 99 % confidence
 761 level.

762 These results suggest that the origin of SST bias during [spring](#) (Feb-March-April) mainly
763 arise from the coupled feedbacks as well as MLD biases. The spatial distribution and magnitude
764 of SST bias in CORE-II forced simulations are weaker than those in coupled simulations since
765 the errors are amplified by coupled feedbacks. We conjecture that the basin-wide cold bias in
766 CORE-II simulations arises from deficiencies in ocean vertical mixing, with biases enhanced due
767 to coupled feedbacks in the coupled model simulations.

768

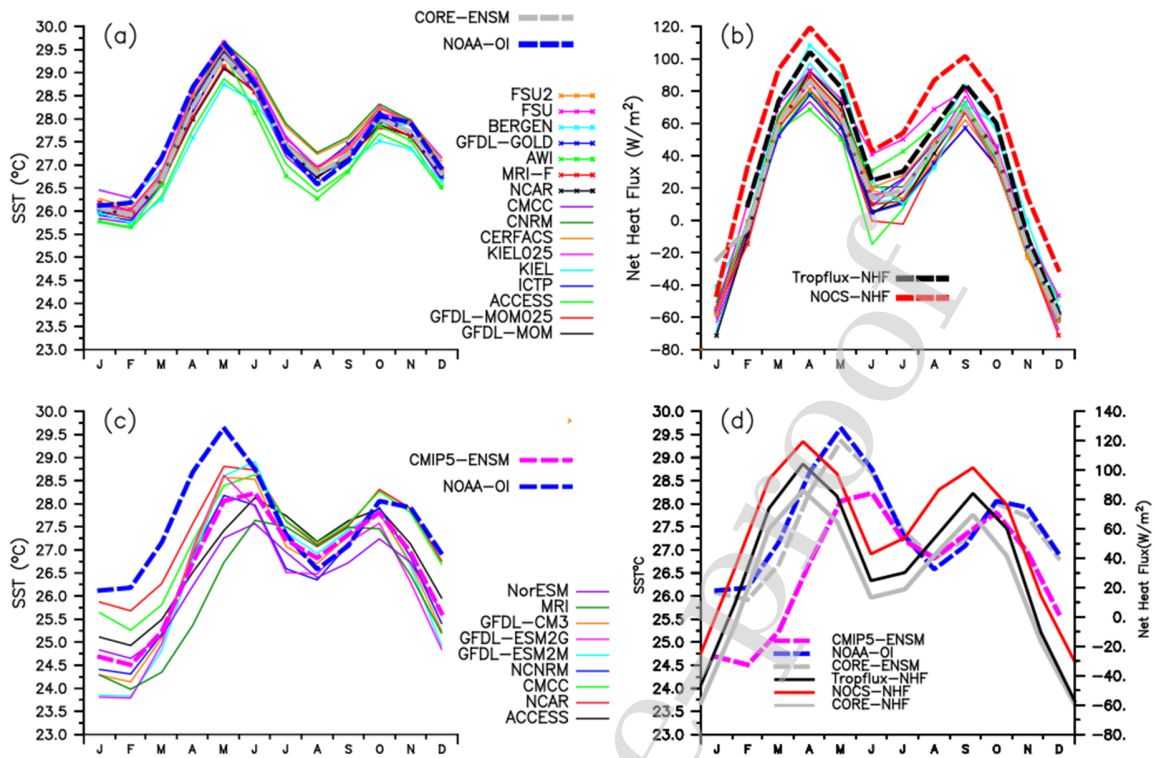
769 **4.2.2 Seasonal cycle of SST and net surface heat flux**

770 The Indian Ocean circulation and tracer property distributions exhibit great spatial
771 inhomogeneity. Correspondingly, so is the spatial distribution of the SST bias. Hence, we here
772 consider the area averaged seasonal cycle over the different sub-regions shown in Figure 1 and
773 described in [Section 3.4](#). The ability of model simulations to correctly capture the seasonal SST
774 variation is a difficult task, particularly over the north Indian Ocean.

775

776 **4.2.2.1 Arabian Sea (AS)**

777 Figure 10a shows the seasonal evaluation of SST over the AS from CORE-II simulations and its
778 ensemble mean along with observations. The observed annual cycle over the AS shows a
779 bimodal SST seasonality with the primary maximum during April-May and the secondary
780 maximum in October (Murtugudde and Busalacchi, 1999; Vinayachandran and Shetye, 1991;
781 Fathrio et al., 2017a). During April–May, prior to the onset of the Indian summer monsoon, the
782 AS evolves to one of the warmest areas in the tropical oceans (Joseph, 1990; Joseph et al., 2006).
783 All CORE-II simulations show bi-modal SST seasonality, but there exists inter-model spread
784 that is largest during summer.



785

786 Figure 10: Seasonal cycle of SST over the Arabian Sea (AS) from (a) CORE-II simulations (c)
 787 CMIP5 simulations. The model ensemble mean and observed SST are also shown as dashed
 788 thick gray and blue lines, respectively. (b) Seasonal cycle of net heat flux from all the CORE-II
 789 simulations as well as two observations (NOCS and TropFlux in dashed thick red and black
 790 lines, respectively). (d) Seasonal cycle of CORE-II and CMIP5 ensemble mean and NOAA-OI
 791 SST (left axis) and net heat flux (NHF) from CORE-II simulations and observations (NOCS and
 792 TropFlux; right axis). The legend for individual models is the same in panels a and b.

793

794 Observations show that SST reduces after the onset of the summer monsoon in June. It reaches a
 795 minimum during the peak summer monsoon (Jul-Aug) over the AS due to upwelling off the
 796 Somali Coast and Arabian Peninsula as well as due to latent heat loss caused by strong
 797 southwesterly monsoon winds (Shenoi et al., 2002). Another mechanism through which SST
 798 reduces over the AS is the export of heat through meridional overturning. Few models show
 799 lower SST during July-August with respect to NOAA-OI observation, while others show slightly

800 higher. This behavior could be due to the different cross-equatorial heat transport among
801 different models (Swapna et al., 2017).

802 The CMIP5 coupled model simulations show similar variations to those forced by
803 CORE-II, but CMIP results show far more inter-model spread (Figure 10c). The cold biases
804 during winter and spring in the coupled models are larger (~ 2 °C) than the CORE-II models
805 (~ 0.5 °C) (Figure 10a,c). Coupled Model Inter-comparison Project Phase 3 (CMIP3) and other
806 CMIP5 coupled models (not considered here) also show similar cold biases over the AS
807 (Marathayil et al., 2013; Levine et al., 2013). Levine and Turner (2012) showed that coupled
808 model SST biases over the northern AS are substantially larger than the observed interannual
809 variability of AS SST, and in turn these biases affect the Indian summer monsoon simulations
810 and forecasts (Narapusetty et al., 2015).

811

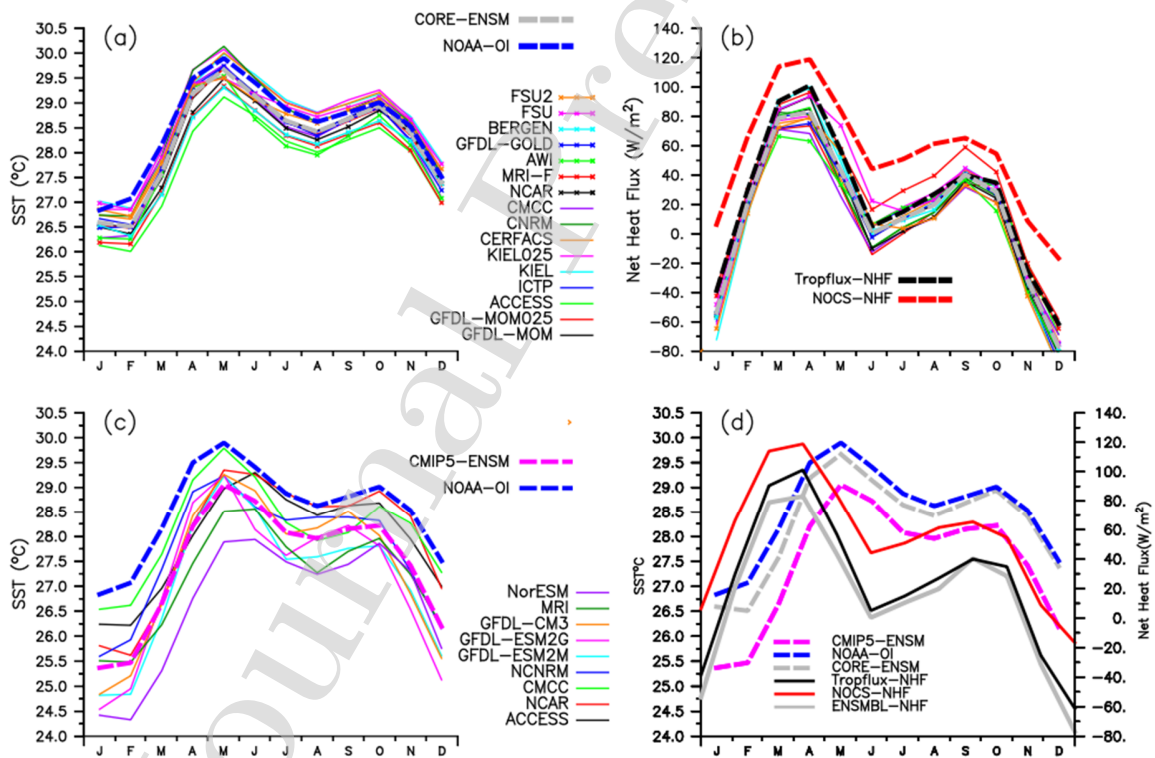
812 The AS seasonal cycle of **NHF** from the CORE-II models matches that of the TropFlux
813 observations (Figure 10b) during October-March, while the magnitude is about 20-30% less than
814 the observations. Despite this reasonably good match in surface heat flux forcing, the cold SST
815 bias in CORE-II simulations indicates the role of oceanic process in seasonal SST evolution,
816 which is also evident from the deeper MLD in all models (Figure 9a). Recent studies by
817 Parampil et al. (2016) have shown that TropFlux derived NHF over the NIO is more realistic
818 when compared with OAFLUX and satellite derived products. All the CORE-II models
819 underestimate the **NHF** as compared to observations (Figure 10b) during March-October. Most
820 models show a cold SST bias during spring but the majority shows warm bias during summer
821 (Jul-Aug) (Figure 10a). The wind speed is strong over AS in CORE-II during spring but it is
822 weaker during peak summer (Aug) as compared to other wind speed products (figure not
823 shown). This leads to an over estimation of the LHF in model. The overestimation of the LHF
824 due to CORE-II wind speed is also shown in Figure 4 and table 4. As previously noted, wind
825 speed is not the sole factor determining the LHF (Rahaman and Ravichandran, 2013). They
826 showed that the LHF overestimation is mainly due to the positive biases of CORE-II near-
827 surface air temperature and specific humidity.

828

829 Figure 10d shows the seasonal evolution of ensemble mean SST and NHF from
 830 observations, CORE-II and CMIP5 simulations. The NHF reaches its maximum in April whereas
 831 SST attains its maximum in May. Studies have shown that the seasonal evolution of SST
 832 tendency matches well with the NHF seasonal cycle (Chowdary et al., 2015; Sayantani et al.,
 833 2016; Kurian and Vinaychandran, 2007).

834

835 In summary, the bimodal semiannual cycle of SST in the AS is well captured by the
 836 CORE-II forced simulations, revealing weaker biases than the coupled CMIP5 models. We
 837 conjecture that the cold SST bias and under-estimation of SST maximum in the pre-summer
 838 monsoon season reflects a problem with simulated oceanic processes since the CORE-II
 839 ensemble NHF is reasonably well matched with both observational products. Additionally, the
 840 inability to reach the minimum SST during the summer monsoon season may arise from biases
 841 in the wind forcing (see section 2.4) as well as simulated oceanic processes.



842

843 Figure 11: Same as Figure 10 but for the Bay of Bengal (BoB).

844

845 **4.2.2.2 Bay of Bengal (BoB)**

846 Figure 11a shows the SST seasonal cycle over the BoB from CORE-II simulated models
847 and observations. As for the AS, the semiannual cycle is very prominent in the BoB, with peak
848 SSTs in May and October. Although the SST reduces rapidly over the AS following the
849 monsoon onset, SST in the BoB remains higher than 28°C, making the BoB favorable for deep
850 atmospheric convection (Gadgil et al., 1984; Graham and Barnett, 1987). The magnitude of SST
851 reduction in the BoB is smaller (~1 °C) than in the AS (2-3 °C). This difference arises from the
852 BL present in the BoB, with this layer suppressing ocean vertical mixing and thus maintaining a
853 higher SST throughout the year (Thadathil et al., 2008; Shenoi et al., 2002; deBoyer et al., 2007;
854 Sprintall and Tomczak, 1992). The models are able to simulate the observed seasonal cycle but
855 most underestimate the observed SST, with KIEL and KIEL025 as exceptions. This
856 underestimation of SST could be due to the models' inability to simulate properly the (observed)
857 BL thickness (Thadathil et al., 2008). Several studies point to the impact of the BoB's BL on
858 SST variation (e.g. deBoyer et al., 2007; Saji and Yamagata, 2003; Saji et al., 2006; Girishkumar
859 et al., 2011). The model study of Rahaman et al. (2014) suggested the importance of relatively
860 fine vertical grid spacing (~2 m) to properly represent the BL features. Note that most of the
861 CORE-II models have vertical grid spacing no finer than ~5 m in the upper ocean.

862 Further evidence for the oceanic role in establishing the SST biases can be further seen in
863 Figure 11b, which shows that the CORE-II ensemble mean surface heat fluxes closely follows
864 the TropFlux observations with little spread across the models. As pointed out by Parampil et al.,
865 (2016), data from NOCS overestimates the NHF compared to other observational products. This
866 bias is also reflected in Figure 11b where the NOCS NHF is larger than TropFlux throughout the
867 year.

868 In contrast to the CORE-II forced simulations, the coupled CMIP5 simulations show
869 larger SST bias ranging up to -2 °C almost throughout the year with maximum during February-
870 May (Figure 11c). The inter-model spread is large in coupled models compared to the CORE-II
871 forced simulations. Figure 11d shows the seasonal variation of the ensemble mean SST and the
872 NHF from both CORE-II and CMIP5 along with observations, with CORE-II models better

873 representing the seasonal variation of SST in the BoB than CMIP5 models, showing a rather
874 uniform offset of 1 °C over the year compared to observations.

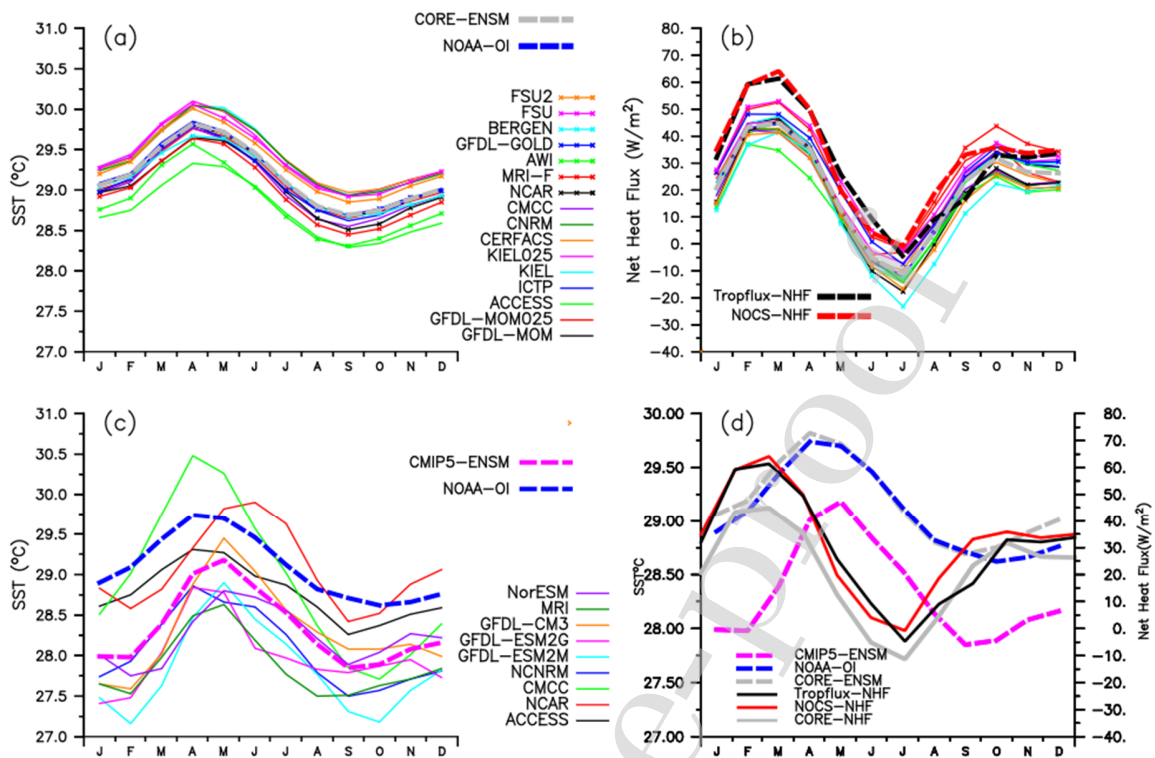
875

876 **4.2.2.3 Eastern Equatorial Indian Ocean (EEIO)**

877 SST over the Indian Ocean generally shows large-scale seasonal variability, but SST variation in
878 the EEIO remains within about ± 0.5 °C (Figure 12a). The mean SST is above 28 °C throughout
879 the year, thus favoring deep atmospheric convection (Gadgil et al., 1984) and rainfall throughout
880 the year. Figure 12a shows the EEIO SST seasonal cycle from CORE-II forced models and
881 observations. The observations show that SST exceeds 29 °C throughout the year and peaks in
882 April. All models are able to capture the observed seasonal cycle with comparatively small
883 biases (~ 0.25 °C), except ACCESS and AWI, both of which show a systematic year-round cold
884 bias of ~ 0.5 °C. Similar to the AS and the BoB, the NHF over the EEIO is also underestimated
885 by all models compared to both observational products. The CORE-II ensemble mean value
886 shows good agreement with the observations, but a large inter-model spread exists throughout
887 the year, with all models showing systematically warm or cold biases. KIEL and FSU show
888 positive SST biases during April-May despite a NHF that underestimates the observed values.
889 This result suggests that the NHF may not be a major factor determining the evolution of SST
890 during April-May, but that instead the ocean dynamics likely dominate. Over the EEIO,
891 particularly off Java and further east, horizontal advection through the ITF and vertical
892 entrainment by upwelling are the most important processes balancing the annual mean heat
893 budget, and these processes in turn control the SST variation (Qu et al., 1994; Du et al., 2005). In
894 the EEIO, the horizontal advection by the WJ is also expected to contribute to the SST (e.g.
895 Halkides and Lee 2009).

896

897



898

899 Figure 12: Same as Figure 10 but for the Eastern Equatorial Indian Ocean (EEIO).

900

901 Coupled CMIP simulations show large cold biases throughout the year and inter-model
 902 spread is much larger than their CORE-II counter parts (Figure 12c). The systematic inter-model
 903 spread is $\sim 2^\circ\text{C}$ and the systematic bias is much larger ($\sim 1\text{-}1.5^\circ\text{C}$) in coupled simulations
 904 compared to $0.25\text{-}0.5^\circ\text{C}$ in CORE-II simulations.

905 The zonal wind stress over this region is westerly from March to October and largest
 906 during northern hemisphere spring and autumn, driving the bi-annually observed equatorial jets
 907 in spring and autumn (Wyrtki, 1973). These equatorial jets deepen the thermocline in the east,
 908 thus contributing to SST increase in the EEIO.

909 Figure 12d shows the ensemble mean SST seasonal cycle from the CORE-II and the
 910 CMIP5 simulations along with observations. The ensemble mean NHF from the CORE-II
 911 simulations and observations (TropFlux and NOCS) are additionally overlaid. The CORE-II
 912 ensemble mean closely matches the observed SST seasonal cycle, whereas the CMIP5

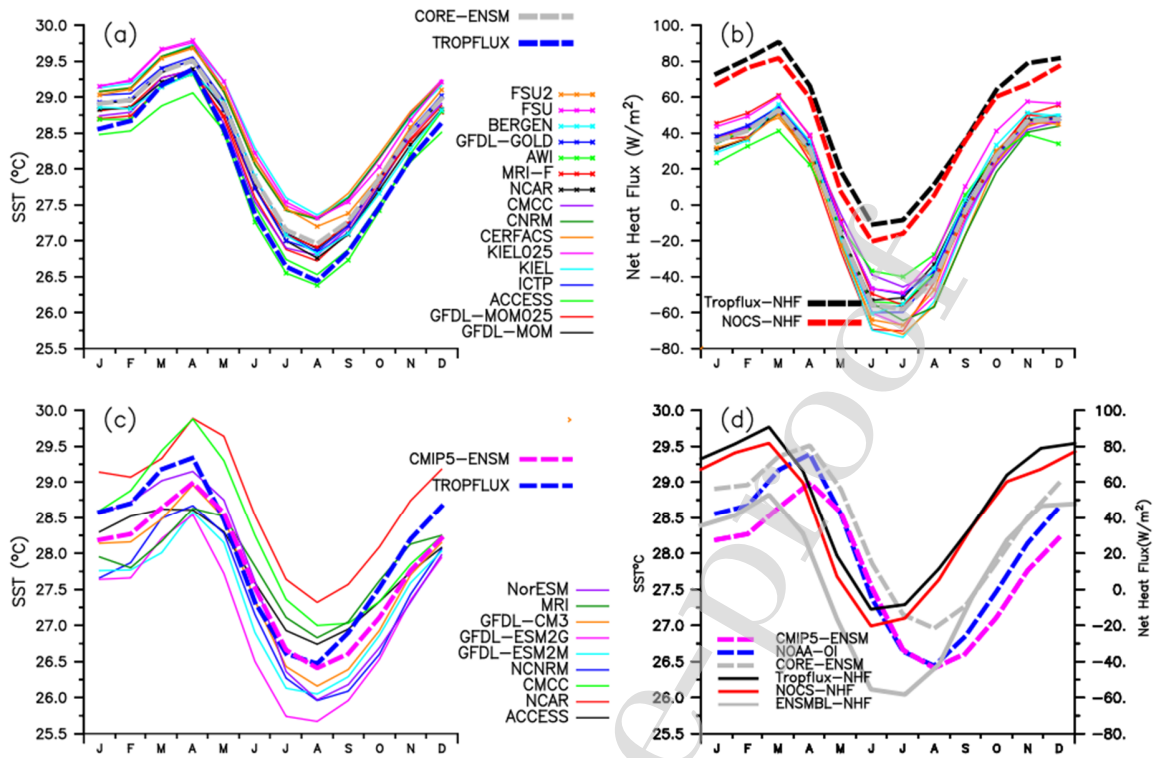
913 simulations show a systematic cold bias throughout the year with a maximum bias of about 1.2
914 °C during December-January. Additionally, the peak SST in CMIP5 models is reached in May,
915 which is one month after the observed peak in April. The NHF from the CORE-II ensemble is
916 underestimated throughout the year except in autumn. As for the AS and the BoB, the EEIO
917 NHF peaks one month earlier than the SST, so that the tropical Indian Ocean SST responds to
918 NHF changes after roughly one month.

919

920 **4.2.2.4 Thermocline Ridge**

921 SST in the TR (also called the Seychelles Dome) region shows a dominant annual cycle,
922 rather than a semiannual cycle as in the AS, the BoB and the EEIO (Levitus, 1987; Rao and
923 Sivakumar, 1999; Vialard et al., 2009). SST in the TR region has a large impact on the Indian
924 summer monsoon (Annamalai et al., 2005) and the tropical cyclone activity (Xie et al., 2002).
925 Therefore, it is important for coupled prediction models to simulate the observed SST variability
926 over TR. In particular, resolving its seasonal cycle provides a useful benchmark test for model
927 performance. Figure 13a shows the seasonal variation of SST from observations and

928



929

930 Figure 13: Same as Figure 10 but for the Thermocline Ridge (TR) region.

931

932 the CORE-II simulations. Observational estimates show an increase in SST from August to April
 933 followed by decrease from May to July as the cross-equatorial wind starts evolving (Figure 13a).
 934 Most of the models capture this seasonal variation, but they generally overestimate the observed
 935 SST throughout the year with a maximum during July-August (up to 1 °C). AWI and ACCESS
 936 capture the observed July-August cooling over the TR region. However, both models have a
 937 consistently cold bias over other sub-regions. The NHF is underestimated (Figure 13b)
 938 systematically by all CORE-II simulations with an ensemble bias (-60 W/m^2) during July-August
 939 (figure 13b). Horizontal advection tends to warm the SST in austral winter owing to the
 940 southward Ekman heat transport associated with the Indian summer monsoon (Yokoi et al.,
 941 2012). Despite a large negative NHF in the CORE-II simulations, many models show a warm
 942 bias during August, thus suggesting the role of excess heat transport from north of the Equator
 943 by the wind driven Ekman transport. Yokoi et al. (2012) also showed that cooling by vertical

944 turbulent diffusion in the ocean becomes most effective in the austral summer, owing to the
945 shallow mixed layer and correspondingly shallow thermocline during that season. Positive SST
946 biases may have arisen due to the reduced vertical cooling since the thermocline is deeper (85-
947 140 m) than found in the observations (75-80 m) (not shown). Similarly, the CMIP5 simulations
948 also capture the observed seasonal cycle of SST, but exhibit a larger inter-model spread than the
949 CORE-II simulations. Analysis indicates that almost half of the CMIP5 models shows a warm
950 bias and the rest show a cold bias, thus leading to an ensemble mean CMIP5 SST that is close to
951 the observation. Nagura et al. (2013) analyzed 35 coupled general circulation models (CGCM)
952 including some CMIP5 models for the simulations of the longitudinal biases in the Seychelles
953 Dome. They showed that the CMIP5 models are unable to simulate the longitude of the
954 upwelling dome and the magnitudes of the annual and semiannual cycles of thermocline depth
955 variability in the dome region. These biases could help to explain why some of the CMIP5
956 models generally have problems reproducing the observed seasonal cycle of SST over this
957 region. GFDL-ESM2G shows a systematic cold bias throughout the year (figure 13c). This
958 region also shows that the NHF leads SST by about one month (Figure 13d).

959

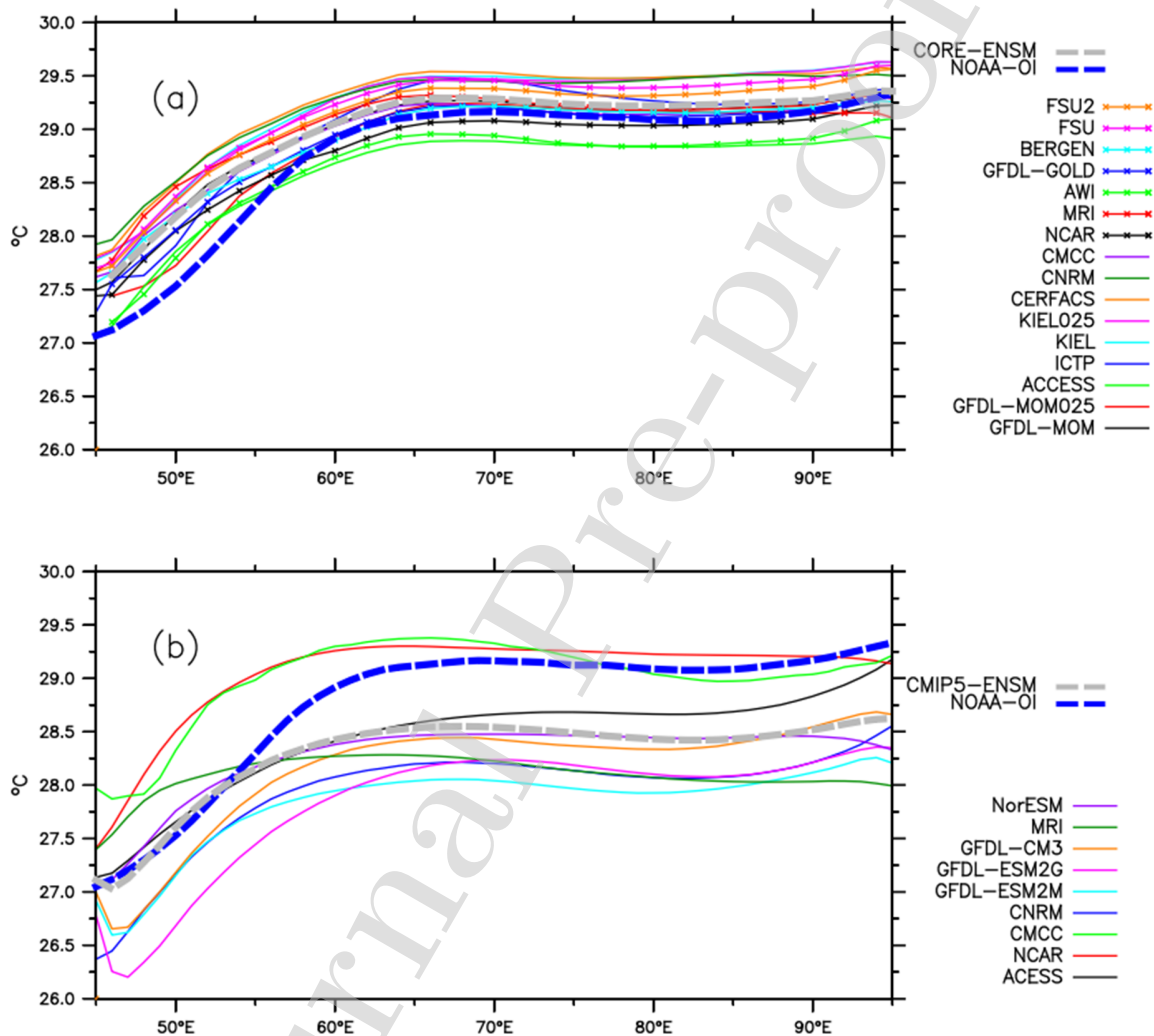
960 **4.2.3 Zonal SST variation along the equator**

961 Murtugudde and Busalacchi (1999) first reported that the mixed layer-thermocline
962 interactions in the EEIO potentially imply a coupled feedback. Furthermore Saji et al. (1999) and
963 Webster et al. (1999) showed that coupled feedbacks in the equatorial Indian Ocean are critical
964 for variability in the tropical Indian Ocean. This variability mode is known as the IOD. Many
965 studies have since shown that IOD is intrinsic to the Indian Ocean with a potential kick from the
966 massive western Pacific convection center (Annamalai et al., 2003; Annamalai and Murtugudde,
967 2004; Saji et al., 2006; Wang et al., 2016; Wang and Wang, 2014).

968

969 Figure 14a shows the east-west SST gradients from CORE-II simulations and results
970 from CMIP5 simulations are shown in Figure 14b. Observational estimates for mean SST in the
971 eastern and western regions are 29.6 °C and 27.2 °C respectively (Figure 14a). All models show
972 a warm bias of up to 0.9 °C in the western equatorial Indian Ocean (45-60 °E) (Figure 14a). This

973 sort of bias concentrated on the western equatorial IO would have implications for the modes of
 974 interannual variability. Observations show a sharp gradient at 65 °E and nearly constant values
 975 of 29.3 °C in between 65-95 °E with a dip of 29.1 °C at 80 °E. All models show nearly constant
 976 SST between 65-95 °E with a spread of +/-
 977



978

979

980 Figure 14: Annual mean SST along the equator from (a) CORE-II models (b) CMIP5 models,
 981 their ensemble mean and NOAA-OI observations are also shown in thick gray and blue colors.

982
983 0.5 °C compared to observations. The KIEL group of models as well as FSU and FSU2 represent
984 the upper estimates of SST along the equator, while AWI and ACCESS show a cold bias
985 between 65-95 °E providing the lower SST estimate of the ensemble. The CORE-II ensemble
986 mean shows a general warm bias stronger evolved west of 65 °E. In contrast to the CORE-II
987 forced simulations, most CMIP5 simulations show colder SST throughout the basin as well as a
988 large model spread (figure 14b). Overall, CORE-II models show a higher skill in simulating
989 zonal SST distribution along the equator than the CMIP5 models.

990
991 We summarize this analysis by noting that the seasonal variation of SST in different sub-
992 regions in the Indian Ocean is well captured by the CORE-II models compared to the coupled
993 CMIP5 simulations. In particular, the bi-modal SST variability over the AS, the BoB and the
994 EEIO are well reproduced in CORE-II models, while the absolute climatological values differ
995 regionally and seasonally by up to 1.8 °C, with a broad range of variations shown by the models.
996 However, both CORE-II and CMIP5 models exhibit deficiencies in capturing the equatorial
997 Indian Ocean dynamics, as evident from the flat zonal SST gradient and the warm bias over the
998 open ocean upwelling dome south of the equator. The seasonal prediction skill for the tropical
999 SST anomalies are a major predictability source for monsoon precipitation in the coupled
1000 models and is closely linked to the ability to simulate the SST mean state (Lee et al., 2010).
1001 We conjecture that the relatively poor skill of the coupled models at simulating the mean SST
1002 in the Indian Ocean versus the higher skill in the CORE-II simulations indicates the role for
1003 coupled feedbacks that amplify ocean biases. These results offer a useful benchmark for use in
1004 developing methods to reduce biases in coupled prediction models.

1005

1006 **4.3. Surface Salinity and barrier layer**

1007

1008 In this section, we study the behavior of the surface salinity and associated BL within the
1009 Indian Ocean. Much of this behavior is affected by precipitation and river runoff forcing, with
1010 CORE-II simulations using interannually varying monthly mean precipitation derived from

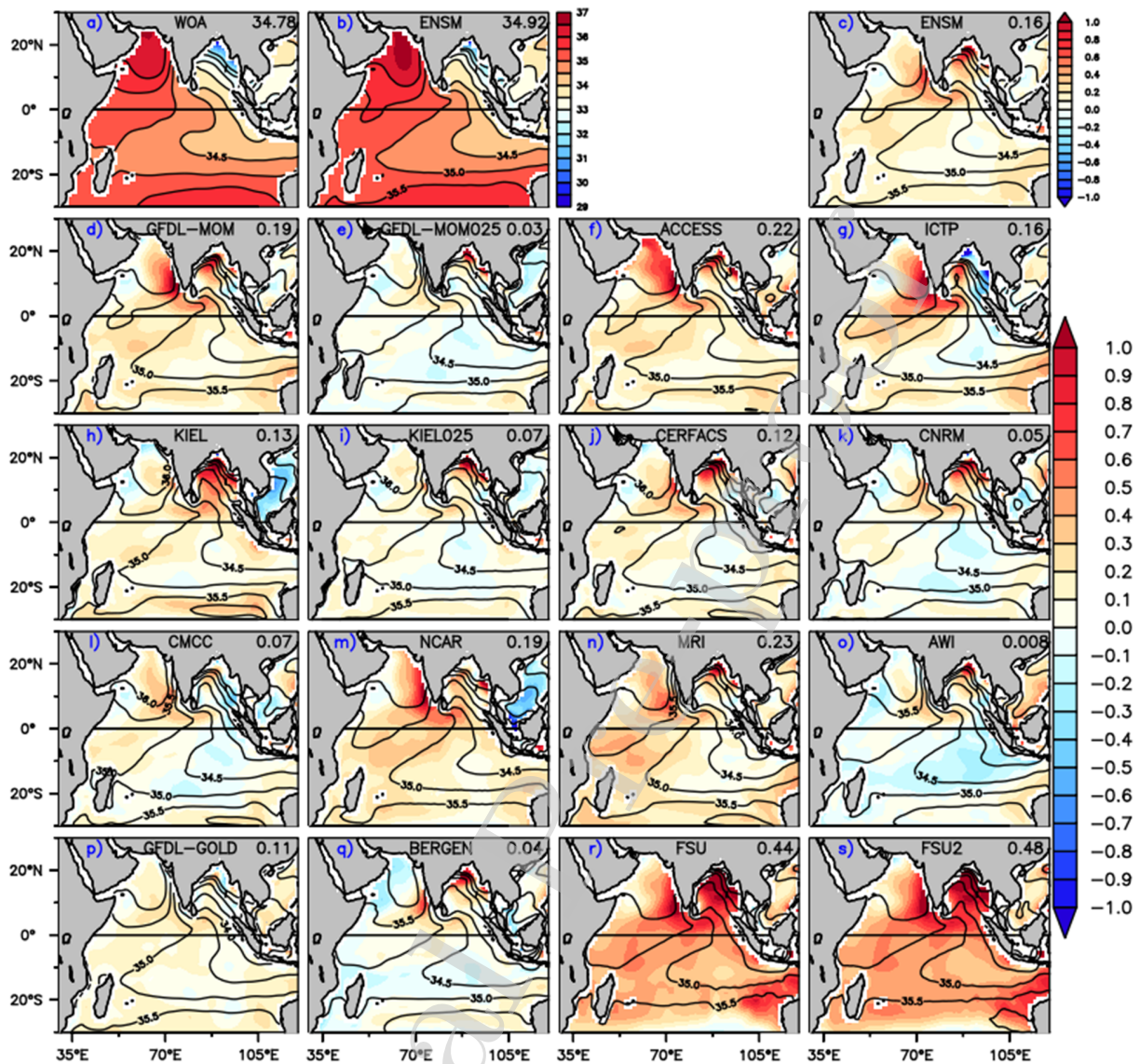
1011 satellite corrected rainfall and interannually varying monthly mean river runoff (Dai et al.
1012 2009; Danabasoglu et al. 2014). Additionally, as detailed in Griffies et al. (2009) and
1013 Danabasoglu et al. (2014), CORE-II simulations are integrated with surface salinity restoring in
1014 order to reduce long-term drifts in the thermohaline properties of the models. Details are given in
1015 Section 3.1. The monthly climatology is computed over the period 1982 to 2007 for all models.

1016

1017 **4.3.1 Surface Salinity**

1018

1019 Figure 15 shows the annual mean SSS from the CORE-II models and their biases with
1020 respect to observations. Figure 15a shows the SSS from WOA observation, Figure 15b shows the
1021 ensemble mean from all models and Figure 15c shows the ensemble bias. Asymmetry in the SSS
1022 distribution with higher salinity in the AS and lower salinity in the BoB is seen in the
1023 observation and is reproduced by all simulations. However, all models show a basin wide
1024 positive salinity bias with large values over the northern BoB and the southeastern AS.
1025 Interestingly, the biases are much smaller along the observed salinity fronts aligned towards
1026 Madagascar Island from Sumatra. Some models, such as CNRM, CMCC, AWI and BERGEN,



1027

1028 Figure 15: Annual mean SSS bias (model minus observation) from CORE-II simulations (color
 1029 shade) with contours for the annual mean. The model ensemble mean bias is shown in the upper
 1030 right panel. Observed annual mean SSS from WOA is shown in the upper left panel. Ensemble
 1031 mean from all CORE-II models is shown in the upper middle panel. Contour levels for WOA
 1032 and all models are same. Units are in practical salinity. Basin averaged SSS values from WOA
 1033 observation, ensemble mean as well as basin averaged bias of individual models are shown in
 1034 upper right corner of each panel.

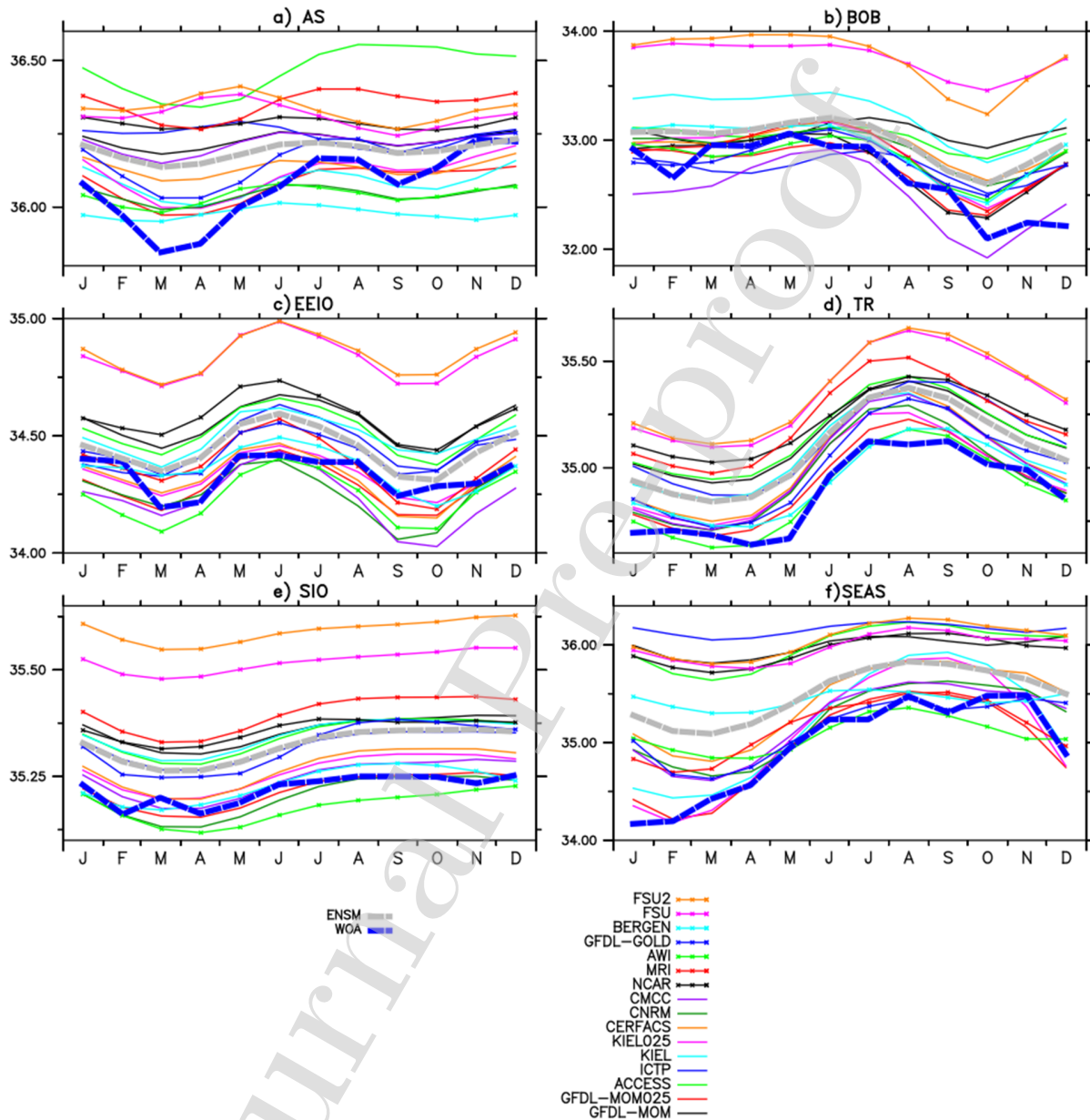
1035
1036 even show lower salinity along this path. Due to this opposite sign of the bias, the basin averaged
1037 salinity bias is much weaker in these models. Both FSU models show a basin wide bias of 0.44
1038 and 0.48 psu, which is much larger than the ensemble mean bias (0.16 psu) as well as the bias in
1039 other models. The annual mean basin averaged salinity from WOA observation is 34.77 psu and
1040 over the northern BoB it reaches down to 32.12 psu due to the strong influence of river runoff.

1041
1042 In the northern BoB, the mean SSS bias in the individual models range between 0.3 and
1043 0.5 psu with higher values in FSU and FSU2 (2.1 and 1.8 psu, respectively). The slight
1044 improvement in FSU2 may be due to an improvement in model physics. The low-salinity water
1045 flowing out of the BoB along its eastern boundary (Shetye et al., 1996; Han and McCreary 2001;
1046 Jensen, 2001; Sengupta et al., 2006) crosses the basin with the SEC and reaches to the western
1047 Indian Ocean to Madagascar. The observed low salinity band south of the equator between 5 °S
1048 and 20 °S is well reproduced in all models. This low salinity region also corresponds to the
1049 region of [Inter Tropical Convergence Zone \(ITCZ\)](#) associated with locally large precipitation
1050 (Yu, 2011; Perigaud et al., 2003). The annual SSS bias is only 0.11 psu over the entire basin in
1051 GFDL-GOLD (Figure 15p). KIEL shows a large positive bias over the BoB. ACCESS, GFDL-
1052 MOM and NCAR show a large positive bias over the eastern AS. A positive bias over the SEAS
1053 can be attributed to the inability of these models to transport low salinity water by the EICC.
1054 This behavior can be seen in the depth versus time plots of salinity over this region as well (see
1055 Figure 22a and sec 4.4.2). SSS simulations improve significantly upon refining the model's
1056 horizontal resolution (KIEL025, GFDL-MOM025) as compared to their coarser counterpart. Han
1057 et al. (2001) reported that advection of salinity by a coastal current plays an essential role in the
1058 salinity balance. This may be the reason for better salinity simulation in a higher resolution
1059 model. This result contrasts to the SST results (Figure 5), which revealed only minor sensitivity
1060 to horizontal grid resolution.

1061
1062 Unlike SST, spatial structure of annual mean SSS and its bias are roughly symmetric
1063 across all seasons. However, different regions differ in seasonal SSS variations (Figure 16). The

1064 minimum surface salinity over the NIO is seen in October over the north BoB (Figure 16b;Rao
 1065 and Shivakumar, 2003; Sengupta et al., 2006).

1066



1067
 1068 Figure 16: Seasonal cycle of sea surface salinity from all CORE-II models and WOA observation
 1069 over different sub-regions of the Indian Ocean (see sec 3.4 for sub-regional specifications).

1070

1071 FSU and FSU2 seasonal cycles are outliers with a systematic positive bias of ~ 1 psu in the BoB
1072 (Figure 16b) and in the other regions as well with slight reduction in bias. As in the case of SST,
1073 SSS also shows large inter-model spread. In the BoB, only AWI is able to capture the seasonal
1074 cycle with lowest observed salinity in October (Figure 16b). Peak river runoff and the integrated
1075 summer rainfall lead to a SSS minimum in October. EEIO shows two salinity lows during the
1076 inter-monsoon months of Mar-Apr and Oct-Nov in the seasonal SSS variations (Figure 16c).
1077 These lows are associated with precipitation due to ITCZ seasonality over this region. The
1078 models are able to capture this semi-annual signal, but with varying biases and large inter-model
1079 spread. SSS does not change significantly over the SIO on seasonal time scales (Figure 16e). It is
1080 almost constant in WOA at 35 psu and the models are able to capture this near constant SSS
1081 throughout the year. Almost all models show a positive salinity bias in the AS, the BoB and the
1082 SEAS (Figure 16a, b, f), but in FSU and FSU2 this bias is seen in all the sub-regions.

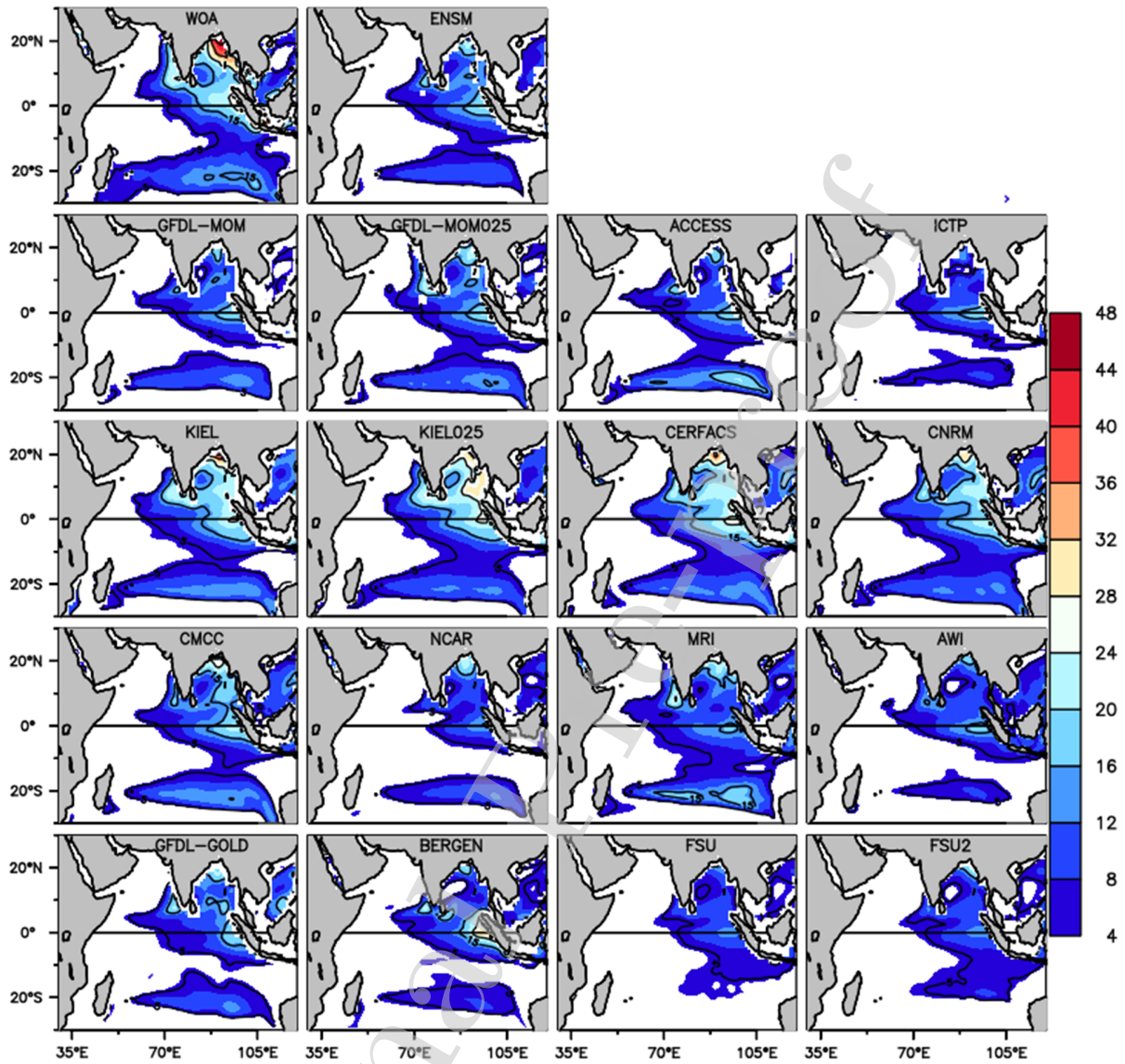
1083
1084 In summary, the CORE-II SSS shows good representation of the asymmetric salinity
1085 pattern in the Indian Ocean, with high salinity water in the AS and low salinity water in the BoB.
1086 Most of the models underestimate the freshening in the northern BoB, with improvement seen in
1087 high resolution eddy permitting models.

1088
1089 **4.3.2 Barrier layer and its impact on SST bias**
1090 The time varying depth of the mixed layer is a crucial parameter for the mixed layer heat budget
1091 and hence for the SST (Chen et al., 1994; Qiu et al., 2004). Challenges of ocean models are to
1092 simulate this time varying MLD over global and regional oceans. In the Indian Ocean, the upper
1093 ocean stratification in temperature and salinity does not necessarily coincide. Depending upon
1094 the freshwater input, it differs particularly over the BoB, the EEIO and the SEAS (Thadathil et
1095 al., 2007; Sprintall and Tomczak, 1992). Owing to its unique geographical location, the BoB
1096 receives large amount of freshwater both from local precipitation and river discharge, estimated
1097 at about 4700 and 3000 km³/yr, respectively (Sengupta et al., 2006). Annual freshwater input
1098 exceeds evaporation and hence it makes the BoB relatively **fresh** compared to the rest of the
1099 basin. This low saline water is confined within a thin layer near the surface and makes the top of

1100 the halocline shallower than the top of the thermocline. This unique structure makes the mixed
1101 layer limited by the top of halocline and an isothermal layer depth (ILD) limited by top of the
1102 thermocline. The difference of these two layers is called a BL (Thadathil et al., 2007; Sprintall
1103 and Tomczak, 1992). BL also form over the SEAS and the EEIO. This layer inhibits vertical
1104 mixing and hence restricts entrainment cooling from the thermocline and affects the mixed layer
1105 heat budget and SST variations. Observational studies show that on a seasonal scale this layer
1106 thickness is ~10-60 m (de Boyer Montégut et al., 2007; Thadathil et al., 2007). It has been shown
1107 in these studies that BL formation potentially plays a significant role in mixed layer heating. In
1108 this section, we assess the BL from all the simulations and its effect on SST. The ILD and MLD
1109 are computed based on Kara et al. (2000) corresponding to temperature change of 1 °C at the
1110 surface.

1111
1112 The annual mean BL from all model simulations and WOA is shown in Figure 17.
1113 Sprintall and Tomczak (1992) show that three regions (EEIO, north BoB and SEAS) consistently
1114 display a significant BL of 10-50 m thickness throughout the year. There is a BL in the north
1115 BoB (Vinayachandran et al., 2002; Thadathil et al., 2007; de Boyer Montégut et al., 2007) due to
1116 inflow of freshwater from adjoining rivers and local precipitation during the Indian summer
1117 monsoon, thus making the mixed layer very thin (~ 10-20 m) and in turn thickens the BL (Figure
1118 17). The observed annual mean BL over the northeastern BoB is ~ 40-44 m (Figure 17). The
1119 northwestern BoB shows slightly thinner BL, mainly since the western BoB experiences a
1120 regime of excess evaporation as compared to the eastern BoB (Sprintall and Tomczak, 1992;
1121 Pokhrel et al., 2012b). The BL in the western BoB is maintained by the river runoff received
1122 during summer monsoon (Vinayachandran et al., 2002; Sengupta et al., 2006). The east-west
1123 difference in BL over BoB is most prominently simulated by KIEL and KIEL025. Other models
1124 are unable to capture this east-west gradient.

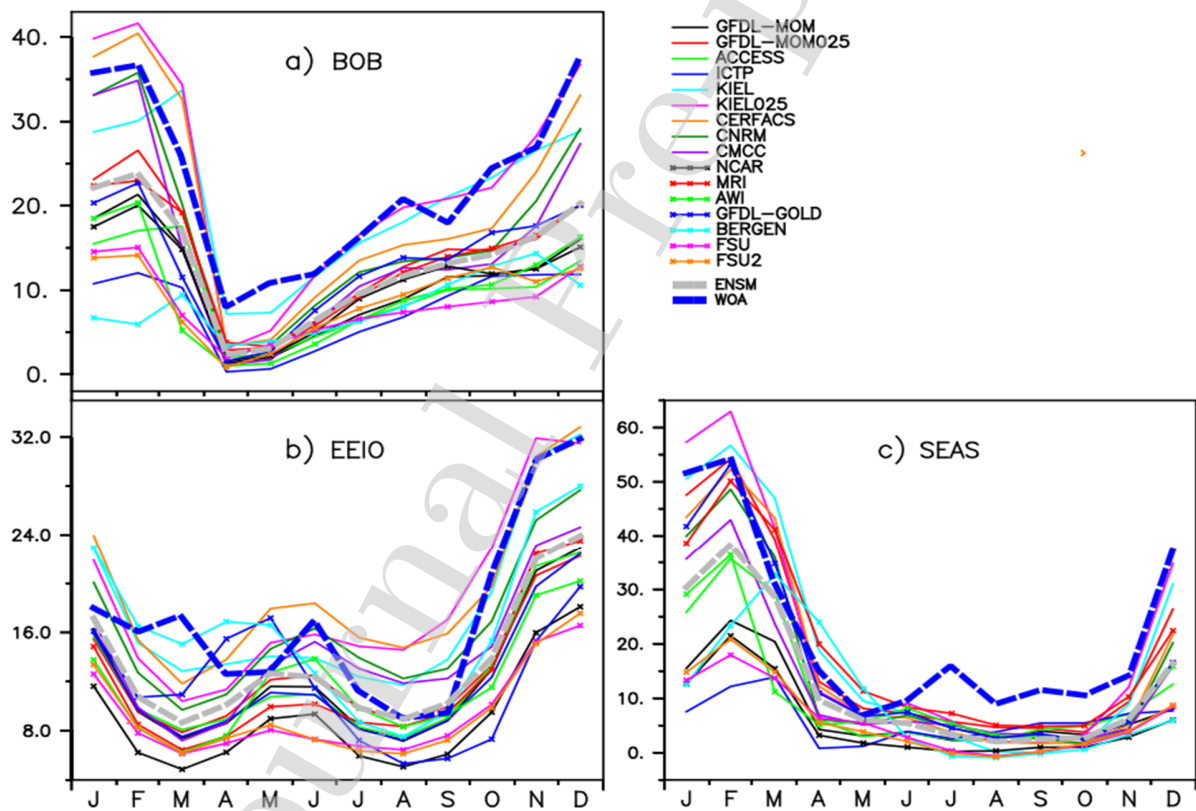
1125



1126

1127 Figure 17: Annual mean barrier layer thicknesses (BL) in meters from CORE-II simulations and
 1128 WOA observation. The observed annual mean BL from WOA is shown in upper left panel. The
 1129 ensemble means BL from all simulations is shown in the upper middle panel. The individual
 1130 model performances are shown in other panels.

1131 To see how the models simulate the seasonal variation of the BL, we show the time series
 1132 of the BL averaged over the BoB, the SEAS and the EEIO in Figure 18. Observations show that
 1133 the seasonality in the BL becomes most prominent over the BoB during Dec-Jan when it
 1134 becomes ~40 m thick (Figure 18a) and is mainly driven by substantial river runoff into the north
 1135 BoB. Most of the models are unable to capture this winter time thick BL in the northern BoB,
 1136 though the NEMO group of models (KIEL at both resolutions, CERFACS, CNRM and CMCC)
 1137 do a reasonable job with KIEL and CERFACS have BL slightly thicker than observed value.
 1138 MOM and the HYCOM class of models are unable to capture this BL. Notably, horizontal
 1139 refinement of grid resolution (eg., MOM025) improves the BL simulations (figure 31b). We
 1140 conjecture that the inability of the MOM class of models to simulate the observed BL, in contrast
 1141 to the NEMO class, arises from differences in boundary layer parameterizations.



1142

1143 Figure 18: Seasonal cycle of Barrier Layer Thickness over (a) Bay of Bengal, (b) Eastern
1144 Equatorial Indian Ocean, and (c) South Eastern Arabian Sea from all CORE-II model
1145 simulations and WOA observations.

1146 The second region with a prominent BL occurs over the EEIO west of Sumatra.
1147 Observations show an annual mean BL thickness of ~20-25 m with seasonality and peaks during
1148 Nov-Dec with a BL thickness of 30 m. KIEL and CERFACS capture the observed mean and
1149 seasonality (Figure 18b). The remaining NEMO models also capture this annual mean and
1150 seasonality with reasonable accuracy. The remaining models underestimate the BL. FSU and
1151 FSU2 models underestimate the BL by ~10 m, and during the peak season (Nov-Dec) it is
1152 doubled (20 m). The presence of a BL throughout the year is due to the local maximum in P-E
1153 present throughout the year (Oberhuber, 1988).

1154 The SEAS is the third region where a BL is prominent. Observations show a thick BL
1155 (~30 m) over the SEAS (Figure 18c). Once again, the NEMO class of models performs better
1156 than the other models. The other class of z-coordinate models based on MOM (MOM,
1157 MOM025, ICTP, and ACCESS) and NCAR as well as the isopycnal model BERGEN provide a
1158 reasonable simulation of the location and amplitude of the BL. In the hybrid vertical coordinate
1159 model FSU and FSU2, BL amplitude is largely underestimated as compared to WOA
1160 observation. The seasonal cycle of the BL shows that the BL is a maximum in January-February
1161 (~ 50 m) and then gradually decreases and is almost annihilated in April (Shenoi et al., 2004)
1162 (Figure 18c). Large spread (10-55 m) is seen among the models in simulating the peak BL during
1163 January-February. The superiority of the NEMO model class in reproducing the seasonal cycle
1164 of BL can be seen with KIEL025, which is able to capture the peak magnitudes. Although the
1165 MOM simulations are unable to reach the highest value for the BL thickness, the increased
1166 resolution clearly improves the peak magnitude. FSU and FSU2 are notably poor in reproducing
1167 the seasonal cycle. The inability of reproducing the BL is mainly due to the inability to bring the
1168 low salinity water from the north BoB by the EICC during November-January (Shankar et al.,
1169 2002; Rao and Shivakumar, 2003), as explained in Section 4.2.

1170

1171 4.4. Subsurface Features

1172

1173 4.4.1 Subsurface Temperature

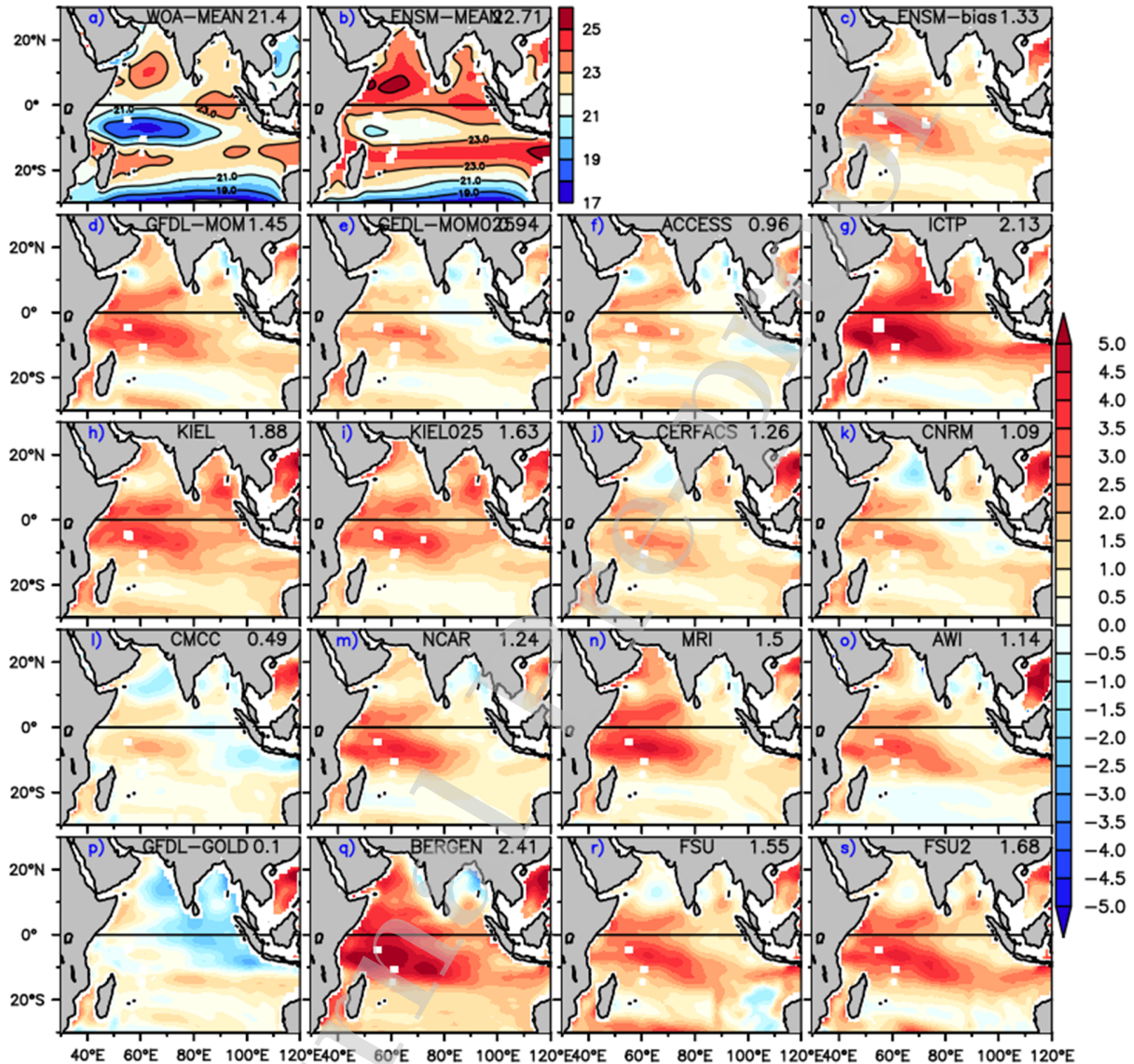
1174 The spatial distribution of subsurface temperatures in the tropical Indian Ocean has
1175 distinct regional characteristics (Colborn, 1975). It is well documented that all climate models
1176 tend to render a diffuse thermocline with mostly deeper than observed thermocline (Cai and
1177 Cowan, 2013; Tao et al., 2015; Flato et al., 2013). The models' ability to simulate the temporal
1178 and spatial variability, particularly on a seasonal timescale, determines how well the model
1179 performs in terms of monsoon strength and variability. It has been reported in IPCC-AR5
1180 (Stocker et al., 2013) that the thermocline biases in CMIP5 have not improved much despite the
1181 increase in resolution compared to CMIP3 (IPCC AR4) (Cai and Cowan, 2013; Tao et al., 2015;
1182 Flato et al., 2013). It is important in this context to investigate how the CORE-II simulations,
1183 perform in simulating subsurface dynamics and thermodynamics.

1184

1185 The average thermocline depth in the NIO is about 100 m (Rao and Sivakumar, 2000;
1186 Yokoi et al., 2008; Yokoi et al., 2009). We thus take 100 m as a reference depth, with Figure 19
1187 showing the 100 m temperature bias from models relative to WOA. The WOA shows three
1188 distinct warm regions over the AS, the EEIO, and along 25 °S-10 °S in the south Indian Ocean.
1189 The relatively cooler region over the thermocline ridge corresponds to the open ocean upwelling
1190 region (Xie et al., 2002; Schott et al., 2009). Similar to the SST distribution, all models show a
1191 warm bias over this region as well as the western equatorial Indian Ocean, with ICTP and
1192 BERGEN showing the largest bias (>3 °C) and CMCC and GFDL-GOLD showing the smallest
1193 in these regions. The basin averaged bias is largest in BERGEN (2.4 °C) followed by ICTP (2.1
1194 °C), whereas GFDL-GOLD shows a negligible bias of 0.1 °C. The refined resolution reduces the
1195 bias especially in GFDL-MOM025. Among the NEMO group of models, CMCC performed best
1196 with a basin averaged bias of 0.49 °C. Interestingly, both the isopycal (BERGEN) and hybrid
1197 class of models (FSU, FSU2) show larger biases than the z-coordinate models. This result

1198 indicates a common weakness of these models in the representation and/or parameterization of
 1199 near surface physical processes.

1200



1201

1202 Figure 19: The upper left panel shows the temperature (degrees Celsius) at 100 m depth from
 1203 WOA; the upper middle panel shows the same from the CORE-II ensemble and the upper right
 1204 panel shows the ensemble bias at 100 m depth with respect to WOA. The remaining panels show

1205 the temperature bias (model minus observation) at 100 m depth from all CORE-II individual
1206 models. The basin averaged values are given in upper right corner of each panel.

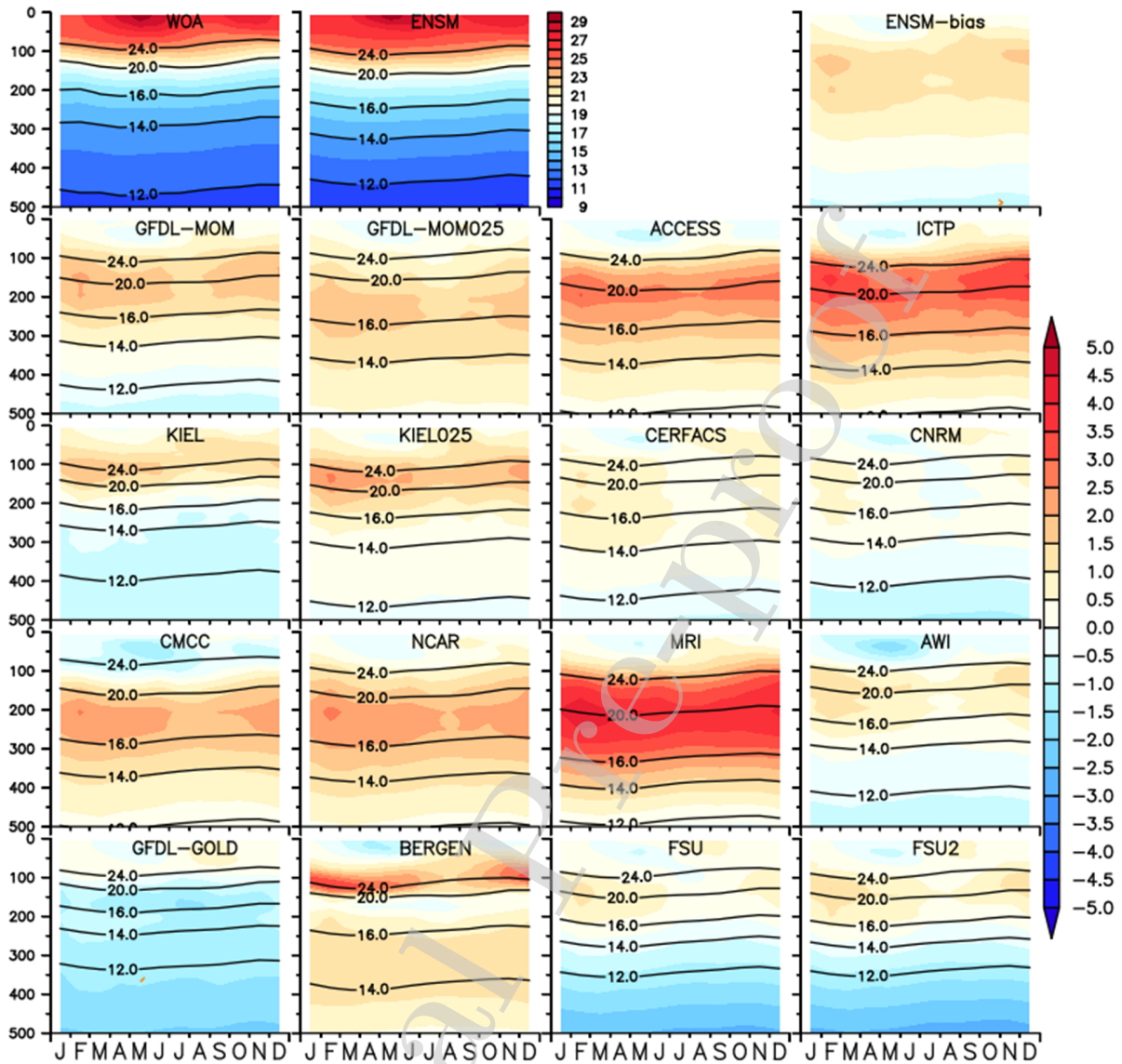
1207

1208 To see how the models capture the seasonal cycle of subsurface temperature, we plot the
1209 depth versus time mean temperature and the corresponding bias over different regions. The
1210 vertical levels of all models are regridded to MOM depth levels. Figure 20 shows upper ocean
1211 mean temperature from WOA observations and from the 16 model CORE-II ensemble. The
1212 biases of individual models are also shown in shade with mean values represented in contours.
1213 The warm surface temperature seen in April-May (Figure 20) penetrates down to 40 m with
1214 values similar to the surface (~ 30 °C) in the WOA observations, which is well represented by the
1215 CORE-II ensemble mean. The upper ocean (0-100 m) is warmer throughout the year with
1216 maximum of 30 °C right at the surface during April/May, but decreasing to 26 °C near 40 m.
1217 Below 100 m, temperature changes sharply and reaching ~ 11 °C at 500 m depth. The ensemble
1218 mean temperature variation is close to observed values. The ensemble mean bias in the
1219 thermocline depth and below (100-300 m) shows much lower values (~ 1 °C) compared to many
1220 individual models, thus indicating a non-unidirectional bias of the models. The MOM group of
1221 models (GFDL-MOM, GFDL-MOM025, ICTP and ACCESS) shows a large bias in the
1222 thermocline with a range between 1-3 °C, with the highest bias in the coarsest model ICTP.
1223 Among all models, MRI shows the maximum bias of $\sim 4-5$ °C in the thermocline region. In the
1224 AS for the NEMO group of models (KIEL, KIEL025, CERFACS, CNRM and CMCC), the bias
1225 in the thermocline region (100-200 m) is much less ($\sim 1 - 1.5$ °C) with almost negligible bias in
1226 CNRM. However, these biases are increased in the BoB and the EEIO. In contrast, the deeper
1227 layers (below 250 m) are much cooler (~ 1.5 °C) in GFDL-GOLD, FSU and FSU2 in the AS and
1228 this bias reduces in the BoB and the EEIO. These biases cancel each other out such that the
1229 model ensemble mean resembles the observations. In BERGEN, the thermocline shows a
1230 positive bias in the AS, whereas it shows a negative bias in the BoB. But it is much narrower
1231 relative to the MOM group of models (MOM, MOM025, ICTP and ACCESS), which shows a
1232 broader and more diffuse thermocline. Increased horizontal grid resolution does not show any

1233 significant change in the thermocline bias with slight increases in the thermocline bias for both
1234 GFDL-MOM025 and KIEL025 as compared to their coarser resolution counterparts (Figure 20).
1235 This behavior suggests that these models are producing enhanced spurious mixing due to
1236 numerical truncation errors (Griffies et al., 2000; Ilicak et al., 2012). All models show a cold and
1237 warm bias within 1 °C in the upper ocean (0-100 m), except AWI which shows a cold bias (~1-2
1238 °C) in the BoB. The thermocline continues to be diffuse and warmer for all models except
1239 GFDL-GOLD and BERGEN, which are cooler than WOA.

1240
1241 In the EEIO, observations show a stronger seasonal cycle of temperature down to 500 m
1242 depth, which is absent in other regions of the tropical IO (Figure 20c). All the models show a
1243 warm thermocline bias with ICTP and MRI showing the largest bias (~3-4 °C). Also note that
1244 the thermocline bias is largest in the EEIO as compared to AS and BoB. GFDL-GOLD is an
1245 exception among all models in all regions, with this model showing a cold thermocline bias with
1246 magnitude range of 0.5-1 °C. The positive subsurface bias is largest over the EEIO as compared
1247 to the AS and the BoB. The isotherms show a semi-annual signal with peaks in May and
1248 November that penetrate down to 500 m depth, which is in general present in all the models
1249 shown here. This deep penetration of seasonal variation in the isotherms is due to the
1250 convergence of warm water from the western Indian Ocean to the eastern Indian Ocean
1251 associated with the spring and autumn WJ (Webster et al., 1999; Rao and Sivakumar, 2000). The
1252 equatorial downwelling Kelvin waves generated in May–June and November propagate eastward
1253 and deepen the thermocline in the region off Sumatra (Du et al., 2005). The warm layer of 30 °C
1254 appears in February and gradually reaches a deeper layer in May and then again cooling down to
1255 29 °C in June. This near surface structure is only captured by the AWI simulation. The observed
1256 vertical temperature gradients are well captured in GFDL-GOLD. The EEIO shows a mixed
1257 response to refinement in grid resolution, with a slight bias reduction over the thermocline region
1258 but degradation below the seasonal thermocline. The ensemble mean variation closely followed
1259 the WOA but with a warm bias almost throughout the upper ocean with highest values in the
1260 thermocline region (Figure 20c).

1261



1262

1263 Figure 20a: Seasonal variation of mean temperature (degrees Celsius) as a function of depth
 1264 averaged over the Arabian Sea (contour) and its bias (model minus observation) in color. The
 1265 upper left panel shows the mean seasonal variation of temperature from WOA observations and
 1266 the upper middle panel shows the mean seasonal variation of temperature from the ensemble
 1267 mean and the upper right panel shows the ensemble mean bias with respect to WOA. Contour
 1268 levels for WOA observation, all individual models and its ensemble mean are same.

1269

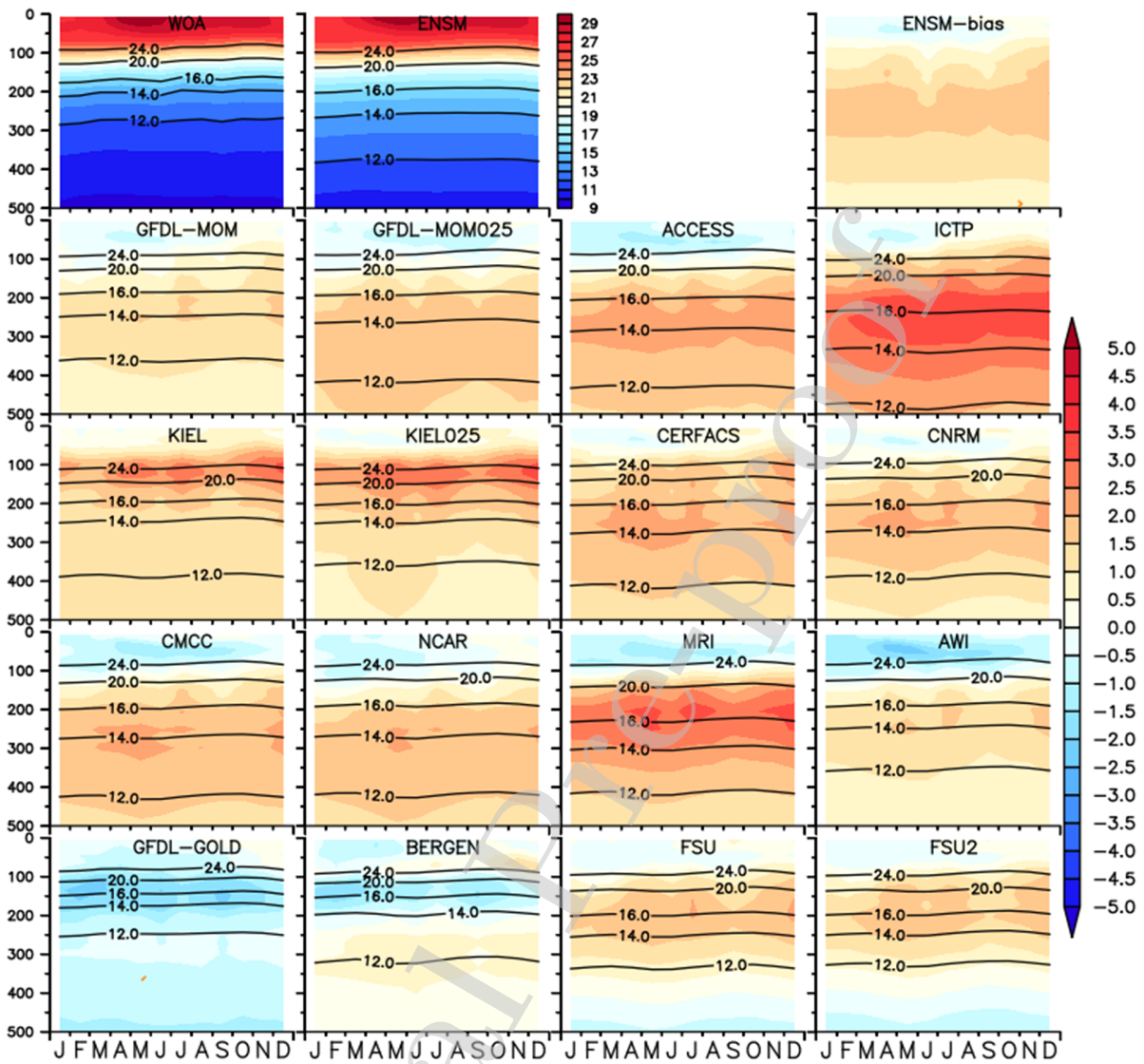
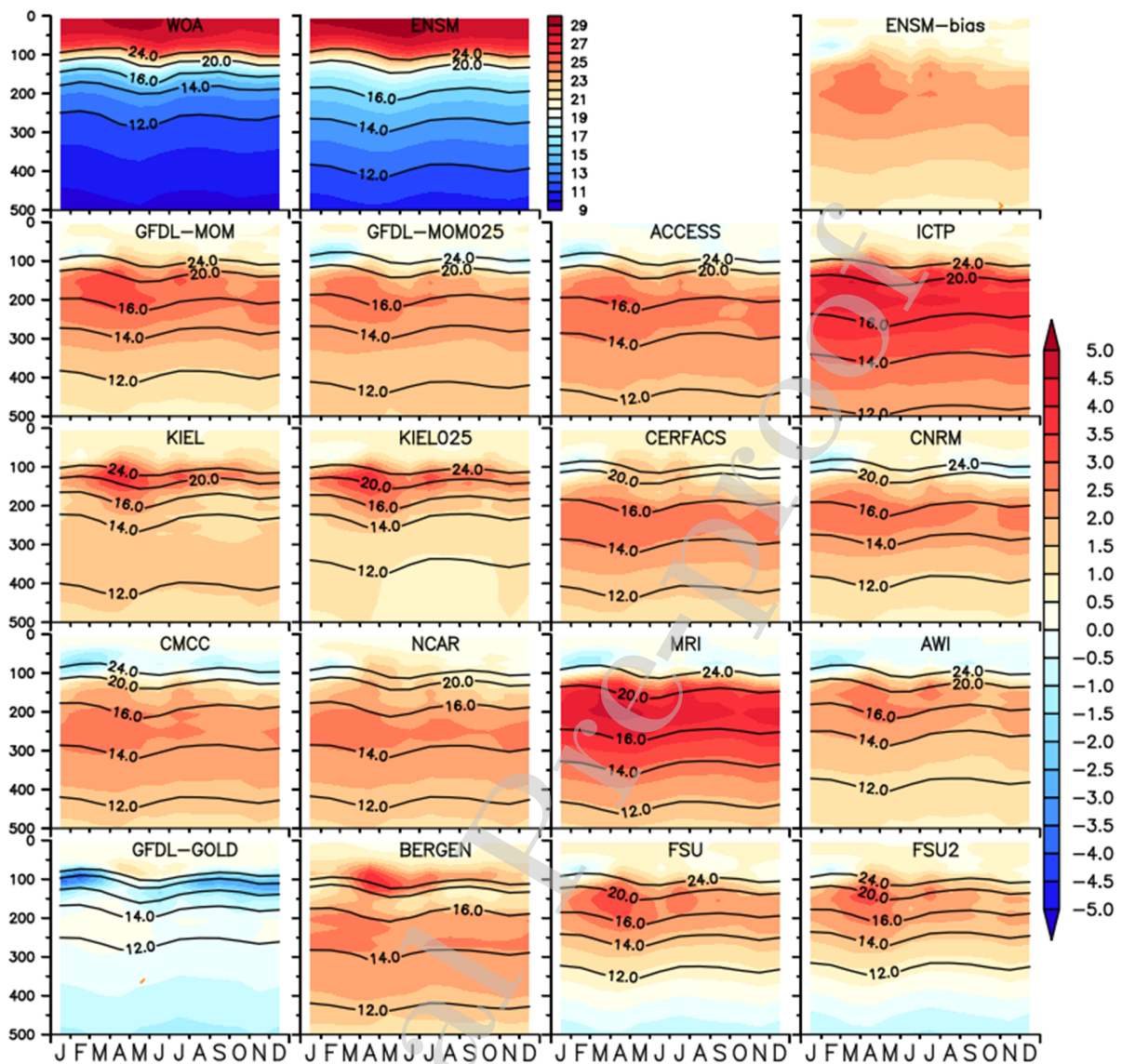


Figure 20b: Same as figure 20a but for the Bay of Bengal.



1272

1273 Figure 20c: Same as figure 20a but for the Eastern Equatorial Indian Ocean.

1274

1275

4.4.2 Subsurface Salinity

1276

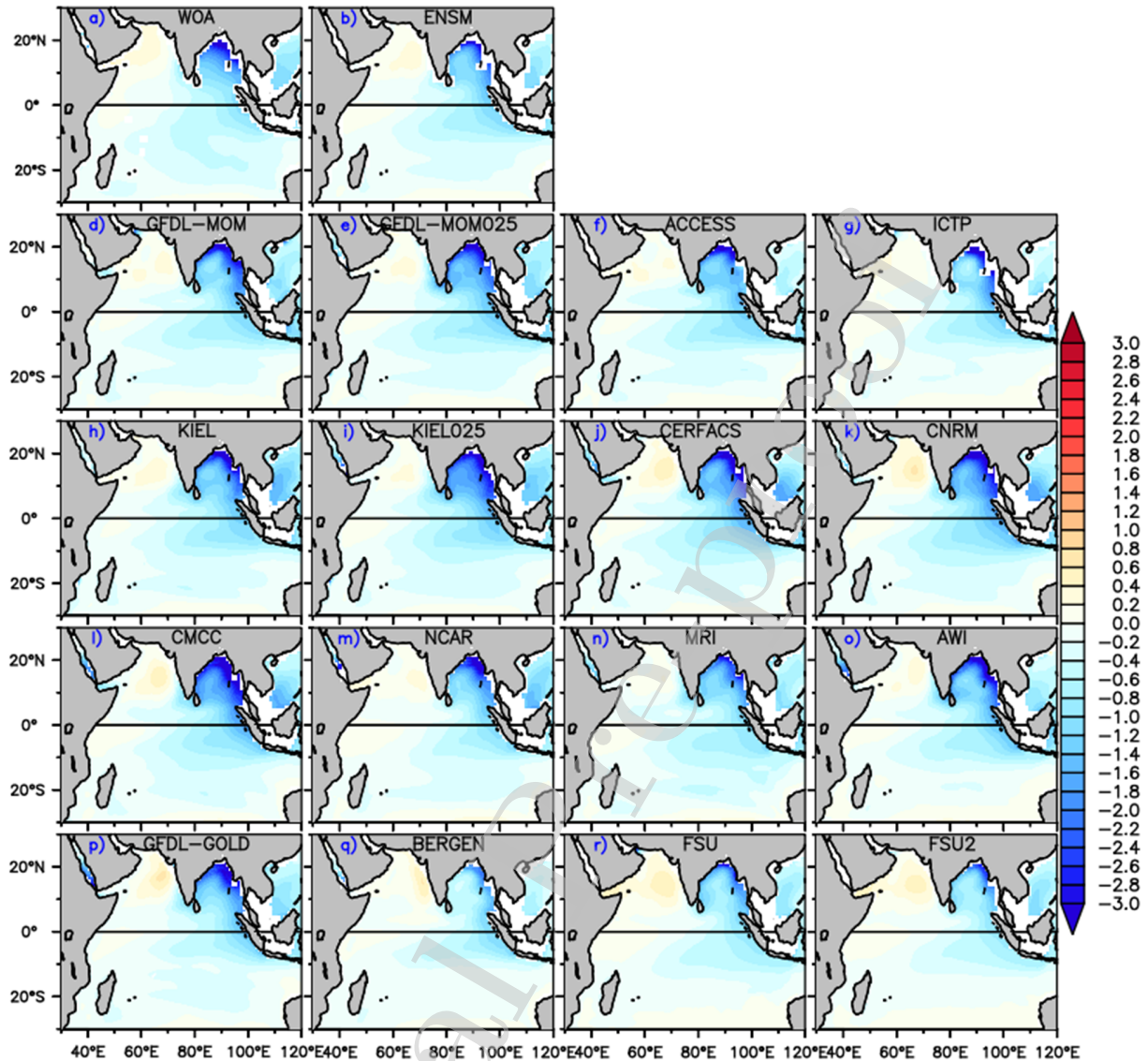
1277

1278

1279

Salinity stratification is mainly driven by the precipitation, evaporation and freshwater through river runoff and by the horizontal advection which also play an important role (Sprintall and Tomczak 1992). In the NIO near-surface haline stratification indirectly influences the evolution of the mixed-layer temperature by inhibiting the entrainment of subsurface cooler

1280 water (Moshonkin and Harenduprakash, 1991; Rao and Sanil Kumar, 1991; Rao et al., 1991; Rao
1281 and Sivakumar, 2003; Howden and Murtugudde, 2001; Shenoi et al., 2002; Shenoi et al., 2004;
1282 Miller, 1976). Many modelling studies have also shown that salinity plays an important role in
1283 the evolution of SST through MLD variations in the tropical Indian Ocean (Cooper, 1988;
1284 Masson et al., 2002; Masson et al., 2005; Sharma et al., 2007; Sharma et al., 2010; Durand et al.,
1285 2011; Fathrio et al., 2017b). These results motivate us to examine the vertical salinity gradients
1286 in the tropical Indian Ocean, with the vertical difference of salinity between surface and 100 m
1287 shown in Figure 21.



1288

1289 Figure 21: The upper left panel shows the annual mean salinity stratification (surface minus 100
 1290 m depth) from the WOA observation, and the upper middle panel shows the same for CORE-II
 1291 model ensemble mean. Remaining panels show the same for the individual CORE-II models.

1292

1293

1294

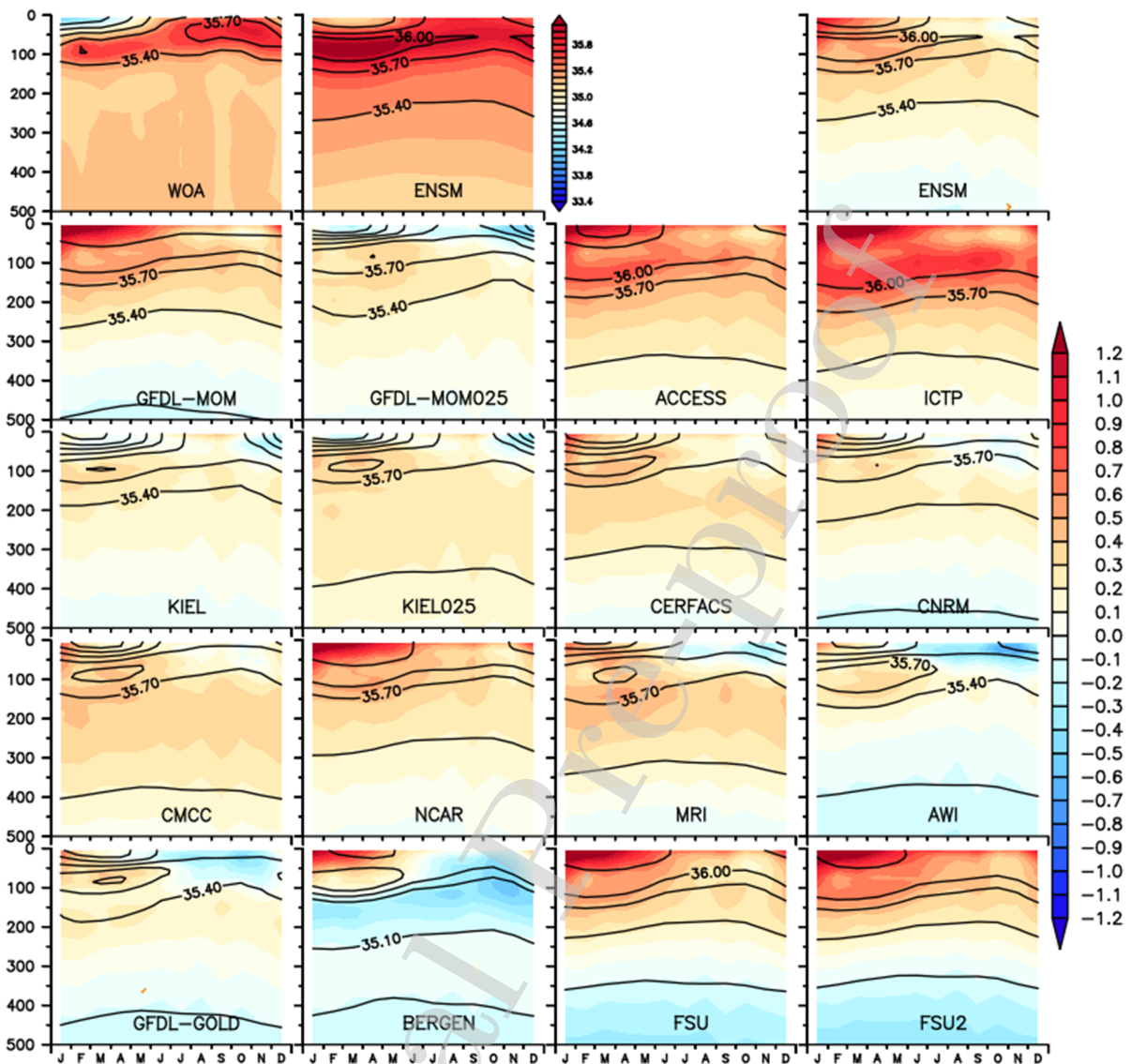
1295

The WOA shows three regions with strong haline stratification (>1.4 psu), namely: BoB, EEIO and SEAS. The strong vertical salinity differences are noticed primarily in the northern BoB. The observed difference is more than 3 psu over the northern BoB. The MOM group of

1296 models (GFDL-MOM, GFDL-MOM025, ACCESS and ICTP) and the NEMO class (KIEL,
1297 KIEL025, CERFACS, CNRM and CMCC) show their strongest stratification there as compared
1298 to WOA. The stratification is rather weak over the BoB in AWI, BERGEN, FSU and FSU2 and
1299 worst in ICTP as compared to WOA.

1300
1301 Rao (2015) has shown that within the Indian Ocean warm pool, near surface haline
1302 stratification exist over the southeastern AS, the southwestern BoB and the EEIO. They also
1303 reported that a strong coupling between near surface salinity stratification and the subsequent
1304 evolution of warm pool core is most prominently seen over the SEAS. The near-surface vertical
1305 salinity stratification over the SEAS is instrumental for the mini-warm pool in the AS (Durand et
1306 al., 2004), which is influenced by the advection of low salinity waters from the BoB during
1307 November–February (Rao et al., 2015). Hence, it is of particular interest to determine how the
1308 CORE-II models capture this stratification.

1309 Since salinity stratification mostly modulates the upper ocean temperature, we show the
1310 seasonal evolutions of salinity with depth over the SEAS, the BOB and the EEIO. The vertical
1311 levels of all models are regridded to MOM depth levels. Figure 22a shows the seasonal evolution
1312 of salinity with depth over the SEAS. The freshening in the upper ocean (0-50 m) during the
1313 period December-February is very prominent in the WOA observation. This freshening is
1314 reasonably reproduced by all models, but most prominently by KIEL, KIEL025 and MOM025.
1315 Below this fresh water, there is an intrusion of saltier water present throughout the year with
1316 peak values in October-November at about 50 m depth. This intrusion of saltier water is from AS
1317 high salinity water (ASHSW), as well as salty waters from the Red Sea and Persian Gulf (Shenoi
1318 et al., 1999, 1993, 2005; Levitus, 1983; Shetye et al., 1994; Durgadoo et al., 2017).



1319

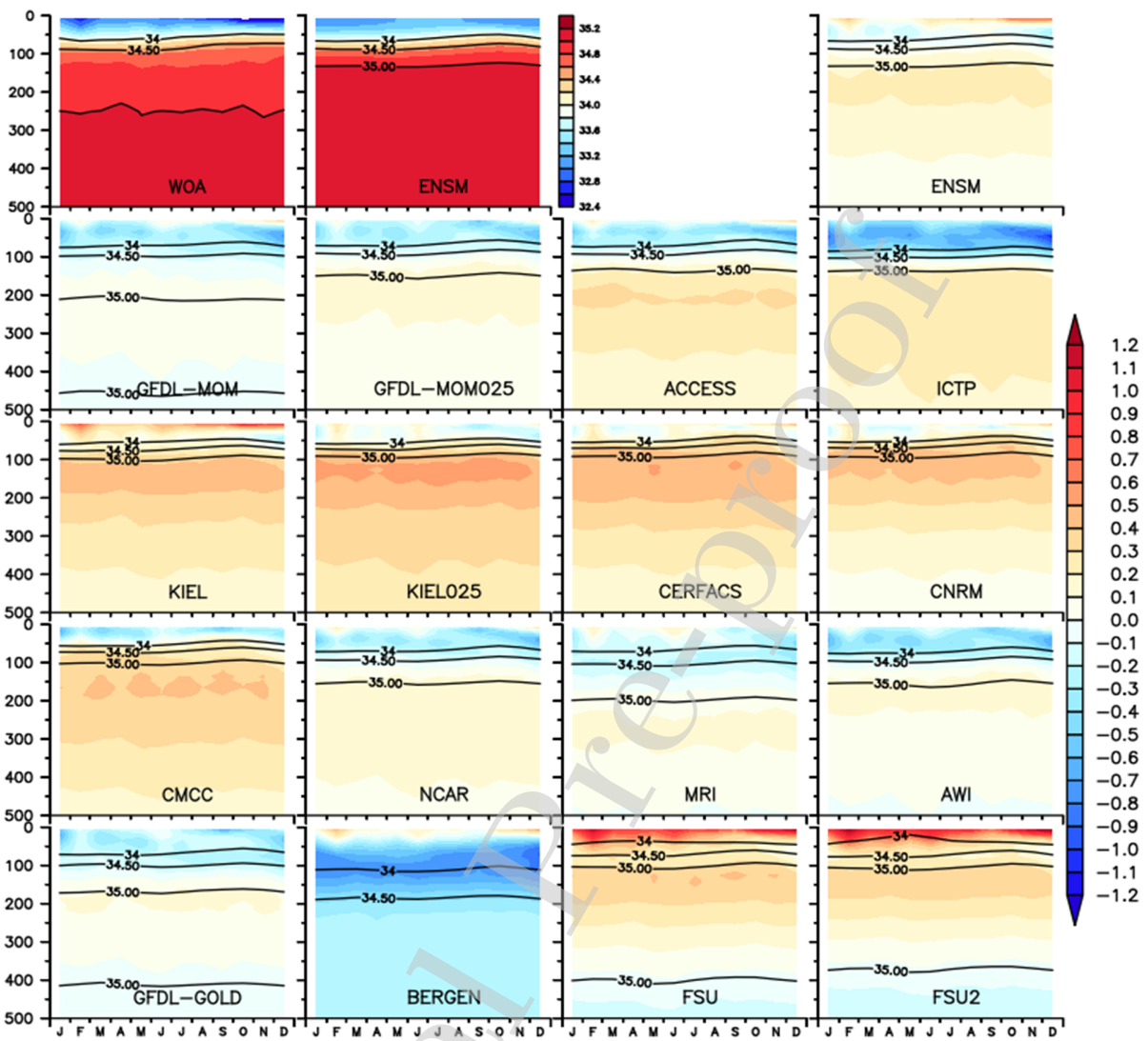
1320 Figure 22a: The upper left panel shows the seasonal variation of salinity with depth over the
 1321 south eastern Arabian Sea (SEAS). The top middle panel shows the same for CORE-II ensemble
 1322 mean, and the top upper right panel shows the ensemble mean bias. The remaining panels show
 1323 the individual CORE-II model bias (model minus WOA) in colors and its mean in contours.
 1324 Contour levels for WOA observation, all individual models and its ensemble mean are same.

1325 Below this saltier layer there are fresher waters seen in WOA, with a minimum at 200 m depth,
1326 which can also be seen in Figure 23c. Note that individual profiles based observations also show
1327 this structure (Shankar et al., 2005; Shenoi et al., 2005). The upper ocean is saltier during
1328 December-February in all simulations, with salinity larger than 1.2 psu in GFDL-MOM,
1329 ACCESS, ICTP, NCAR, BERGEN, FSU and FSU2. Aside from BERGEN, these models also
1330 show a saltier thermocline region compared to observations, as well as an increased salinity
1331 down to 300 m depth. Within the MOM models, ICTP and GFDL-MOM are unable to capture
1332 the winter time upper ocean freshening. A refinement of the horizontal resolution improves the
1333 simulation and allows the model to capture these low salinity values. Among all the models,
1334 BERGEN shows the freshest thermocline in contrast to a positive salinity bias for the
1335 thermocline in other models (Figure 22 a). The CORE-II ensemble mean variation captures the
1336 overall observed vertical structure, but with a positive salinity bias with largest value in the
1337 thermocline. The ensemble mean is also unable to resolve the local minimum in salinity below.

1338 Figure 22b shows the seasonal cycle of vertical salinity over the BoB. The upper ocean
1339 (0-100 m) is much fresher ~33-34 psu in observations than in the SEAS due to the proximity of
1340 large freshwater input by river runoff. MRI shows the smallest biases over depth and the
1341 seasonal cycle. Most models show an upper ocean (0-100 m) fresh bias, except FSU and FSU2
1342 which show a much saltier upper ocean. There is a rather large positive salinity biased
1343 thermocline in KIEL, KIEL025, CERFACS, CNRM, CMCC, FSU and FSU2, whereas
1344 BERGEN shows a much fresher thermocline as compared to WOA (Figure 22b). The remaining
1345 models show a slightly saltier (~0.3 psu) thermocline. In the EEIO region (Figure 22c) we see a
1346 fresh surface layer (0-100 m), which is mostly captured by all models except FSU and FSU2.
1347 Below 100 m, salinity shows only weak variation in observations, remaining nearly constant at
1348 35 psu. However, the simulations show a spread with a positive salinity bias in the upper
1349 thermocline and fresh bias in the deeper ocean (also see Figure 23c).

1350 Figure 23 shows the annual mean vertical salinity variations from WOA and CORE-II
1351 simulations averaged over different regions. The vertical salinity distribution shows distinct
1352 variations in the western Indian Ocean (AS, SEAS, TR) as compared to the eastern Indian Ocean

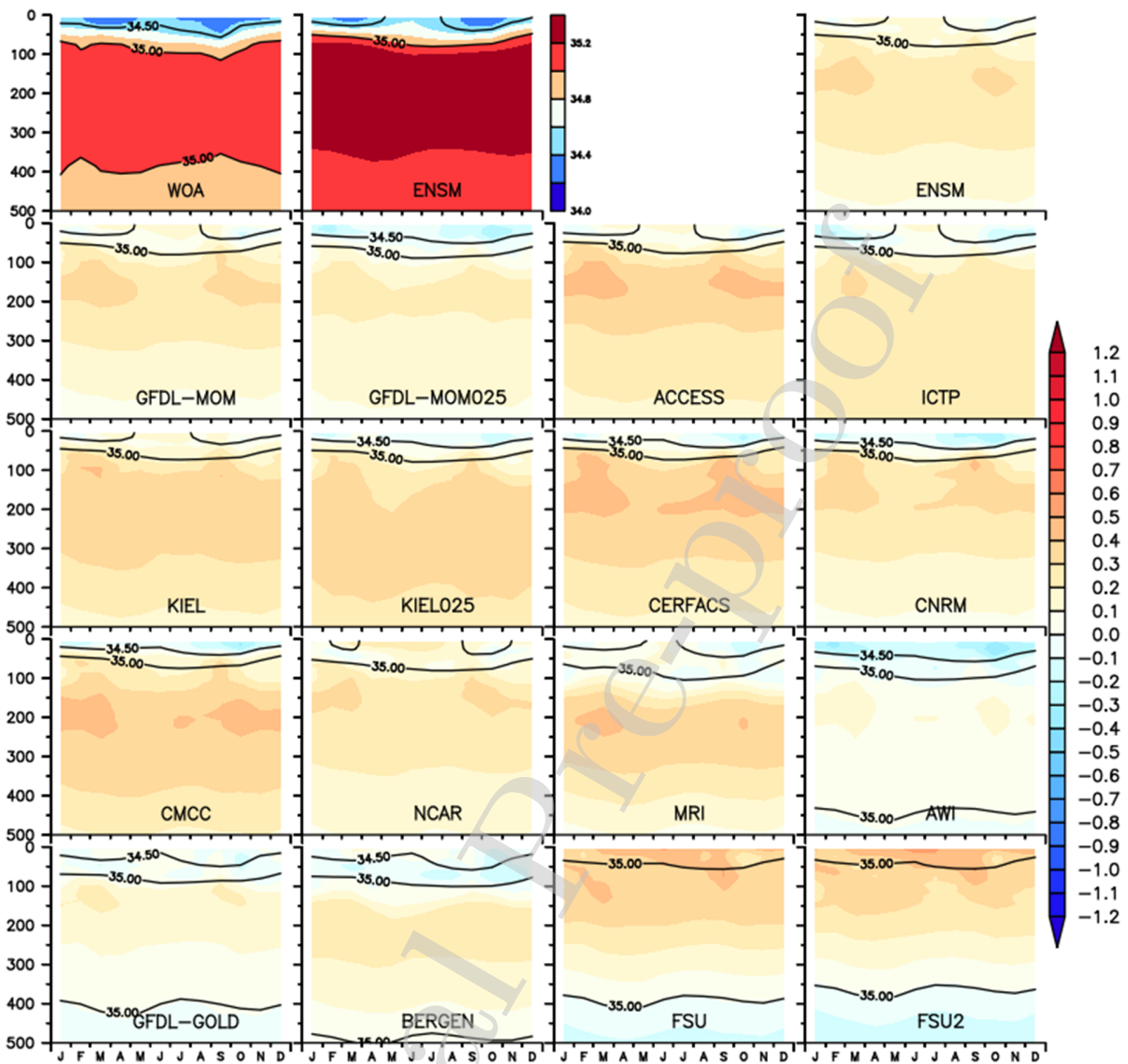
1353 (BoB and EEIO). Over the BoB and the EEIO, higher precipitation reduces surface salinity
1354 compared to the western basin, where evaporation dominates precipitation (Pokhrel et al., 2012b)
1355 thus leading to a saltier surface layer there. The observations show that in the AS the high
1356 surface salinity decreases rapidly with depth to 200 m then the observed salinity decrease is
1357 small, almost stable up to 800 m depth then the observed salinity decrease is small, almost stable
1358 up to 800 m depth, while deeper a stronger freshening occurs again. All simulations show saltier
1359 upper ocean, except for BERGEN and AWI, which show a fresh bias. Below 200 m all models
1360 reproduce a fresh subsurface layer. Salinities in FSU and FSU2 are the freshest of all
1361 simulations.



1362

1363 Figure 22b: Same as figure 22a but for the Bay of Bengal.

1364

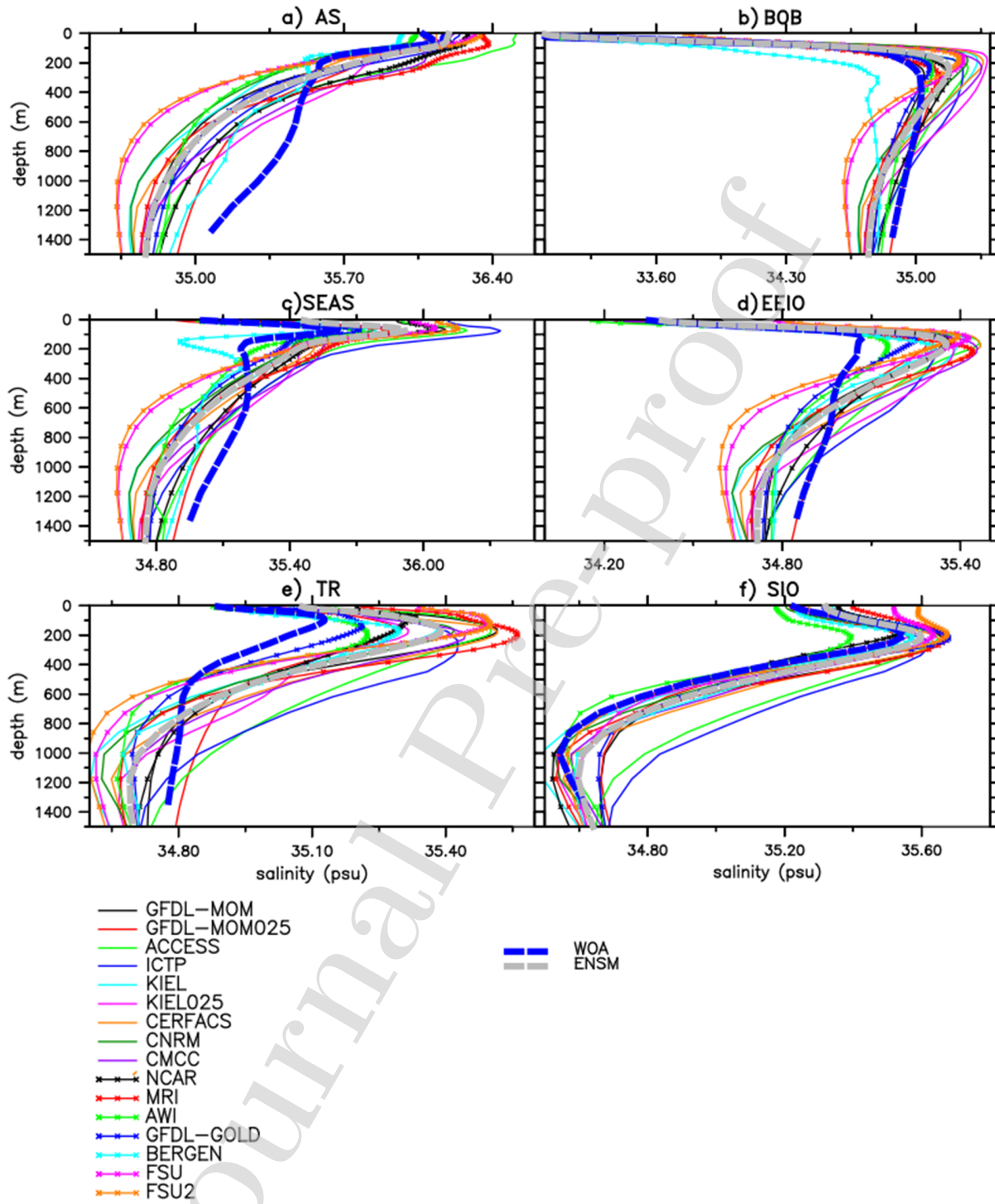


1365

1366 Figure 22c: Same as figure 22a but for the Eastern Equatorial Indian Ocean.

1367

1368 This low salinity could be due to the unrealistic exchange of salty water from the Red Sea and
 1369 Persian Gulf in these models (Legg et al., 2009; Durgadoo et al., 2017). In the BoB, the halocline
 1370 is represented by a strong gradient over the upper 100 m, which is captured by almost all models,
 1371 except for AWI, which shows a negative salinity bias. Observations also



1372

1373 Figure 23: Annual mean vertical salinity variations from the CORE-II simulations as compared
1374 to WOA observation averaged over different sub-regions in the Indian Ocean: (a) Arabian
1375 Sea(AS), (b) Bay of Bengal (BoB), (c) Eastern Equatorial Indian Ocean(EEIO), (d) Southern
1376 Indian Ocean (SIO), (e) South Eastern Arabian Sea (SEAS), and(f) Thermocline Ridge
1377 (TR).(See Section 3.4 for sub-region specifications)

1378
1379 show a local maximum in salinity around 200-400 m depth, which is connected to the intrusion
1380 of high saline ASHSW, Red Sea Water (RSW) and Persian Gulf Water (PGW) (Rochford ,1964;
1381 Varadachari et al., 1968; Sastry et al.,1985; Vipin et al.,2015). All models capture this subsurface
1382 salinity maximum except for AWI. Below 400 m FSU and FSU2 show a much fresher layer as
1383 compared to WOA observation.

1384
1385 Vertical salinity variations in the SEAS show a saltier layer at 50 m depth with a fresh
1386 layer above and below. As already seen in the AS, in the SEAS models overestimate the surface
1387 and subsurface salinity, with only AWI showing a clear local minimum between 100 m and 200
1388 m depth. Below 600 m all models are fresher than the observations. In the TR region, the
1389 presence of ASHSW increases subsurface salinity at 100-200 m depth. Although all models
1390 overestimate salinity in the upper 400 m, they capture this increased salinity signature from
1391 ASHSW and finally end with a rather constant salinity over depth below 1000 m, as seen in
1392 observations already further up in the water column.

1393
1394 In the SIO a high saline subsurface layer exists at 200-400 m depth. This salty layer is
1395 formed due to the presence of Indian Ocean Central Water. The excess evaporation over
1396 precipitation forms high salinity surface water (>35 psu) between 35°S - 25°S , winter convection
1397 and downward fluxes of salt and heat causes the subtropical water to extend with salinity above
1398 35 psu to a depth of about 500 m (Wyrcki, 1973). The subsurface salinity maximum in the south
1399 Indian Ocean spreads towards the north and is carried by the South Equatorial Current and
1400 reduces the thickness of the central water mass to 300 m at 20°S and 100 m at 10°S . The
1401 subsurface salinity maximum is at ~ 250 m depth, in which salinity can exceed 35.6 psu as

1402 reported by Warren (1981). This feature is most strongly developed in the central Indian Ocean,
1403 between 70-100 °E along 18 °S. Slight freshening at 1000 m depth is seen in the observation,
1404 which is captured by most models except CERFACS and KIEL025. This freshening is due to the
1405 intrusion of Antarctic Intermediate Water in this layer (Wyrski, 1973). This low salinity layer has
1406 a thickness of 500 m or more and can be identified by a salinity minimum of 34.3-34.4 psu at the
1407 Subtropical Convergence Zone. Warren (1981) has reported that the salinity minimum of AAIW
1408 is at depth of 600-900 m along 18 °S with depth generally increasing towards the west.

1409

1410 In summary, the vertical salinity structure is more realistically captured by z-level models
1411 (MOM and NEMO group of models) except for ACCESS and ICTP. The vertical salinity
1412 structure is less well represented by the isopycnal/hybrid models (BERGEN, FSU and FSU2).
1413 An increased horizontal resolution in the model marginally improves the salinity simulation.

1414

1415 **4.5. Variations in the Equatorial currents**

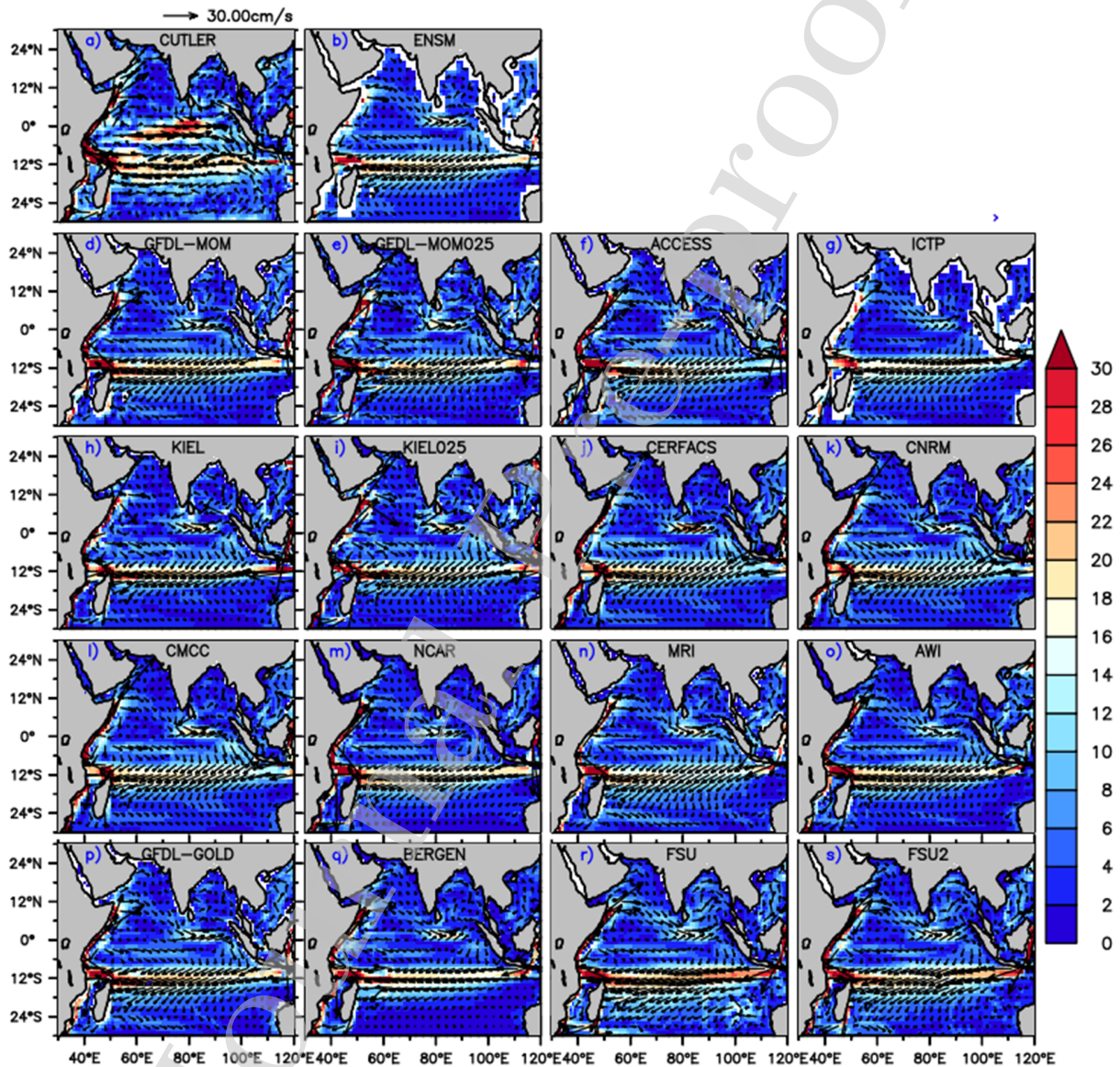
1416

1417 **4.5.1 Surface Current**

1418 As seen in Figure 24a, the CORE-II simulations capture the major current systems shown
1419 in Figure 1. During the northeast Monsoon the SC flows southward and is limited to the region
1420 south of 10 °N. The surface flow reverses in April and November, during the inter-monsoon
1421 period (not shown). Observations show that during the southwest Monsoon, the SC develops into
1422 an intense jet with extreme velocities of about 2 m/s during mid-May and reaching to 3.5 m/s
1423 during June (INDEX, 1976-1979). This jet is very well reproduced in all the models; however,
1424 models are unable to capture the observed magnitudes (not shown). The SEC, the westward
1425 current south of 10 °S, does not undergo any seasonal variation in direction throughout the year.
1426 The model simulated SEC shows good fidelity in reproducing the spatial variability seen in the
1427 observations (Figure 24a). Compared to the observations all models show a narrower SEC and
1428 an underrepresented SECC pattern.

1429

1430 Figure 24b shows the comparison of the seasonal cycle of the WJ between different
 1431 observations (OSCAR, CUTLER and LUMPKIN) and the CORE-II model simulations. All
 1432 observations show the spring (autumn) jets peak in May (November) but differ in magnitude
 1433 between 33-43 cm/s. Interestingly, all the models show a quite coherent but under-represented
 1434 autumn jets; however, there exist a large model spread (25-45 cm/s) in the representation of the
 1435 spring jet.

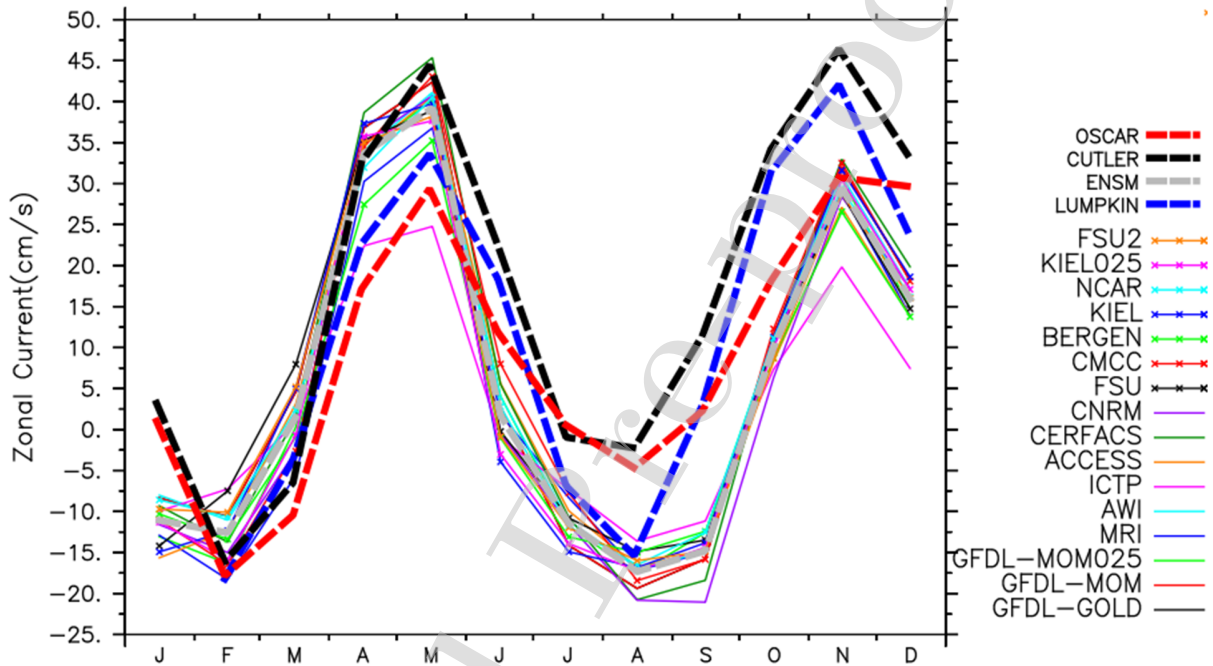


1436

1437 Figure 24a: Annual mean surface current comparison (current speed is given in color) with ship
 1438 drift observation. The upper left panel shows observations (CUTLER) and the upper middle
 1439 panel shows CORE-II ensemble mean. The remaining panels show the individual CORE-II
 1440 models. Units are in cm/s.

1441

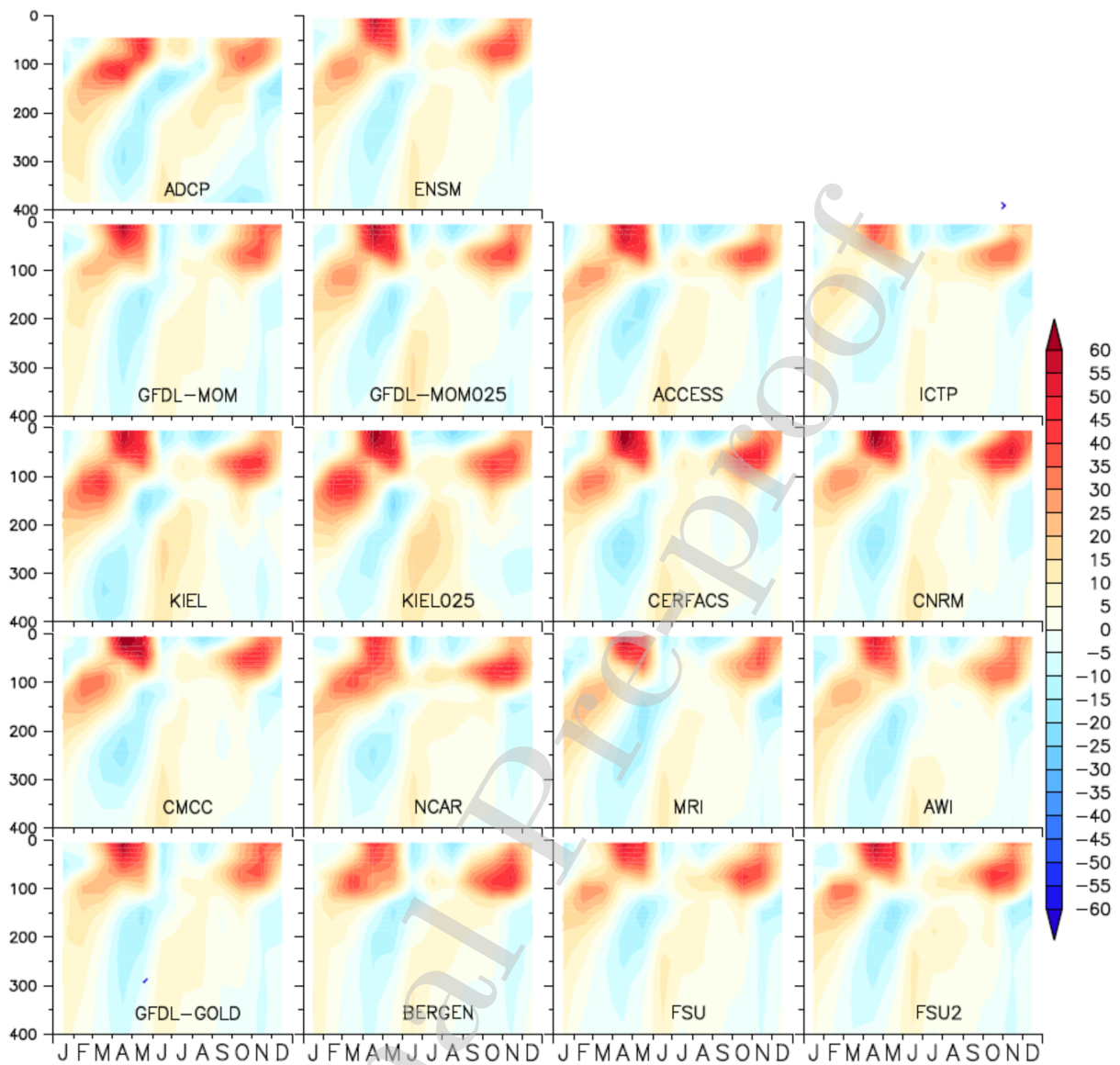
1442



1443 Figure 24b: Seasonal cycle of zonal currents at the WJ location [55-80 °E, 2.5 °S - 2.5 °N]
 1444 averaged over 0 -15m depth from CORE-II simulations and observations (CUTLER, OSCAR,
 1445 LUMPKIN).

1447

1448 **4.5.2 Subsurface Currents**



1449
1450

1451 Figure 25: Upper ocean mean zonal current (cm/s) comparison of CORE-II simulations with
1452 ADCP observation at 90 °E and equator. The mean is computed for 2001-2007 for both models
1453 and ADCP observation.

1454

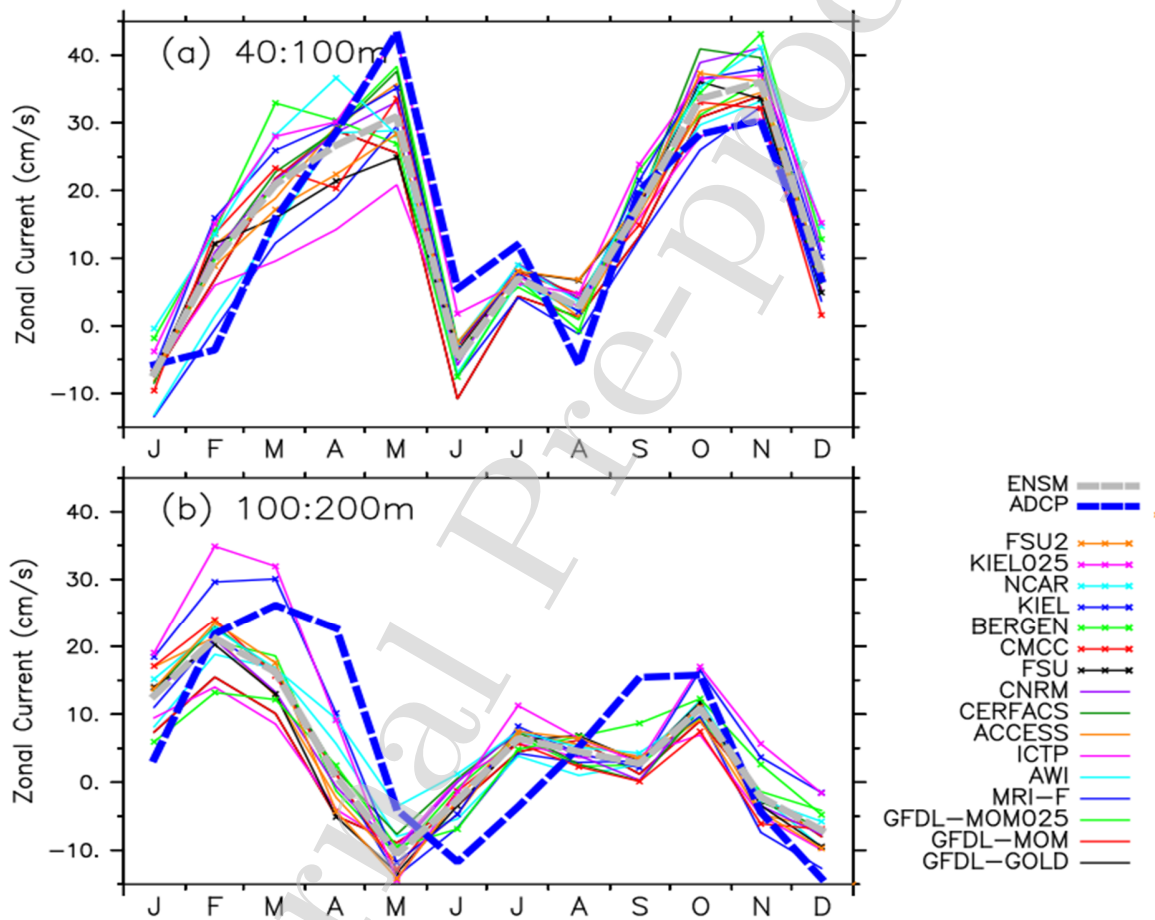
1455 Figure 25 shows the seasonal cycle of sub-surface currents from Acoustic Doppler
1456 current profiler (ADCP) observations and the CORE-II simulations at 90 °E and the equator.

1457 CORE-II simulations are able to capture the semi-annual cycle of the EUC magnitude. Refining
1458 the horizontal resolution from GFDL-MOM to GFDL-MOM025 indicates an improvement in the
1459 EUC representation. The NEMO groups of models accurately simulate the EUC magnitude.
1460 However, all models are unable to capture the timing of the peak values of EUC (Figure 26b),
1461 where the peak magnitude is reached about a month earlier (February) relative to ADCP
1462 observations. The pronounced upward phase propagation (Iskandar et al., 2009) is weaker or
1463 near absent in the CORE-II models.

1464 The presence of a WJ during inter-monsoon period extends down to 100 m (Figure 25).
1465 The ADCP observations are not available in the upper 40 m but the extent of spring WJ can be
1466 seen between 40-100 m (Figure 25). To compare the lower part of WJ, the seasonal cycle of
1467 upper ocean current averaged over 40-100 m depth from observations and simulations are shown
1468 in Figure 26a. None of the models capture the observed peak spring jet values of ~ 45 cm/s
1469 whereas the models overestimate the autumn jet values. The observed eastward current
1470 associated with summer monsoon in July is also not found in any of the models whereas the rest
1471 of the season they are more coherent and close to observations.

1472 EUC is present below WJ and it is most prominent at 90-170 m (Iskandar et al., 2009).
1473 To examine the simulated EUC seasonal cycle, we show the depth averaged (100-200 m) zonal
1474 current from ADCP observations and CORE-II simulations in Figure 26b. The peak observed
1475 EUC value occurs in March-April, but all the models show an early peak in February-March.
1476 Iskandar et al. (2009) showed that development of an eastward pressure gradient during winter is
1477 responsible for the formation of the EUC with a delay of one month. Equatorial wave dynamics
1478 also play a role in the development of EUC. A downwelling Kelvin wave is excited in the
1479 western basin in March-April (see their Figure 8b), which raises the sea level in the western part,
1480 whereas an upwelling Rossby wave lowers the eastern basin during same time. These waves are
1481 responsible for generating the pressure gradient. In the CORE-II simulations all models show the
1482 appearance of these waves about a month early and hence the pressure gradient force gives rise
1483 to an early EUC peak (not shown). The subsurface-surface interactions in the ocean are governed
1484 chiefly by baroclinic dynamics and wave propagations. If baroclinic dynamics are affected via
1485 biases in the resolved vertical structure of density, the associated planetary/Rossby and Kelvin

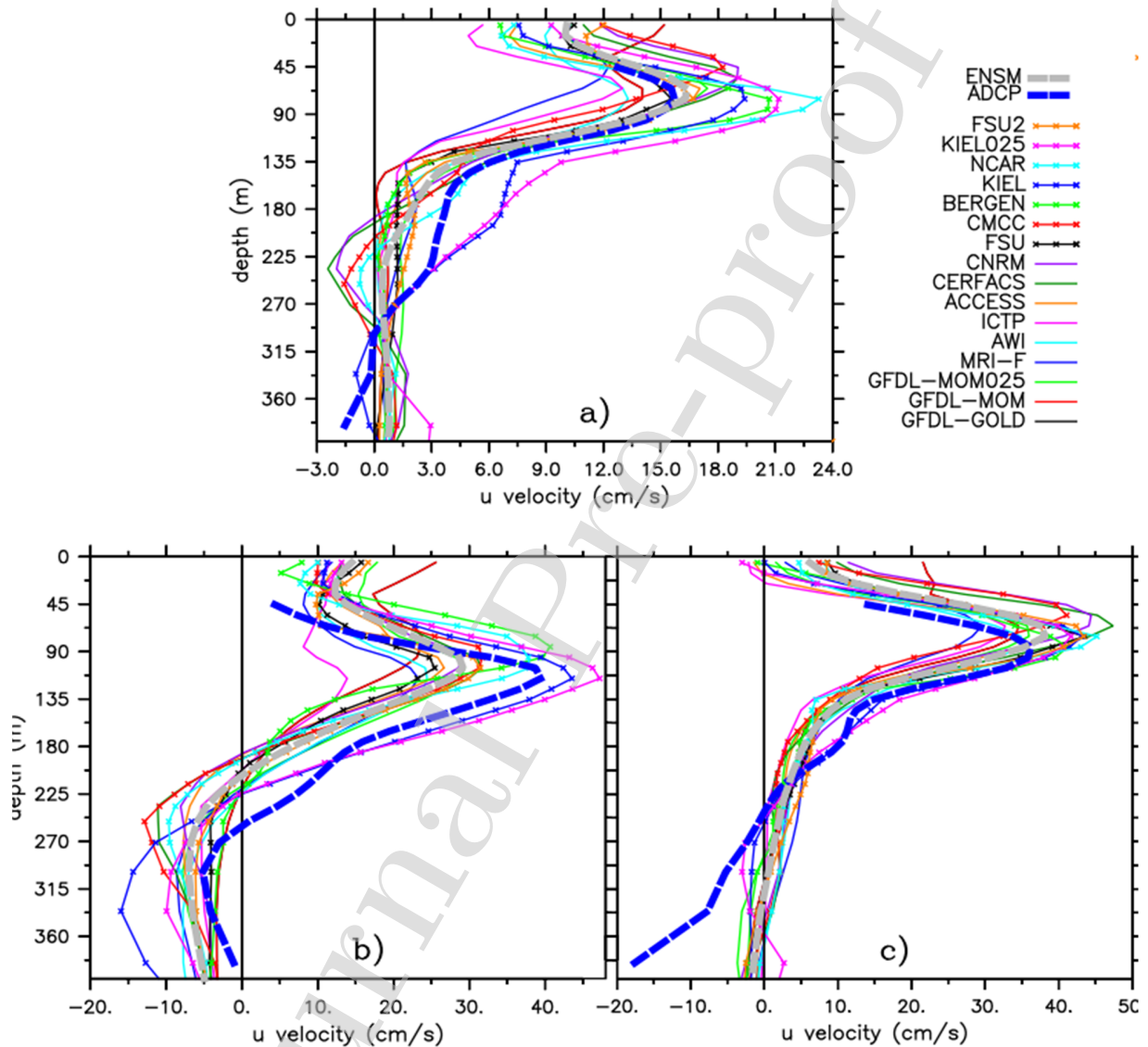
1486 waves will be affected too. These waves are the key controlling factors for thermocline
 1487 displacements and are at the core of tropical climate variability such as El Nino-Southern
 1488 Oscillation and Indian Ocean dipole/zonal mode (IODZM). Recently Shikha and Valsala (2018)
 1489 have shown the subsurface temperature and salinity bias in CMIP-5 models over the Indian
 1490 Ocean tend to have a positive bias in the speed of first baroclinic mode wave propagation since
 1491 the first and second baroclinic modes are highly sensitive to density and its biases.
 1492



1493
 1494
 1495
 1496
 1497
 1498

Figure 26: Seasonal cycle of zonal current at 90 °E and the equator from CORE-II simulations and ADCP observations (a) averaged over 40-100 m depth and (b) averaged over 100-200 m depth. Model ensemble mean is also plotted in gray.

1499 Figure 27a shows the comparison of annual mean vertical variation of the zonal current at
 1500 90 °E and at the equator. The ADCP observations show that the annual mean subsurface zonal
 1501 current peaks at 80 m depth with a magnitude of 15 cm/s. FSU2 remarkably reproduces this
 1502 feature.



1503
 1504

1505 Figure 27: The upper ocean zonal current with depth at 90 °E and the equator from CORE-II
 1506 models and ADCP observation (a) Annual mean, (b) April mean and (c) October mean. The
 1507 mean is computed for 2001-2007 for both models and ADCP observation.

1508 As explained earlier, the NEMO (MOM) class of models over- (under)estimate this
1509 observed EUC value. Due to these counter-acting biases, the ensemble mean is relatively close to
1510 ADCP observations both in magnitude and depth. The subsurface zonal current in April is shown
1511 in Figure 27b. Most of the models are unable to capture the peak values at the observed depth.
1512 Only KIEL simulations are able to capture the observed depth of the EUC, but with an
1513 overestimation of up to 10 cm/s. BERGEN and NCAR simulate the peak EUC value, but it peaks
1514 at a shallower depth of 90 m. The EUC in the coarse model from ICTP is almost absent, while all
1515 other models show a comparable velocity structure as the observations.

1516 The autumn EUC appears at a slightly shallower depth (90 m) compared to spring (~110
1517 m) (Figure 27c), with the models showing biases in the peak depth and its amplitude. During
1518 autumn, most models show stronger EUC with varying peak depths ranging between 45-90 m,
1519 whereas the observed value is ~ 35 cm/s at 90 m. The spread of peak EUC values in the autumn
1520 is much less than its spring values. But in the autumn the models are unable to capture the
1521 westward current at the depth range 300-400m seen in observations.

1522 To assess the robustness of the above results, we repeated the analysis at 80 °E. There
1523 only 3 years (2005-2007) continuous observational ADCP data is available till 340 m depth
1524 (Nagura and Masumoto 2015). We thus computed a monthly climatology for both ADCP and
1525 CORE-II simulated data over that period. At 80 °E location the ADCP and CORE-II model
1526 comparisons show coherent results with that at 90 °E. The WJ and the EUC are stronger at 80 °E
1527 compared to at 90 °E (not shown). Furthermore, the inter-model spread for both currents is
1528 reduced at 80 °E. Another notable difference at 80 °E is that the timing of the EUC peak in
1529 spring is reproduced by all models. At 90 °E all models exhibit an early peak.

1530 Recently McPhaden et al. (2015) showed that the volume transport associated with the
1531 WJ peaks in May (November) with a transport of 14.9 +/- 2.9 Sv (19.7 +/- 2.4 Sv). The coupled
1532 models analyzed by McPhaden et al. (2015) were unable to capture these observed values. We
1533 examine here the performance of the CORE-II models by computing the transport following
1534 McPhaden et al. (2015). The CORE-II models capture the observed seasonal variation of upper

1535 ocean volume transport (not shown). The ensemble mean of zonal transport shows a transport of
1536 18.74 Sv in May and 16.83 Sv in November which is similar to Wyrтки jet volume transport
1537 reported by McPhaden et al. (2015).

1538

1539 **4.6. Indian Ocean meridional overturning circulation**

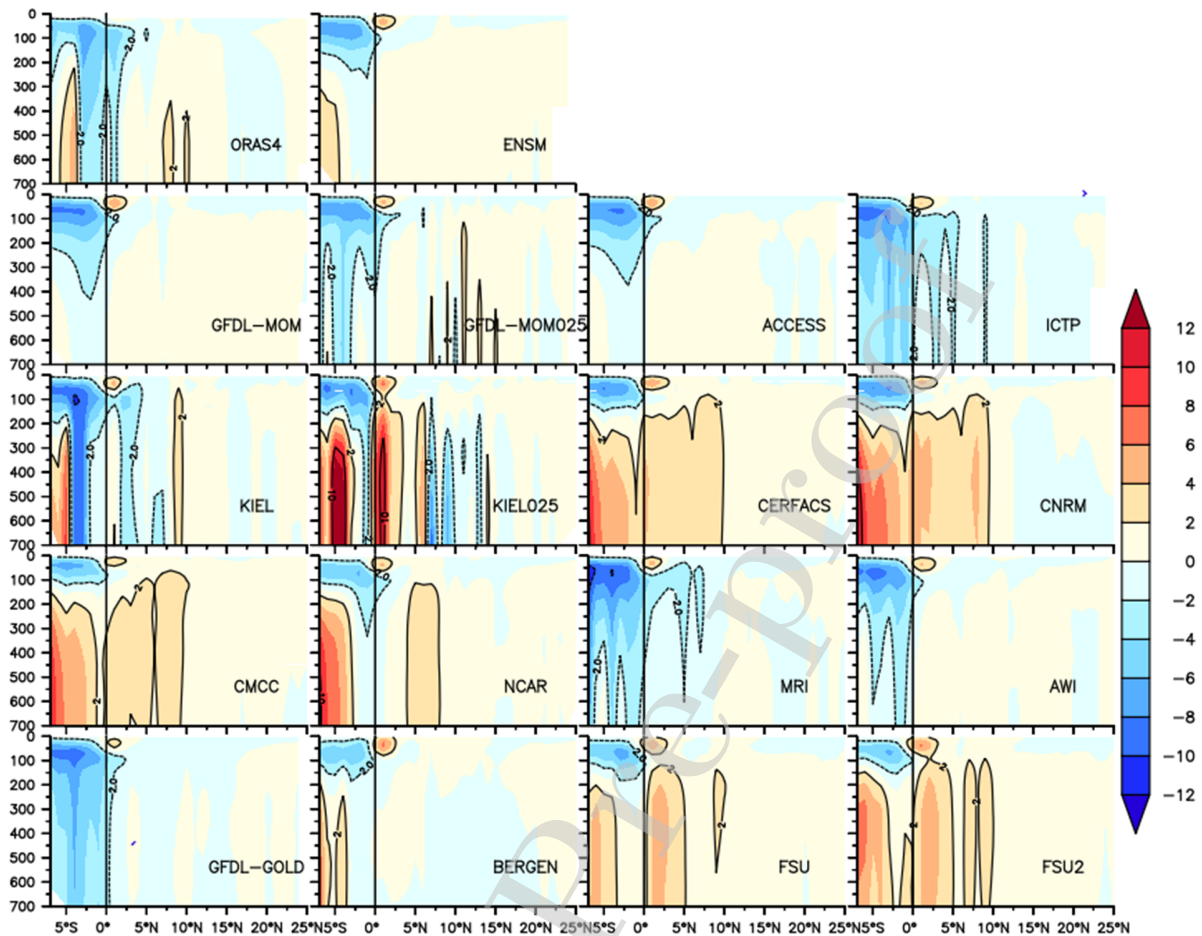
1540 The surface circulation of the northern and the equatorial Indian Ocean shows large seasonal
1541 changes due to seasonal reversals of the monsoon winds. The seasonal variability of surface
1542 circulation is well known, such as the Somali Current (Schott et al., 1990) and the semiannual
1543 equatorial jet (Wyrтки, 1973). However, characteristics of CEC and its underlying mechanisms
1544 are not very well known (Lee, 2004). Apart from CEC, the presence of an “equatorial roll” in
1545 the mixed layer of the Indian Ocean was also identified in model simulations of Wagcongne and
1546 Pacanowski (1996), and its presence has been confirmed thereafter by observations (Wang and
1547 McPhaden 2017; Horii et al. 2013; Perez-Hernandez et al. 2012; Schott et al., 2002). This
1548 shallow equatorial roll consists of a northward wind-driven surface current in the upper 25 m
1549 near the equator overlaying the southward directed subsurface Sverdrup transport. This
1550 circulation is narrowly confined to within $\pm 1^\circ$ of the equator and is most strongly developed
1551 seasonally during July-October. However, it has little impact on cross-equatorial heat transport
1552 (e.g., Schott et al., 2002; Miyama et al., 2003).

1553 In the north Indian Ocean (north of 10°S) the annual mean net surface heat flux is
1554 directed into the ocean (Oberhuber, 1988; Godfrey et al., 2007). It is the wind-driven meridional
1555 overturning circulation in the upper several hundred meters that exports the annual-mean net heat
1556 gain towards the subtropical SIO, south of the Equator (Wagcongne and Pacanowski, 1996; Lee
1557 and Marotzke, 1997,1998; Gartnericht and Schott, 1997; Miyama et al., 2003). Godfrey et al.
1558 (2007), evaluating a variety of different models over the Indian Ocean, found a mean heat
1559 transport more than double the mean obtained when averaging the observed climatology. The
1560 CEC is very important for the NIO warming and sea level variability (Srinivasu et al., 2017;
1561 Swapna et al., 2017).

1562

1563 Figure 28 shows the Indian Ocean Meridional Overturning circulation (IOMOC)
1564 computed from all the models and the ORAS4 reanalysis. Most of the models are able to
1565 simulate the CEC, while there is almost no thermocline northward flow in the coarse model from
1566 ICTP. The mean strength of CEC varies in different models and is in the range of 2-8 Sv. This
1567 value is within the earlier reported value of 6 Sv (Lee and Marotzke, 1997; Schott et al., 2002a,
1568 b). The CEC structures as demonstrated by Miyama et al. (2003) are well reproduced by a
1569 majority of the models (Figure 28). The ensemble mean from the entire model suite is shown in
1570 upper middle panel of Figure 28. The CEC structure is prominent and it corroborates the finding
1571 of Miyama et al. (2003).

1572 Although Miyama et al. (2003) have shown the pathways of CEC, the vertical extent and
1573 the exact location of equatorial crossing have not been reported in earlier studies. To quantify the
1574 vertical extent and exact location, we plot the cross equatorial transport across the equator. The
1575 cross equatorial transports from all the individual models show the vertical extent of



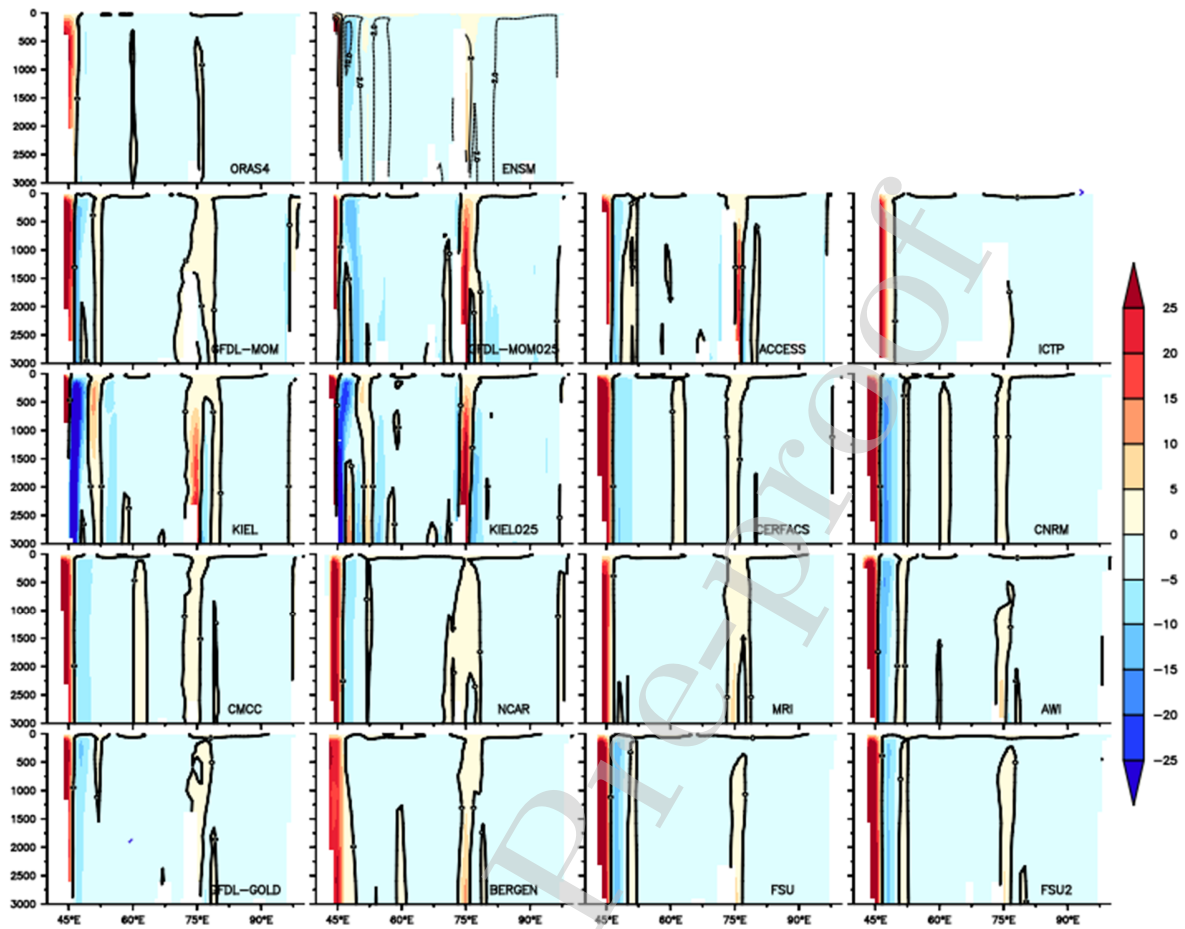
1576

1577 Figure 28: Indian Ocean meridional volume transport (IOMOC) from CORE-II simulations and
 1578 ORAS4 analysis. Units are in Sv.

1579 the northward cross equatorial flow extends over the full water column near the African Coast
 1580 (Figure 29). The magnitude of this flow varies and is strongest in CERFACS, CNRM, AWI,
 1581 FSU and FSU2. The ensemble mean cross equatorial transport with depth is shown in the upper
 1582 middle panel of Figure 29. A narrow band of CEC near the Somali coast can be seen from Figure
 1583 29, with vertical extent of the transport extends to 1500 m. All the models show another
 1584 secondary pathway of northward transport of cross equatorial flow along 75 °E with a value
 1585 ranging 5-10 m^2/s . These values are more prominent and higher in the fine resolution MOM and
 1586 KIEL simulations with a maximum value of $\sim 20-25 m^2/s$. With islands and seamounts along 75

1587 °E (the Maldives and Chagos Archipelago), topography plays a major role for the northward
1588 transport along that longitude. Nagura and Masumoto (2015) used in-situ observations and
1589 OGCM output to find a northward current at about 75 °E. They discussed its dynamics using 1.5-
1590 layer model experiments and found that the WJ hits the Maldives Islands near 73°E and
1591 meanders, leading to a northward current near the islands. The KIEL1 and MOM1 topography do
1592 not show the presence of Maldives Island along the 73 °E in the upper 1000 m. However, the
1593 MOM025 and KIEL025 models show the presence of bathymetry at 45 m depth onwards (not
1594 shown). The annual mean currents in the models at 200 m and below are mostly zonal along the
1595 equator. As reported by Nagura and Masumoto (2015) the presence of Maldives Island around
1596 73°E meanders this zonal current and leads to northward current at the southern flank of the
1597 Island, which mainly drives the northward transport seen in Figure 29 for the ¼ degree MOM
1598 and KIEL simulations.

1599 The strong southward flow apparent in the KIEL models near to the Somali coast is due
1600 to the stronger meridional currents seen in these models. This strong southward current is absent
1601 in other models (not shown). The transport along the African coast across 5 °S is stronger than
1602 across the Equator (not shown). This band is also a slightly wider across 10 °S. Observations
1603 show a strong northward transport (25-30 m²/s) along 50 °E



1604

1605 Figure 29: Transport across the equator from all the models. The upper left panel shows transport
 1606 from ORAS4 reanalysis product. The upper middle panel shows transport from CORE-II
 1607 ensemble. The remaining panels show transport from all CORE-II individual models. The
 1608 maximum transport occurs through a narrow passage near to Somali Coast. Note that the $\frac{1}{4}$
 1609 degree simulations from MOM-25 and KIEL025 show large transport at $\sim 75^\circ\text{E}$. Units are in
 1610 m^2/s .

1611 across the 10°S latitude (not shown). Only GFDL-MOM and ICTP are able to capture this band.

1612

1613 We conclude that most CORE-II models simulate the structure of the CEC in the Indian
 1614 Ocean. Additionally, the CORE-II analysis uncovers a previously unidentified secondary

1615 pathway of CEC. Namely, there is a northward cross-equatorial transport along 75 °E, which is
1616 also present feebly in ORAS4, complements the pathway near the Somali coast.

1617

1618 **5. Summary of impacts from model resolution**

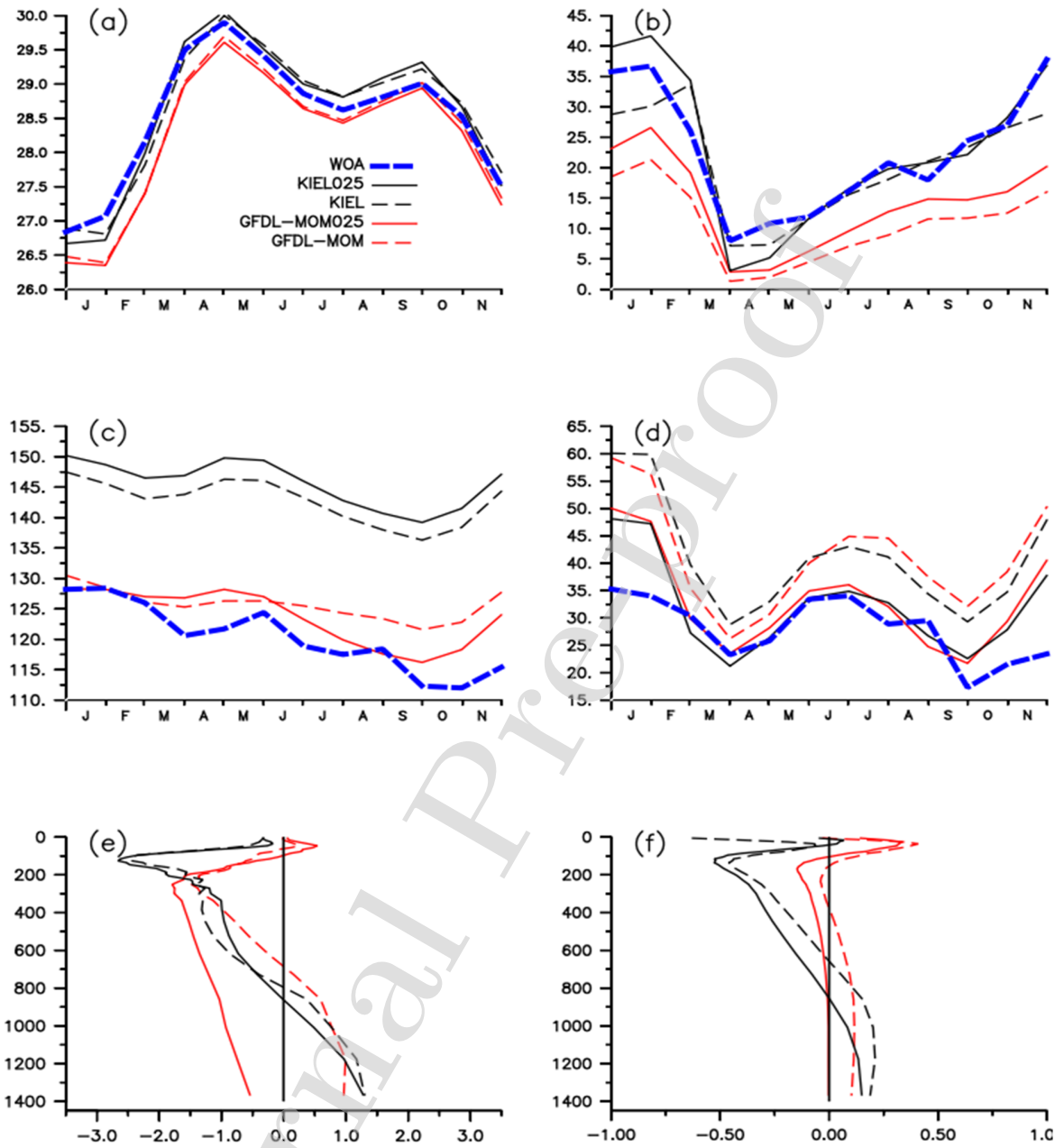
1619 Momin et al. (2014) is the only study that reported on the impact of model resolution for
1620 Indian Ocean simulations. They showed an overall marginal improvement in D20, SST and SSS,
1621 though with a degradation in SST seasonal cycle over the equatorial Indian Ocean. In earlier
1622 sections, we identified a variety of features that differ across the ICTP, GFDL-MOM/GFDL-
1623 MOM025 and KIEL/KIEL025 resolution suite. In this section, we discuss these two resolution
1624 suites with a focus on the Bay of Bengal.

1625 Figure 30a shows the comparison of SST simulation derived from KIEL and MOM. Both
1626 coarse and fine resolution models capture the observed seasonal cycle. Increased resolution does
1627 not improve the biases in spring (MOM) and summer for neither KIEL nor MOM. The KIEL and
1628 KIEL025 simulations reproduce the observed SST variation during winter and spring, associated
1629 with a good representation of the BL thickness (Figure 30b).

1630 The observed thermocline seasonal cycle is well captured in MOM with some
1631 improvement in MOM025. However, the KIEL and KIEL025 simulations show a systematic bias
1632 of ~20 m in 20 °C isotherm (D20) throughout the season with slight improvement in KIEL025
1633 (Figure 30c), possibly as a result of differences in parameterizations between KIEL and MOM.
1634 Enhanced horizontal resolution shows a significant improvement in the MLD simulations both in
1635 MOM025 and KIEL025 as compared to their coarse resolution counterparts (Figure 30d). The
1636 mixed layer depth in MOM025 and KIEL025 show similar value to WOA during spring and
1637 summer, but deeper by ~ 10 m during autumn and winter. Their coarse resolution counterparts
1638 show ~20 m deeper MLD as compared to WOA observations. The vertical temperature
1639 difference with respect to WOA observations is shown in Figure 30e. KIEL does not show any
1640 significant improvement in vertical temperature simulations as resolution increases, but MOM
1641 shows a slight warming in the deeper layer when refining the resolution, which can also be seen

1642 in the seasonal bias plot in Figure 20b. For salinity, MOM shows improved simulations below
1643 the thermocline as resolution increases, but in KIEL bias slightly increases with increase in
1644 resolution (Figure 30f).

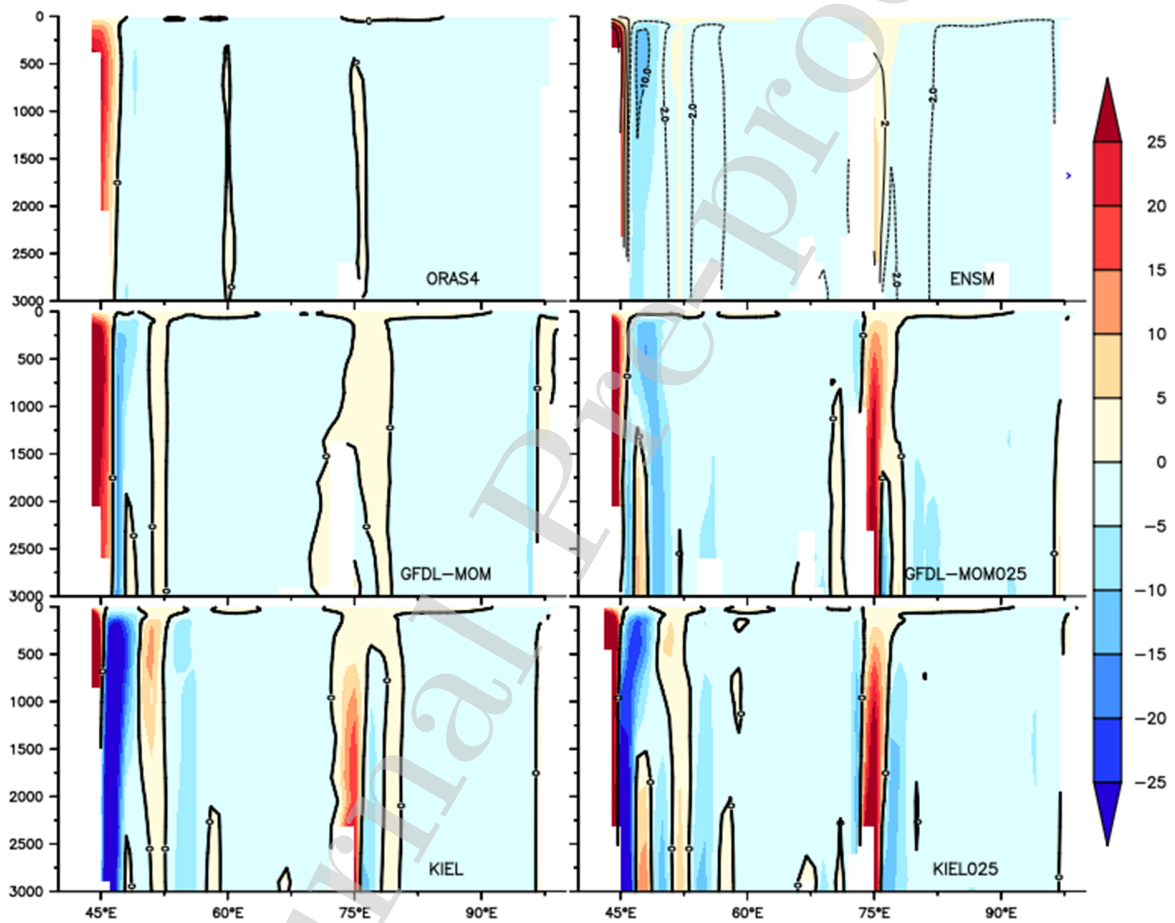
1645 Figure 31 shows the annual mean cross equatorial transport with depth along the equator
1646 for MOM, MOM025, KIEL, KIEL025, ensemble mean of all models and ORAS4. As explained
1647 in the previous section the coarse resolution models do not show much transport across 72-76 °E,
1648 but with enhanced resolution this transport is very prominent with magnitude of 25-30 m²/s.
1649 Earlier modeling studies show that the cross equatorial volume transport is maximum near the
1650 Somali coast in a narrow band between 43-46 °E (Jensen, 2003, 2007; Miyama et al., 2003). The
1651 coarse resolution MOM and KIEL simulations also show the similar band in the surface layer,
1652 with the high resolution (MOM025 and



1653

1654 Figure 30: Seasonal cycle of (a) SST, (b) Barrier Layer Thickness, (c) Thermocline Depth, (d)
 1655 mixed layer depth for 1 degree and $\frac{1}{4}$ degree MOM and 0.5 degree and $\frac{1}{4}$ degree KIEL models.
 1656 Vertical temperature (e) and salinity (f) bias (model minus observation) with respect to WOA
 1657 observations. The averages are taken over the Bay of Bengal.

1658 KIEL025) showing even narrower band of cross equatorial flow near the Somalia coast (Figure
 1659 31) with much stronger value ($\sim 50 \text{ m}^2/\text{s}$) and a strong secondary pathway along $72-76^\circ\text{E}$. As
 1660 previously reported at around 50°E a weak cross equatorial transport can be found in the
 1661 simulations except for the MOM025 configuration. The cross equatorial transport near Somalia
 1662 coast is mainly contributed from July (Figure 32b), whereas there is a negligible cross equatorial
 1663 volume transport during January (figure 32a) over the Somali coast.

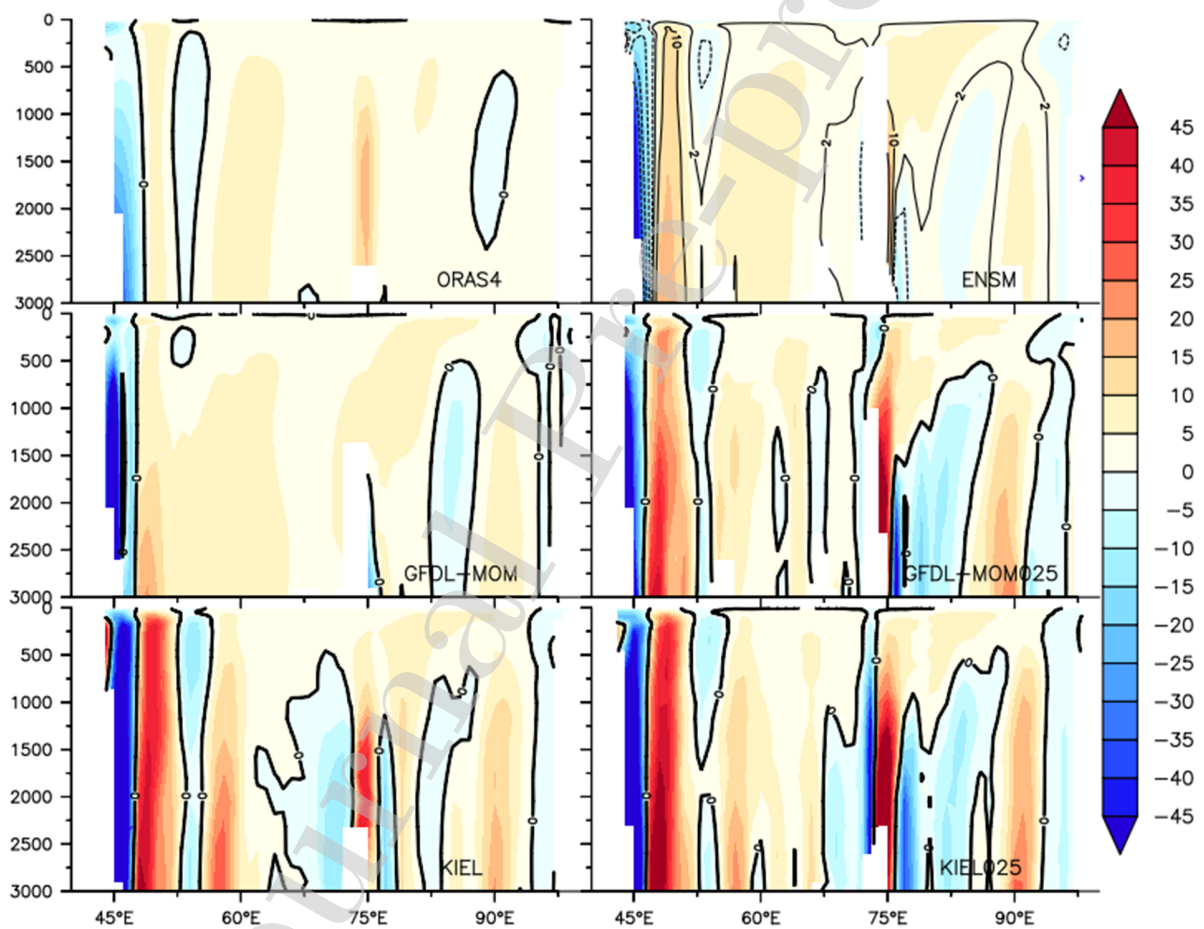


1664

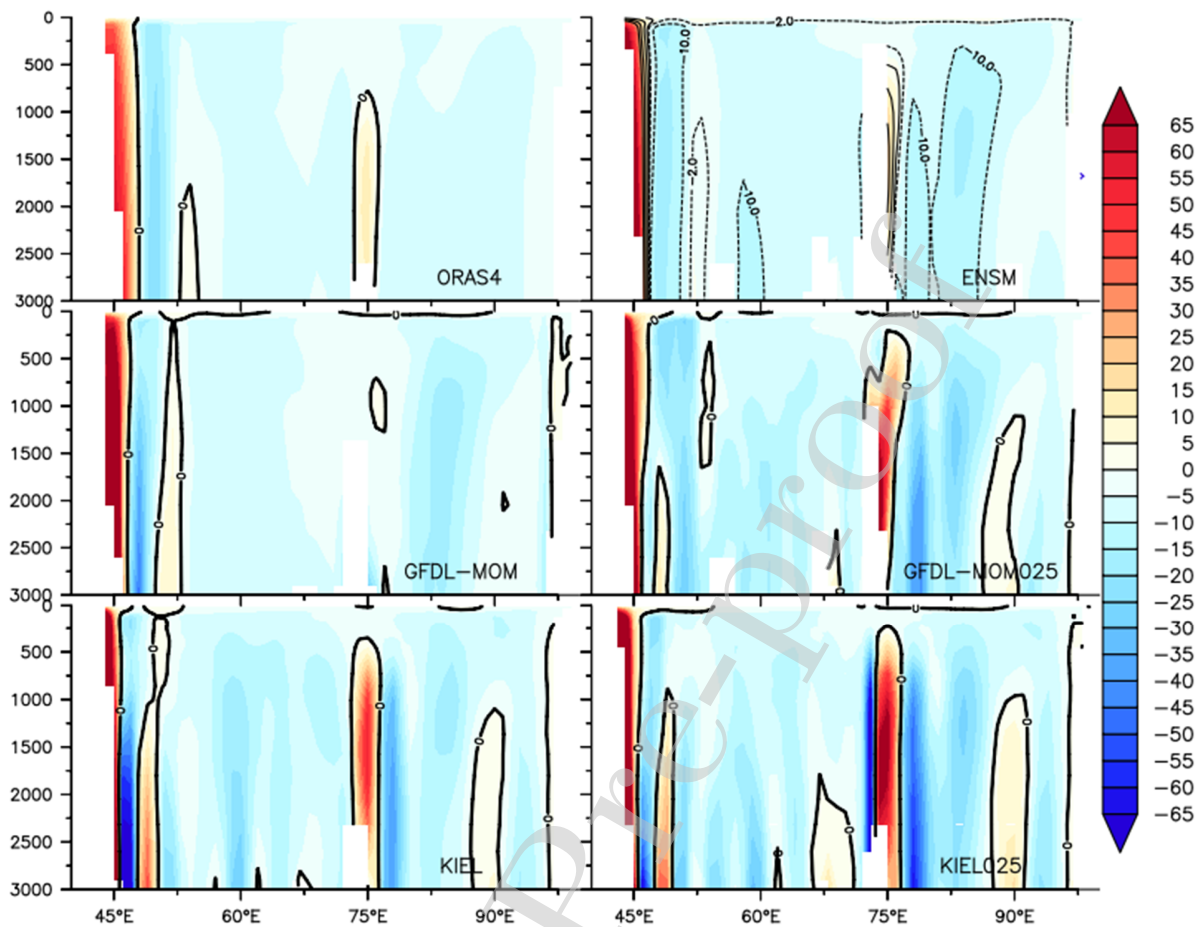
1665 Figure 31: Annual mean transport across the equator from MOM, MOM025, KIEL, KIEL025,
 1666 all model ensemble and ORAS4. Units are in m^2/s .

1667 There is stronger cross equatorial transport in the subsurface with enhanced resolution in
 1668 KIEL025 as well as MOM025. The secondary cross equatorial pathways of volume transport
 1669 along 72-74 °E in the subsurface appears in the high resolution models both during winter and
 1670 summer (Figure 32a,b). This feature is absent or near absent in the coarse resolution models in
 1671 the ensemble mean and ORAS4 reanalysis products as well.

1672 We conclude that increasing the horizontal resolution does not necessarily improve the
 1673 temperature and salinity properties noticeably. However, increased resolution does improve
 1674 fidelity in the cross-equatorial pathways in the Indian Ocean.



1675
 1676 Figure 32a: Transport across the equator from MOM, MOM025, KIEL, KIEL025, all model
 1677 ensemble and ORAS4 in January. Units are in m^2/s .



1678

1679 Figure 32b: Transport across the equator from MOM, MOM025, KIEL, KIEL025, all model
 1680 ensemble and ORAS4 in July. Units are in m^2/s .

1681

1682 6. Summary of the assessment

1683

1684 We presented an analysis of 16 ocean/sea-ice models forced according to the Coordinated
 1685 Ocean-ice Reference Experiments (CORE) interannual protocol, focusing here on the annual
 1686 mean and seasonal features of the Indian Ocean. This assessment is the first of its kind, and thus
 1687 it offers an important benchmark for further studies with global ocean/sea-ice models or fully
 1688 coupled climate models. In particular, we documented the mean state by analyzing surface

1689 properties (SST, SSS and surface currents), subsurface properties (temperature, salinity and
1690 currents), and the MOC. The SST from CMIP5 simulations were also utilized to compare the
1691 coupled and CORE-II simulations.

1692
1693 Our study provides an assessment across a suite of high-end global ocean climate models,
1694 many of which were part of CMIP5 climate models. We identified many biases with the
1695 simulations, and offered suggestions for where these biases might be related to limitations in the
1696 CORE-II forcing or the ocean model physical parameterizations. As in other CORE-II
1697 assessments, we do not perform sensitivity studies to support hypotheses for what mechanisms
1698 lead to the diagnosed model biases. Nevertheless, our study provides a critical baseline from
1699 which future targeted studies can address these limitations. This perspective forms the basis for
1700 the nine other published CORE-II assessments.

1701
1702 In the following we offer a summary of the main results from our assessment.

1703

1704 **6.1 Sea Surface Temperature**

1705 CORE-II models show improvement in capturing the observed seasonal variability with
1706 less bias compared to the coupled models, and their SST biases are ~ 2 times smaller than
1707 coupled simulations. The SST simulations from coupled CMIP5 models that we analyzed are
1708 dominated by a negative (cold) bias in the Indian Ocean of about 1-2 °C, with large inter-model
1709 spread particularly over the EEIO. Additionally, CMIP5 models are generally unable to simulate
1710 the timing and magnitude of peak SST values, thus affecting the seasonal cycle over the AS, the
1711 BoB and the EEIO. This result emphasizes the need to improve the atmosphere and ocean
1712 components of coupled climate models and their coupling to improve their representation of
1713 regional Indian Ocean features.

1714 We comment in particular on the northern AS, where the CORE-II simulations show a
1715 negative (cold) SST bias (1-2 °C) during February to April, which is increased to (2-3 °C) in the
1716 CMIP5 models. Previous studies showed that the advection of cold air from the Asian land mass
1717 causes this large cooling in coupled models (Marathayil et al., 2013; Sandeep and Ajayamohan,

1718 2014). We also find that this large bias arises from a deeper MLD over this region in the CORE-
1719 II simulations.

1720

1721 **6.2 Sea Surface Salinity (SSS) and barrier layer**

1722 The CORE-II models show a positive salinity bias in the BoB, the AS and the SEAS. The
1723 simulations from FSU and FSU2 consistently overestimate the SSS throughout the basin,
1724 particularly over the BoB, the EEIO and the SIO, with these two models exhibiting the largest
1725 bias among the CORE-II models. The seasonal cycle of SSS shows that inter-model spread is
1726 larger in the AS and the SIO. The unrealistic seasonal cycle in CORE-II models in the AS might
1727 be due to the unrealistic representation of the overflow of high salinity waters from the Red Sea
1728 and Persian Gulf into the AS. The intrusion of high-salinity water from the AS to the BoB during
1729 the summer monsoon (Murty et al., 1992; Vinayachandran et al., 1999) is not realistic in most of
1730 the models, particularly in FSU and FSU2. Peak river runoff and the integrated summer rainfall
1731 lead to a SSS minimum in October over the BoB. Only AWI captures the seasonal cycle with
1732 low salinity in October reflecting those found in observations. Whereas SST simulations do not
1733 notably improve with enhanced resolution, the SSS simulation improves significantly when
1734 moving to the eddy permitting models KIEL025 and GFDL-MOM025 compared to their
1735 respective coarser counterparts.

1736

1737 The seasonal variation in the BL becomes most prominent during December-January
1738 when it reaches to 40 m thickness and is mainly driven by substantial river runoff into the
1739 northern BoB. None of the models capture this thick BL over the northern BoB. The NEMO
1740 models (KIEL, CERFACS, CNRM and CMCC) reasonably capture the BL and the east-west
1741 gradients. The MOM based models and the hybrid-coordinate models are unable to represent the
1742 observed BL variation. We conjecture that the inability of MOM class of models to simulate the
1743 BL, in contrast to the NEMO models, might be due to the use of distinct vertical turbulence
1744 mixing schemes.

1745

1746 **6.3 Indian Ocean circulation features**

1747 The CORE-II models are able to simulate the Indian Ocean circulation features with
1748 reasonable accuracy. The WJs are weakest in the ICTP simulations (coarsest resolution model in
1749 the suite) and are more faithfully represented in the other MOM and NEMO class of models. All
1750 the models capture the observed seasonal cycle of WJs except ICTP, which underestimates both
1751 the spring and autumn jets. Interestingly, all the models show converging values in the autumn
1752 jets, however there is a larger spread among the models for the spring jet.

1753 Three different observations (OSCAR, CUTLER and LUMPKIN) show the spring
1754 (autumn) jets peak in May (November) but they differ in magnitude. The SMC is almost absent
1755 in some models and the NMC is weaker in ICTP (again we hypothesize that this weakness is due
1756 to the coarse resolution of 2° used in the ICTP model). AWI, BERGEN, NCAR and FSU2 also
1757 show a near absence of observed peak values of SMC. We found a splitting of the zonal currents
1758 at $\sim 10^\circ\text{N}$ off the Somali coast in the AS during peak summer monsoon in the observation which
1759 is absent in all simulations. This splitting has not been noted in previous studies and is worthy of
1760 further investigation in the future using model and observational data.

1761 All models underestimate the spring WJ peak values of ~ 45 cm/s found in ADCP
1762 observations, whereas all models overestimate the autumn jet values. The observed eastward
1763 current associated with the summer monsoon in July is also poorly simulated by the CORE-II
1764 models. The NEMO group of models most accurately simulates the EUC magnitude. However,
1765 all models show an inaccurate timing of the peak values of the EUC, with models showing their
1766 peak magnitudes about a month earlier (February) than the ADCP observations (March).

1767

1768 **6.4 Subsurface temperature and salinity**

1769 All models show a basin wide warm bias at 100 m depth (typically the mean thermocline
1770 depth) except GFDL-GOLD, which shows a slightly cold bias over the EEIO and eastern AS.
1771 ICTP and BERGEN shows the largest bias ($>3^\circ\text{C}$) over the western equatorial Indian Ocean.

1772 Many models (ICTP, MRI, and BERGEN) show a warmer subsurface layer over central AS.
1773 CMCC and GFDL-GOLD well reproduce the observed spatial distribution of subsurface
1774 temperatures. The MOM group of models (GFDL-MOM, GFDL-MOM025, ICTP and ACCESS)
1775 is unable to reproduce the spatial extent and magnitude of the TR region. These models show a
1776 higher temperature at 100 m depth as compared to WOA. Although KIEL, KIEL025 and GFDL-
1777 GOLD capture the TR cooler water, they show a cold bias in the EEIO. The observed spatial
1778 distributions are most accurately reproduced by CMCC whereas the BERGEN and ICTP
1779 simulations perform the worst.

1780 The seasonal evolution of subsurface temperature shows distinct differences. All the
1781 models show a positive (warm) thermocline bias over the AS, BoB and EEIO with a magnitude
1782 ranging from ~1-4 °C. MRI and ICTP show the warmest thermocline bias (3-4 °C) among all the
1783 models in all the regions, whereas GFDL-GOLD shows a slightly cold thermocline bias. The
1784 NEMO group of models shows a reduced bias (~0.5-1 °C) in the AS. AWI, FSU and FSU2 also
1785 show a similar low thermocline bias over the AS. Over the EEIO, isotherms below 100 m show a
1786 clear semiannual signal reaching to 500 m depth. The thermocline bias shows seasonality in all
1787 the models. Over the AS and the EEIO there are maximum biases during winter and spring, but
1788 over the BoB the models show maximum biases during the summer time. Increased spatial
1789 resolution in the model increases the thermocline bias over AS and BoB, possibly as a result of
1790 increases in spurious mixing (Griffies et al., 2000, Ilicak et al., 2012).

1791 The MOM (GFDL-MOM, GFDL-MOM025, ACCESS and ICTP) and NEMO (KIEL,
1792 KIEL025, CERFACS, CNRM and CMCC) group of models show stronger upper ocean salinity
1793 stratification near the north BoB as compared to WOA, but over the south BoB they show
1794 weaker salinity stratification. AWI, BERGEN, FSU and FSU2 are unable to capture either north
1795 or south BoB salinity stratification.

1796

1797 **6.5 Meridional overturning circulation and cross equatorial transport**

1798 The MOC in the Indian Ocean consists of a CEC and a Subtropical Cell (STC) also called
1799 southern cell (see Figure 1b). The CEC is a shallow (~500 m) meridional overturning circulation
1800 consisting of the northward flow of southern-hemisphere thermocline water, upwelling in the
1801 northern hemisphere, and a return flow of surface water (Miyama et al., 2003). Most of the
1802 CORE-II models simulate the structure of the CEC. The mean strength of the simulated CEC is
1803 in the range of 2-8 Sv, which is within the earlier reported value of 6 Sv (Lee and Marotzke,
1804 1997; Schott et al., 2002a, b). The CEC structures reported by Miyama et al. (2003) are well
1805 reproduced by a majority of the CORE-II models.

1806 Maximum transport occurs through a narrow passage near the Somali Coast as reported
1807 by Miyama et al. (2003). All simulations show a single narrow band of cross equatorial flow near
1808 the Somali Coast, but its vertical structure is yet unknown (see Figure 3 and 4 of Miyama et al.
1809 2003). This study shows that the vertical extent of the transport extends to 1500 m.

1810 All models show a secondary pathway of northward transport of cross equatorial flow
1811 along 75 °E with a value ranging between 5-10 m²/s. These values are more prominent and
1812 higher in the high resolution MOM025 and KIEL025 models with a maximum value of ~ 20-25
1813 m²/s. The observations show a strong northward transport (25-30 m²/s) along 50 °E across the
1814 10 °S latitude.

1815 Thus, most CORE-II models simulate the structure of the CEC in the Indian Ocean.
1816 Importantly, the CORE-II analysis uncovers a previously unidentified secondary pathway of
1817 CEC, northward cross-equatorial transport along 80 °E, thus complementing the pathway near
1818 the Somali coast. We plan to study this secondary pathway in studies targeted on the dynamics of
1819 this flow.

1820

1821 **6.6 Comments on model resolution**

1822 ICTP is the coarsest model considered in this study, which has a nominal 2 degree
1823 horizontal grid spacing with 30 vertical levels. For many of the metrics assessed in this study,
1824 this coarse model performed the worse. We therefore suggest that Indian Ocean simulations

1825 should be conducted with grid spacing no coarser than the 1 degree used by the bulk of the
1826 models considered here.

1827 When comparing the one degree and one-quarter degree simulations, we find that moving
1828 to a fine horizontal resolution plays a large role in improving mesoscale eddy dominated
1829 processes and strong confined boundary current regions. In particular, for the eddy active BoB
1830 region the simulations are better represented using $\frac{1}{4}$ degree models (MOM025 and KIEL025)
1831 than their coarser resolution (1° MOM or 0.5° KIEL) counterparts. Furthermore, an improvement
1832 is seen in the representation of mixed layer depth, and SSS with simulations of $\frac{1}{4}^\circ$ as compared
1833 to their coarse resolution counterpart. However, the thermocline becomes deeper as well as the
1834 vertical temperature and salinity representation degrades in $\frac{1}{4}^\circ$ models compared to their coarser
1835 resolution counterparts. This is reflected in the SST features which are not improved, thus
1836 suggesting that many biases result from limitations due to physical parameterization (e.g.,
1837 vertical mixing in the boundary layers) rather than limitations due to horizontal grid resolution.

1838 Our current understanding of the meridional overturning circulation in the Indian Ocean
1839 is based largely on non-eddy-resolving models. The CORE-II simulations provide new insight on
1840 the cross-equatorial cell, which is an important component of MOC in the Indian Ocean. A
1841 future analysis will target how these new pathways improve the inter-annual variability of the
1842 Indian Ocean.

1843 **6.7 Closing comments about the present study and its future implications**

1844 The Indian subcontinent and surrounding south Asian region are home to billions of
1845 people whose livelihood depends on the ISMR. Hence, a timely and accurate prediction of the
1846 monsoon rains is crucial throughout this region. Presently, many global prediction centers predict
1847 ISMR on a seasonal time scale. The seasonal prediction skill for tropical SST anomalies provides
1848 the major predictability source of monsoon precipitation, and is closely linked to the models'
1849 ability to accurately simulate the mean SST (Sperber and Palmer, 1996; Lee et al., 2010; Pokhrel
1850 et al., 2012a; Pokhrel et al., 2016; Saha et al., 2019). Current coupled models generally show
1851 cold biases over the Indian Ocean. Our study of CORE-II simulations shows that these biases are

1852 reduced in CORE-II forced simulations, thus suggesting that the origin for the coupled biases is
1853 mostly related to coupled feedbacks that amplify ocean and atmospheric biases. However, apart
1854 from this coupled feedback the coupled mode SST bias also arises due to the tuning effect to
1855 make coupled model's global mean temperature comparable to observations.

1856
1857 The present study also shows that despite using the same atmospheric state and
1858 experimental protocol, the oceanic response from different models can be quite different as
1859 revealed by the sizable intermodal spread in many of the prognostic variables. Enhanced model
1860 horizontal resolution (to $\frac{1}{4}^\circ$) fails to improve the mean state and the seasonal evolutions. This
1861 result emphasizes the need to improve the model physics as well as providing a realistic
1862 representation of bathymetry. The phase and strength of the IOD play an important role in
1863 modulating regional as well as global climate (Saji et al., 1999; Webster et al., 1999), with the
1864 seasonal evolution of the IOD sensitive to the representation of the model mean state. A recent
1865 study also shows a model's ability to capture the teleconnection to the positive IOD is closely
1866 related to its representation of the mean state (Hirons and Turner 2018). Hence this study will
1867 give significant insight into the IOD climate mode and its prediction.

1868
1869 Recent studies by Li et al. (2016, 2017) noted that CMIP climate model projections of
1870 increased frequency of IOD events (Cai et al., 2014), increased ISMR, or a change in the mean
1871 state of the oceans are mostly artifacts of model errors that can significantly distort regional
1872 climate projections. Shikha and Valsala (2018) showed that over the Indian Ocean, CMIP5
1873 models develop internal warm and saline biases approximately between a depth range of 100 m
1874 and 800 m in long term simulations, and these internal biases have implications in large scale
1875 ocean dynamics via their linkage through ocean baroclinicity. These studies suggest that the
1876 mean state and subsurface biases in the state-of-the-art coupled climate models can largely limit
1877 the model's skill for regional climate prediction. The present study showed that even in forced
1878 ocean/sea-ice climate models, the subsurface temperature and salinity biases are persistent, with
1879 particular examples being the thermocline temperature biases that result in the inability of these
1880 modes to realistically represent the subsurface mean state. Therefore, more focused research is

1881 needed to improve the model physics and the realistic representation of bathymetry in the
1882 development of future climate models.

1883

1884 **7. Acknowledgements**

1885 The encouragement and facilities provided by the Director, Indian National Centre for Ocean
1886 Information Services (INCOIS), are gratefully acknowledged. Graphics were generated using the
1887 NOAA product Ferret. We thank Raghu Murthugude for useful suggestions that greatly
1888 improved the manuscript. We thank N Kiran Kumar for his help to generate the schematic
1889 diagram in Figure 1. J.V.D. acknowledges funding from the Helmholtz Association and the
1890 GEOMAR Helmholtz Centre for Ocean Research Kiel (grant IV014/GH018). This is INCOIS
1891 contribution no.xxxx. [We thank all five anonymous reviewers for their constructive comments](#)
1892 [by which we have improved the manuscript immensely.](#)

1893

1894

1895 **Appendix: Acronyms**

1896 ACCESS: Australian Community Climate and Earth System Simulator

1897 AS: Arabian Sea

1898 AWI: Alfred Wegener Institute

1899 BoB: Bay of Bengal

1900 BL: Barrier Layer

1901 CEC: Cross-Equatorial Cell

1902 CERFACS: Centre Européen de Recherche et de Formation Avancée en Calcul Scientifique

1903 CESM: Community Earth System Model

1904 CGCM: Coupled general circulation model

1905 CLIVAR: Climate Variability and Predictability

1906 CMCC: Centro Euro-Mediterraneo sui Cambiamenti Climatici

1907 CMIP3: Coupled Model Intercomparison Project Phase 3

1908 CMIP5: Coupled Model Intercomparison Project Phase 5

1909 CNRM: Centre National de Recherches Météorologiques

- 1910 CORE-II: Coordinated Ocean-ice Reference Experiments phase II
- 1911 [DRAKKAR: Coordination of high resolution global ocean simulations and developments of the](#)
- 1912 [NEMO modeling framework](#)
- 1913 EACC: East African Coastal Current
- 1914 EEIO: Eastern Equatorial Indian Ocean
- 1915 EICC: East India Coastal current
- 1916 ENSO: *El Niño* Southern Oscillation
- 1917 EUC: Equatorial Undercurrent
- 1918 FSU: Florida State University
- 1919 FSU2: Version 2 of the FSU contribution
- 1920 GFDL: Geophysical Fluid Dynamics Laboratory
- 1921 GOLD: Generalized Ocean Layer Dynamics
- 1922 GOOS: Global Ocean Observing System
- 1923 HYCOM: Hybrid Coordinate Ocean Model
- 1924 ICTP: International Centre for Theoretical Physics
- 1925 IOC: Intergovernmental Oceanographic Commission
- 1926 IOD: Indian Ocean Dipole
- 1927 IODZM: Indian Ocean Dipole/Zonal mode
- 1928 IOMOC: Indian Ocean Meridional overturning circulation
- 1929 ISMR: Indian Summer Monsoon Rainfall
- 1930 ITF: Indonesian through flow
- 1931 ITCZ: Inter Tropical Convergence Zone
- 1932 [JRA55-do: Japanese 55-year atmospheric reanalysis \(JRA-55\) based surface dataset for driving](#)
- 1933 [ocean-sea-ice models \(JRA55-do\) \(Tsujino et al., 2018\)](#)
- 1934 KIEL: Contribution from the Helmholtz Center for Ocean Research, Kiel, Germany
- 1935 [KPP: K-Profile Parameterization \(Large et al., 1994\)](#)
- 1936 LHF: Latent heat flux
- 1937 MLD: Mixed layer depth
- 1938 MOC: Meridional overturning circulation

- 1939 [NMC : Northeast Monsoon Current](#)
- 1940 NHF: Net Heat Flux
- 1941 *NOAA: National Oceanic and Atmospheric Administration*
- 1942 NOCS: National Oceanography Centre Southampton
- 1943 OSCAR: Ocean Surface Current Analysis
- 1944 Qa: specific humidity
- 1945 RAMA: Research Moored Array for African-Asian-Australian Monsoon Analysis & Prediction
- 1946 RMSD: Root-mean-square deviation
- 1947 SC: Somali current
- 1948 SD: Standard deviation
- 1949 SE: Socotra Eddy
- 1950 SEAS: South Eastern Arabian Sea
- 1951 SEC: South Equatorial Current
- 1952 SG: Southern Gyre
- 1953 SIO: Southern Indian Ocean
- 1954 [SICC: South Indian Ocean Counter Current](#)
- 1955 [SMC: Southwest Monsoon Current](#)
- 1956 SSS: Sea surface salinity
- 1957 SST: Sea surface temperature
- 1958 SSTC: Southern Subtropical Cell
- 1959 STC: Subtropical Cell
- 1960 SWIO: Southwest Indian Ocean
- 1961 Ta: Air temperature
- 1962 TIO: Tropical Indian Ocean
- 1963 TR: Thermocline Ridge
- 1964 WICC: West India Coastal current
- 1965 WJ: Wyrтки Jet
- 1966 WOA: World Ocean Atlas
- 1967

1968

1969 **References**

1970

1971 Adcroft, A., and J.-M. Campin, 2004: Rescaled height coordinates for accurate representation
1972 of free-surface flows in ocean circulation models, *Ocean Modelling*, 7, 269–284,
1973 doi:10.1016/j.ocemod.2003.09.003.

1974

1975 Annamalai, H., Liu, P., Xie, S.-P., 2005. Southwest Indian Ocean SST Variability: Its Local
1976 Effect and Remote Influence on Asian Monsoons. *J. Clim.* 18, 4150–4167.
1977 <https://doi.org/10.1175/JCLI3533.1>

1978

1979 Annamalai, H., Murtugudde, R., 2004. Role of the Indian Ocean in Regional Climate Variability,
1980 in: Wang, C., Xie, S.P., Carton, J.A. (Eds.), *Geophysical Monograph Series*. American
1981 Geophysical Union, Washington, D. C., pp. 213–246. <https://doi.org/10.1029/147GM13>

1982

1983 Annamalai, H., Murtugudde, R., Potemra, J., Xie, S., Liu, P., Wang, B., 2003. Coupled
1984 dynamics over the Indian Ocean: spring initiation of the Zonal Mode. *Deep Sea Res. Part II:*
1985 *Topical Studies in Oceanography* 50, 2305–2330. [https://doi.org/10.1016/S0967-0645\(03\)00058-](https://doi.org/10.1016/S0967-0645(03)00058-4)
1986 4

1987

1988 Antonov, J. I., Seidov, D., Boyer, T. P., Locarnini, R. A., Mishonov, A. V., Garcia, H. E., 2010.
1989 *World Ocean Atlas 2009 Volume 2: Salinity*. S. Levitus, Ed., NOAA Atlas NESDIS 69, U.S.
1990 Government Printing Office, Washington, D.C., 184 pp.

1991

1992 Ashok, K., Guan, Z., Yamagata, T., 2001. Impact of the Indian Ocean dipole on the relationship
1993 between the Indian monsoon rainfall and ENSO. *Geophys. Res. Lett.* 28, 4499–4502.
1994 <https://doi.org/10.1029/2001GL013294>

1995

- 1996 Atlas, R., Hoffman, R.N., Ardizzone, J., Leidner, S. M., Jusem, J. C., 2009. Development of a
1997 new cross-calibrated, multi-platform (CCMP) ocean surface wind product. paper presented at
1998 AMS 13th Conference on Integrated Observing and Assimilation Systems for Atmosphere,
1999 Oceans, and Land Surface (IOAS-AOLS), Phoenix, Ariz
- 2000
- 2001 Balmaseda, M. A., Mogensen, K., Weaver, A. T. 2013. Evaluation of the ECMWF ocean
2002 reanalysis system ORAS4. Q.J.R. Meteorol. Soc., 139: 1132–1161. doi: 10.1002/qj.2063
- 2003
- 2004 Berry, D.I., Kent, E.C., 2009. A New Air–Sea Interaction Gridded Dataset from ICOADS With
2005 Uncertainty Estimates. Bull. Am. Meteorol. Soc. 90, 645–
2006 656. <https://doi.org/10.1175/2008BAMS2639.1>
- 2007
- 2008 Bhat, G. S., Vecchi, G. A., Gadgil, S., 2004. Sea Surface Temperature of the Bay of Bengal
2009 derived from TRMM Microwave Imager, J. Atmos. Oceanic Technol., 21, 1283–1290,
2010 doi:[http://dx.doi.org/10.1175/1520-0426\(2004\)021<1283:SSTOTB>2.0.CO;2](http://dx.doi.org/10.1175/1520-0426(2004)021<1283:SSTOTB>2.0.CO;2).
- 2011
- 2012 Benschila, R., Durand, F., Masson, S., Bourdallé-Badie, R., de Boyer
2013 Montégut, C., Papa, F., Madec, G., 2014. The upper Bay of Bengal salinity structure in a high-
2014 resolution model. *Ocean Modelling* 74:36–52.
- 2015
- 2016 Beal, L.M., Donohue, K.A., 2013. The Great Whirl: Observations of its seasonal development
2017 and interannual variability: GREAT WHIRL. J. Geophys. Res. Oceans 118, 1–13.
2018 <https://doi.org/10.1029/2012JC008198>
- 2019
- 2020 Beal, L.M., Hormann, V., Lumpkin, R., Foltz, G.R., 2013. The Response of the Surface
2021 Circulation of the Arabian Sea to Monsoonal Forcing. J. Phys. Oceanogr. 43, 2008–2022.
2022 <https://doi.org/10.1175/JPO-D-13-033.1>
- 2023

- 2024
- 2025 Bonjean, F., Lagerloef, G.S.E., 2002. Diagnostic Model and Analysis of the Surface Currents in
2026 the Tropical Pacific Ocean. *J. Phys. Oceanogr.* 32, 2938–2954. [https://doi.org/10.1175/1520-](https://doi.org/10.1175/1520-0485(2002)032<2938:DMAAOT>2.0.CO;2)
2027 0485(2002)032<2938:DMAAOT>2.0.CO;2
- 2028
- 2029 Boyer, T.P., Antonov, J.I., Baranova, O.K., Garcia, H.E., Johnson, D.R., Locarnini, R.A.,
2030 Mishonov, A.V., O'Brien, T.D., Seidov, D., Smolyar, I.V., Zweng, M.M. 2009. World Ocean
2031 database—2009. In: Levitus S (ed) NOAA Atlas, NESDIS 66, US Govt. Printing Office,
2032 Washington, DC
- 2033
- 2034 Bray, N.A., Wijffels, S.E., Chong, J.C., Fieux, M., Hautala, S., Meyers, G., Morawitz, W.M.L.,
2035 1997. Characteristics of the Indo-Pacific Throughflow in the eastern Indian Ocean. *Geophys.*
2036 *Res. Lett.* 24, 2569–2572. <https://doi.org/10.1029/97GL51793>
- 2037
- 2038 Brodeau, L., Barnier, B., Treguier, A.-M., Penduff, T., Gulev, S., 2010. An ERA40-based
2039 atmospheric forcing for global ocean circulation models. *Ocean Model.* 31, 88–104.
2040 <https://doi.org/10.1016/j.ocemod.2009.10.005>
- 2041
- 2042 Cane, M.A., 1980. On the dynamics of equatorial currents, with application to the Indian Ocean.
2043 *Deep Sea Res. Part A. Oceanographic Research Papers* 27, 525–544.
2044 [https://doi.org/10.1016/0198-0149\(80\)90038-2](https://doi.org/10.1016/0198-0149(80)90038-2)
- 2045
- 2046 Cai, W. and Cowan, T., 2013. Why is the amplitude of the Indian Ocean Dipole overly large in
2047 CMIP3 and CMIP5 climate models? *Geophys. Res. Lett.* 40: 1200– 1205.
- 2048
- 2049 Cai, W., Santoso, A., Wang, G., Weller, E., Wu, L., Ashok, K., Masumoto, Y., Yamagata, T.,
2050 2014. Increased frequency of extreme Indian Ocean Dipole events due to greenhouse warming.
2051 *Nature* 510, 254–258. <https://doi.org/10.1038/nature13327>.
- 2052

- 2053 Chen, D., Busalacchi, A.J., Rothstein, L.M., 1994. The roles of vertical mixing, solar radiation,
2054 and wind stress in a model simulation of the sea surface temperature seasonal cycle in the
2055 tropical Pacific Ocean. *J. Geophys. Res.* 99, 20345. <https://doi.org/10.1029/94JC01621>
2056
- 2057 Chen, G., Han, W., Li, Y., Wang, D., McPhaden, M.J., 2015. Seasonal-to-Interannual Time-
2058 Scale Dynamics of the Equatorial Undercurrent in the Indian Ocean. *J. Phys. Oceanogr.* 45,
2059 1532–1553. <https://doi.org/10.1175/JPO-D-14-0225.1>
2060
- 2061 Chirokova, G., Webster, P.J., 2006. Interannual Variability of Indian Ocean Heat Transport. *J.*
2062 *Clim.* 19, 1013–1031. <https://doi.org/10.1175/JCLI3676.1>
2063
- 2064 Chaudhari, H.S., Pokhrel, S., Saha, S.K., Dhakate, A., Yadav, R.K., Salunke, K., Mahapatra, S.,
2065 Sabeerali, C.T., Rao, S.A., 2013. Model biases in long coupled runs of NCEP CFS in the context
2066 of Indian summer monsoon. *International J. Clim.* 33, 1057–1069.
2067 <https://doi.org/10.1002/joc.3489>
2068
- 2069 Chowdary, J.S., Parekh, A., Ojha, S., Gnanaseelan, C., 2015. Role of upper ocean processes in
2070 the seasonal SST evolution over tropical Indian Ocean in climate forecasting system. *Clim. Dyn.*
2071 45, 2387–2405. <https://doi.org/10.1007/s00382-015-2478-4>
- 2072 Chen, Z., Wu, L., Qiu, B., Sun, S., Jia, F., 2014. Seasonal Variation of the South Equatorial
2073 Current Bifurcation off Madagascar. *J. Phys. Oceanogr.*, 44, 618–631,
2074 <https://doi.org/10.1175/JPO-D-13-0147.1>
2075
- 2076 Chowdary, J.S., Parekh, A., Ojha, S., Gnanaseelan, C., Kakatkar, R., 2016. Impact of upper
2077 ocean processes and air-sea fluxes on seasonal SST biases over the tropical Indian Ocean in the
2078 NCEP Climate Forecasting System: Seasonal SST biases in the tropical Indian Ocean.
2079 *International J. Clim.* 36, 188–207. <https://doi.org/10.1002/joc.4336>
2080

- 2081 Colborn, J., 1975. The thermal structure of the Indian Ocean. The University Press, Hawaii 173
2082 pp
2083
- 2084 Cooper, N. S., 1988. The effect of salinity on tropical ocean models, *J. Phys. Oceanogr.*, 18, 697–
2085 707.
2086
- 2087 Cutler, A. N., Swallow, J. C. 1984. Surface currents of the Indian Ocean, (to 25°S, 100°E),
2088 Tech. Rep., 187, 8 pp., 36 charts, Inst. of Oceanogr. Sci., Wormley, Godalming, Surrey,
2089 England.
2090
- 2091 Danabasoglu, G., Yeager, S.G., Bailey, D., Behrens, E., Bentsen, M., Bi, D., Biastoch, A.,
2092 Böning, C., Bozec, A., Canuto, V.M., Cassou, C., Chassignet, E., Coward, A.C., Danilov, S.,
2093 Diansky, N., Drange, H., Farneti, R., Fernandez, E., Fogli, P.G., Forget, G., Fujii, Y., Griffies,
2094 S.M., Gusev, A., Heimbach, P., Howard, A., Jung, T., Kelley, M., Large, W.G., Leboissetier, A.,
2095 Lu, J., Madec, G., Marsland, S.J., Masina, S., Navarra, A., George Nurser, A.J., Pirani, A., y
2096 Méliá, D.S., Samuels, B.L., Scheinert, M., Sidorenko, D., Treguier, A.-M., Tsujino, H., Uotila,
2097 P., Valcke, S., Voldoire, A., Wang, Q., 2014. North Atlantic simulations in Coordinated Ocean-
2098 ice Reference Experiments phase II (CORE-II). Part I: Mean states. *Ocean Model.* 73, 76–107.
2099 <https://doi.org/10.1016/j.ocemod.2013.10.005>
2100
- 2101 Danabasoglu, G., Yeager, S.G., Kim, W.M., Behrens, E., Bentsen, M., Bi, D., Biastoch, A.,
2102 Bleck, R., Böning, C., Bozec, A., Canuto, V.M., Cassou, C., Chassignet, E., Coward, A.C.,
2103 Danilov, S., Diansky, N., Drange, H., Farneti, R., Fernandez, E., Fogli, P.G., Forget, G., Fujii,
2104 Y., Griffies, S.M., Gusev, A., Heimbach, P., Howard, A., Ilicak, M., Jung, T., Karspeck, A.R.,
2105 Kelley, M., Large, W.G., Leboissetier, A., Lu, J., Madec, G., Marsland, S.J., Masina, S.,
2106 Navarra, A., Nurser, A.J.G., Pirani, A., Romanou, A., Salas y Méliá, D., Samuels, B.L.,
2107 Scheinert, M., Sidorenko, D., Sun, S., Treguier, A.-M., Tsujino, H., Uotila, P., Valcke, S.,
2108 Voldoire, A., Wang, Q., Yashayaev, I., 2016. North Atlantic simulations in Coordinated Ocean-

2109 ice Reference Experiments phase II (CORE-II). Part II: Inter-annual to decadal variability. *Ocean*
2110 *Model.* 97, 65–90. <https://doi.org/10.1016/j.ocemod.2015.11.007>

2111
2112 Dai, A., Qian, T., Trenberth, K. E., and Milliman, J. D., 2009. Changes in continental freshwater
2113 discharge from 1948 to 2004, *J. Climate*, 22, 2773–2792.

2114
2115 deBoyer Montégutet, C., Vialard, J., Shenoi, S.S.C., Shankar, D., Durand, F., Ethé, C., Madec,
2116 G., 2007. Simulated seasonal and interannual variability of mixed layer heat budget in the
2117 northern Indian Ocean. *J. Clim.* 20, 3249-3268.

2118
2119 Dee, D.P., Uppala, S.M., Simmons, A.J., Berrisford, P., Poli, P., Kobayashi, S., Andrae, U.,
2120 Balmaseda, M.A., Balsamo, G., Bauer, P., Bechtold, P., Beljaars, A.C.M., van de Berg, L.,
2121 Bidlot, J., Bormann, N., Delsol, C., Dragani, R., Fuentes, M., Geer, A.J., Haimberger, L., Healy,
2122 S.B., Hersbach, H., Hólm, E.V., Isaksen, L., Kållberg, P., Köhler, M., Matricardi, M., McNally,
2123 A.P., Monge-Sanz, B.M., Morcrette, J.-J., Park, B.-K., Peubey, C., de Rosnay, P., Tavolato, C.,
2124 Thépaut, J.-N., Vitart, F., 2011. The ERA-Interim reanalysis: configuration and performance of
2125 the data assimilation system. *Quarterly J. R. Meteorol. Soc.* 137, 553–597.
2126 <https://doi.org/10.1002/qj.828>

2127
2128 Du, Y., Xie, S.-P., Huang, G., Hu, K., 2009. Role of air-sea interaction in the long persistence of
2129 El Niño-induced North Indian Ocean warming, *J. Clim.*, 22, 2023–2038,
2130 [doi:10.1175/2008JCLI2590.1](https://doi.org/10.1175/2008JCLI2590.1).

2131
2132 Du, Y., Qu, T., Meyers, G., Masumoto, Y., Sasaki, H., 2005. Seasonal heat budget in the mixed
2133 layer of the southeastern tropical Indian Ocean in a high-resolution ocean general circulation
2134 model, *J. Geophys. Res.*, 110, C04012, [doi:10.1029/2004JC002845](https://doi.org/10.1029/2004JC002845).

2135

- 2136 Durgadoo, J. V., Ruhs, S., Biastoch, A., Boning, C.W.B., 2017. Indian Ocean sources of Agulhas
2137 leakage, *J. Geophys. Res. Oceans*, 122, 3481–3499, doi:10.1002/2016JC012676
2138
- 2139 Durand, F., Shetye, S. R., Vialard, J., Shankar, D., Shenoi, S. S. C., Ethe, C., Madec, G., 2004.
2140 Impact of temperature inversions on SST evolution in the South-Eastern Arabian Sea during the
2141 pre-summer monsoon season, *Geophys. Res. Lett.*, 31, L01305, doi:10.1029/2003GL018906.
2142
- 2143 Durand, F., Papa, F., Rahman, A., Bala, S.K., 2011. Impact of Ganges–Brahmaputra interannual
2144 discharge variations on Bay of Bengal salinity and temperature during 1992–1999 period. *J.*
2145 *Earth Syst. Sci.* 120, 859–872. <https://doi.org/10.1007/s12040-011-0118-x>
2146
- 2147 Durgadoo, J.V., Rühls, S., Biastoch, A., Böning, C.W.B., 2017. Indian Ocean sources of Agulhas
2148 leakage, *J. Geophys. Res.*, 122, 3481–3499, doi:10.1002/2016JC012676.
2149
- 2150 Eyring, V., Bony, S., Meehl, G. A., Senior, C. A., Stevens, B., Stouffer, R. J., and Taylor, K. E.:
2151 Overview of the Coupled Model Intercomparison Project Phase 6 (CMIP6) experimental design
2152 and organization, *Geosci. Model Dev.*, 9, 1937–1958, <https://doi.org/10.5194/gmd-9-1937-2016>,
2153 2016.
2154
- 2155 Fasullo, J., Webster, P.J., 1999. Warm Pool SST Variability in Relation to the Surface Energy
2156 Balance. *J. Clim.* 12, 1292–1305. [https://doi.org/10.1175/1520-
2157 0442\(1999\)012<1292:WPSVIR>2.0.CO;2](https://doi.org/10.1175/1520-0442(1999)012<1292:WPSVIR>2.0.CO;2)
2158
- 2159 Fathrio, I., Iizuka, S., Manda, A., Kodama, Y.-M., Ishida, S., Moteki, Q., Yamada, H.,
2160 Tachibana, Y., 2017a. Assessment of western Indian Ocean SST bias of CMIP5 models: Western
2161 Indian Ocean SST bias of CMIP5. *J. Geophys. Res. Oceans* 122, 3123–3140.
2162 <https://doi.org/10.1002/2016JC012443>
2163

2164 Fathrio, I., Manda, A., Iizuka, S., Kodama, Y.-M., Ishida, S., 2017b. Evaluation of CMIP5
2165 models on sea surface salinity in the Indian Ocean. IOP Conference Series: Earth and
2166 Environmental Science 54, 012039. <https://doi.org/10.1088/1755-1315/54/1/012039>

2167
2168 Flato, G., Marotzke, J., Abiodun, B., Braconnot, P., Chou, S.C., Collins, W., Cox, P., Driouech, F.,
2169 Emori, S., Eyring, V., Forest, C., Gleckler, P., Guilyardi, E., Jakob, C., Kattsov, V., Reason, C.,
2170 Rummukainen, M., 2013. Evaluation of Climate Models. In: Climate Change 2013: The Physical
2171 Science Basis. Contribution of Working Group I to the Fifth Assessment Report of the
2172 Intergovernmental Panel on Climate Change [Stocker, T.F., D. Qin, G.-K. Plattner, M. Tignor,
2173 S.K. Allen, J. Boschung, A. Nauels, Y. Xia, V. Bex and P.M. Midgley (eds.)]. Cambridge
2174 University Press, Cambridge, United Kingdom and New York, NY, USA

2175
2176 Farneti, R., Downes, S. M., Griffies, S. M., Marsland, S. J., Bailey, D., Behrens, E., Bentsen, M.,
2177 Bi, D., Biastoch, A., Boning, C., Bozec, A., Chassignet, E., Danabasoglu, G., Danilov, S.,
2178 Diansky, N., Drange, H., Fogli, P. G., Gusev, A., Hallberg, R. W., Howard, A., Kelley, M.,
2179 Illicak, M., Large, W. G., Leboissetier, A., Long, M., Lu, J., Masina, S., Mishra, A., Navarra, A.,
2180 Nurser, A. J. G., Patarra, L., Samuels, B. L., Sidorenko, D., Tsujino, H., Uotila, P., Yeager, S. G.,
2181 Wang, Q., 2015. An assessment of Antarctic Circumpolar Current and Southern Ocean
2182 meridional overturning circulation during 1958–2007 in a suite of interannual CORE-II
2183 simulations, *Ocean Model.*, doi: 10.1016/j.ocemod.2015.07.009

2184
2185 Gadgil, S., 2003. The Indian monsoon and its variability. *Annu. Rev. Earth Planet. Sci.* 31, 429–
2186 467. <https://doi.org/10.1146/annurev.earth.31.100901.141251>

2187
2188 Gadgil, S., Joseph, P.V., Joshi, N.V., 1984. Ocean–atmosphere coupling over monsoon regions.
2189 *Nature* 312, 141–143. <https://doi.org/10.1038/312141a0>

2190

- 2191 Gadgil, S., Rajeevan, M., Nanjundiah, R., 2005. Monsoon prediction – Why yet another failure?
2192 CURRENT SCIENCE 88, 12.
2193
- 2194 Garternicht, U., Schott, F., 1997. Heat fluxes of the Indian Ocean from a global eddy-resolving
2195 model. *J. Geophys. Res. Oceans* 102, 21147–21159. <https://doi.org/10.1029/97JC01585>
2196
- 2197 Girishkumar, M.S., Ravichandran, M., McPhaden, M.J., Rao, R.R., 2011. Intraseasonal
2198 variability in barrier layer thickness in the south central Bay of Bengal. *J. Geophys. Res.* 116.
2199 <https://doi.org/10.1029/2010JC006657>
2200
- 2201 Godfrey, J.S., 1996. The effect of the Indonesian throughflow on ocean circulation and heat
2202 exchange with the atmosphere: A review. *J. Geophys. Res. Oceans* 101, 12217–12237.
2203 <https://doi.org/10.1029/95JC03860>
2204
- 2205 Godfrey, J.S., Hu, R.-J., Schiller, A., Fiedler, R., 2007. Explorations of the Annual Mean Heat
2206 Budget of the Tropical Indian Ocean. Part I: Studies with an Idealized Model. *J. Clim.* 20, 3210–
2207 3228. doi:10.1175/JCLI4157.1
2208
- 2209 Graham, N. E., Barnett, T. P., 1987. Sea surface temperature surface wind divergence and
2210 convection over tropical oceans *Science*, 238, 657-659.
2211
- 2212 Gordon, A.L., Fine, R.A., 1996. Pathways of water between the Pacific and Indian oceans in the
2213 Indonesian seas. *Nature* 379, 146–149. <https://doi.org/10.1038/379146a0>
2214
- 2215 Gordon, A.L., Sprintall, J., Van Aken, H.M., Susanto, D., Wijffels, S., Molcard, R., Field, A.,
2216 Pranowo, W., Wirasantosa, S., 2010. The Indonesian throughflow during 2004–2006 as observed
2217 by the INSTANT program. *Dyn. of Atmospheres Oceans* 50, 115–128.
2218 <https://doi.org/10.1016/j.dynatmoce.2009.12.002>
2219

- 2220 Griffies, S. M., (2009), Elements of MOM4p1. GFDL Ocean Group Tech. Rep. 6, 377 pp.
2221 [Available online at http://data1.gfdl.noaa.gov/~arl/pubrel/o/old/doc/mom4p1_guide.pdf.]
- 2222
- 2223 Griffies, S.M., Biastoch, A., Böning, C., Bryan, F., Danabasoglu, G., Chassignet, E.P., England,
2224 M.H., Gerdes, R., Haak, H., Hallberg, R.W., Hazeleger, W., Jungclaus, J., Large, W.G., Madec,
2225 G., Pirani, A., Samuels, B.L., Scheinert, M., Gupta, A.S., Severijns, C.A., Simmons, H.L.,
2226 Treguier, A.M., Winton, M., Yeager, S., Yin, J., 2009. Coordinated Ocean-ice Reference
2227 Experiments (COREs). *Ocean Model.* 26, 1–46. <https://doi.org/10.1016/j.ocemod.2008.08.007>
- 2228
- 2229 Griffies, S.M., Danabasoglu, G., Durack, P.J., Adcroft, A.J., Balaji, V., Böning, C.W.,
2230 Chassignet, E.P., Curchitser, E., Deshayes, J., Drange, H., Fox-Kemper, B., Gleckler, P.J.,
2231 Gregory, J.M., Haak, H., Hallberg, R.W., Hewitt, H.T., Holland, D.M., Ilyina, T., Jungclaus,
2232 J.H., Komuro, Y., Krasting, J.P., Large, W.G., Marsland, S.J., Masina, S., McDougall, T.J.,
2233 Nurser, A.J.G., Orr, J.C., Pirani, A., Qiao, F., Stouffer, R.J., Taylor, K.E., Treguier, A.M.,
2234 Tsujino, H., Uotila, P., Valdivieso, M., Winton, M., Yeager, S.G., 2016. Experimental and
2235 diagnostic protocol for the physical component of the CMIP6 Ocean Model Intercomparison
2236 Project (OMIP). *Geosci. Model Dev. Discuss.* 1–108. <https://doi.org/10.5194/gmd-2016-77>
- 2237
- 2238 Griffies, S.M., Pacanowski, R.C., Hallberg, R.W., 2000. Spurious Diapycnal Mixing Associated
2239 with Advection in a z -Coordinate Ocean Model. *Monthly Weather Review* 128, 538–564.
2240 [https://doi.org/10.1175/1520-0493\(2000\)128<0538:SDMAWA>2.0.CO;2](https://doi.org/10.1175/1520-0493(2000)128<0538:SDMAWA>2.0.CO;2)
- 2241
- 2242 Griffies, S.M., Yin, J., Durack, P.J., Goddard, P., Bates, S.C., Behrens, E., Bentsen, M., Bi, D.,
2243 Biastoch, A., Böning, C.W., Bozec, A., Chassignet, E., Danabasoglu, G., Danilov, S.,
2244 Domingues, C.M., Drange, H., Farneti, R., Fernandez, E., Greatbatch, R.J., Holland, D.M.,
2245 Ilicak, M., Large, W.G., Lorbacher, K., Lu, J., Marsland, S.J., Mishra, A., George Nurser, A.J.,
2246 Salas y Mélia, D., Palter, J.B., Samuels, B.L., Schröter, J., Schwarzkopf, F.U., Sidorenko, D.,
2247 Treguier, A.M., Tseng, Y., Tsujino, H., Uotila, P., Valcke, S., Voltaire, A., Wang, Q., Winton,

- 2248 M., Zhang, X., 2014. An assessment of global and regional sea level for years 1993–2007 in a
2249 suite of interannual CORE-II simulations. *Ocean Model.* 78, 35–89.
2250 <https://doi.org/10.1016/j.ocemod.2014.03.004>
2251
- 2252 Han, W., McCreary, J.P., 2001. Modeling salinity distributions in the Indian Ocean. *J. Geophys.*
2253 *Res. Oceans* 106, 859–877. <https://doi.org/10.1029/2000JC000316>
2254
- 2255 Han, W., McCreary, J.P., Kohler, K.E., 2001. Influence of precipitation minus evaporation and
2256 Bay of Bengal rivers on dynamics, thermodynamics, and mixed layer physics in the upper Indian
2257 Ocean. *J. Geophys. Res. Oceans* 106, 6895–6916. <https://doi.org/10.1029/2000JC000403>
2258
2259
- 2260 Han, W., Vialard, J., McPhaden, M.J., Lee, T., Masumoto, Y., Feng, M., de Ruijter, W.P.M.,
2261 2014. Indian Ocean Decadal Variability: A Review. *Bull. Am. Meteorol. Soc.* 95, 1679–1703.
2262 <https://doi.org/10.1175/BAMS-D-13-00028.1>
2263
2264
- 2265 Haney, R. L., 1971. Surface thermal boundary conditions for ocean circulation models. *J. Phys.*
2266 *Oceanogr.* 1, 241–248
2267
- 2268 Halkides, D.J., Lee, T., 2009. Mechanisms controlling seasonal-to-interannual mixed layer
2269 temperature variability in the southeastern tropical Indian Ocean. *J. Geophys. Res. Oceans* 114,
2270 C02012, [doi:10.1029/2008JC004949](https://doi.org/10.1029/2008JC004949).
2271
- 2272 Hirons L, Turner, A., 2018. The impact of Indian Ocean mean-state biases in climate models
2273 on the representation of the East African short rains. *J. Clim.* 31(16):6611–
2274 6631. <https://doi.org/10.1175/JCLI-D-17-0804.1>

- 2275 Horii, T., Mizuno, K., Nagura, M., Miyama, T., Ando, K., 2013. Seasonal and interannual
2276 variation in the cross-equatorial meridional currents observed in the eastern Indian Ocean, J.
2277 Geophys. Res. Oceans, 118, doi:10.1002/2013JC009291.
- 2278
- 2279 Howden, S.D., Murtugudde, R., 2001. Effects of river inputs into the Bay of Bengal. J. Geophys.
2280 Res. Oceans 106, 19825–19843. <https://doi.org/10.1029/2000JC000656>
- 2281
- 2282 Huang, B., Kinter III and J. L., 2002. Interannual variability in the tropical Indian Ocean, J.
2283 Geophys. Res., 107(C11), 3199, doi:10.1029/2001JC001278.
- 2284 Ilicak, M., Drange, H., Wang, Q., Gerdes, R., Aksenov, Y., Bailey, D., Bentsen, M., Biastoch,
2285 A., Bozec, A., Böning, C., Cassou, C., Chassignet, E., Coward, A.C., Curry, B., Danabasoglu,
2286 G., Danilov, S., Fernandez, E., Fogli, P.G., Fujii, Y., Griffies, S.M., Iovino, D., Jahn, A., Jung,
2287 T., Large, W.G., Lee, C., Lique, C., Jianhua, L., Simona, M.A.J., Nurser, G., Roth, C., David,
2288 S.Y., Mlija, B.L., Samuels, P.S., Tsujino, H., Valcke, S., Voldoire, A., Wang, X., Yeager, S.G.,
2289 2016. An assessment of the arctic ocean in a suite of interannual core-II simulations. Part III:
2290 Hydrography and fluxes. Ocean Modell 100:141–
2291 161. <https://doi.org/10.1016/j.ocemod.2016.02.004>
- 2292
- 2293 Ilicak, M., Adcroft, A.J., Griffies, S.M., Hallberg, R.W., 2012. Spurious diapycnal mixing and
2294 the role of momentum closure. Ocean Model. 45–46, 37–58.
2295 <https://doi.org/10.1016/j.ocemod.2011.10.003>
- 2296
- 2297 Iskandar, I., Masumoto, Y., Mizuno, K., 2009. Subsurface equatorial zonal current in the eastern
2298 Indian Ocean. J. Geophys. Res. 114. <https://doi.org/10.1029/2008JC005188>
- 2299
- 2300
- 2301 Jensen, T.G., 2007. Wind-Driven Response of the Northern Indian Ocean to Climate Extremes.
2302 J. Clim. 20, 2978–2993. <https://doi.org/10.1175/JCLI4150.1>

- 2303
2304 Jensen, T.G., 2003. Cross-equatorial pathways of salt and tracers from the northern Indian
2305 Ocean: Modelling results. *Deep Sea Res. Part II: Topical Studies in Oceanography* 50, 2111–
2306 2127. [https://doi.org/10.1016/S0967-0645\(03\)00048-1](https://doi.org/10.1016/S0967-0645(03)00048-1)
2307
- 2308 Jensen, T.G., 2001. Arabian Sea and Bay of Bengal exchange of salt and tracers in an ocean
2309 model. *Geophys. Res. Lett.* 28, 3967–3970. <https://doi.org/10.1029/2001GL013422>
2310
- 2311 Joseph, P.V., 1990. Warm pool in the Indian Ocean and monsoon onset. *Trop Ocean Atmos*
2312 *News Lett* 53:1–5
2313
- 2314 Joseph, P.V., Sooraj, K.P., Rajan, C.K., 2006. The summer monsoon onset process over South
2315 Asia and an objective method for the date of monsoon onset over Kerala. *International J.*
2316 *Climatol.* 26, 1871–1893. <https://doi.org/10.1002/joc.1340>
2317
- 2318 Kataoka, T., Tozuka, T., Masumoto, Y., Yamagata, T., 2012. The Indian Ocean subtropical
2319 dipole mode simulated in the CMIP3 models. *Clim Dyn* 39:1385–1399
2320
- 2321 Kara, A.B., Rochford, P.A., Hurlburt, H.E., 2000. An optimal definition for ocean mixed layer
2322 depth. *J. Geophys. Res. Oceans* 105, 16803–16821. <https://doi.org/10.1029/2000JC900072>
2323
- 2324 Karmakar A, Parekh, A., Chowdary, J.S., Gnanaseelan, C., 2017. Inter comparison of Tropical
2325 Indian Ocean features in different ocean reanalysis products. *Clim Dyn*: 1–
2326 23. <https://doi.org/10.1007/s00382-017-3910-8>.
2327
- 2328 Klein, S.A., Soden, B.J., Lau, N.-C., 1999. Remote Sea Surface Temperature Variations during
2329 ENSO: Evidence for a Tropical Atmospheric Bridge. *J. Clim.* 12, 917–932.
2330 [https://doi.org/10.1175/1520-0442\(1999\)012<0917:RSSTVD>2.0.CO;2](https://doi.org/10.1175/1520-0442(1999)012<0917:RSSTVD>2.0.CO;2)
2331

- 2332 Knox, R.A., 1981. Time variability of Indian Ocean equatorial currents. *Deep Sea Res. Part A.*
2333 *Oceanographic Research Papers* 28, 291–295. [https://doi.org/10.1016/0198-0149\(81\)90068-6](https://doi.org/10.1016/0198-0149(81)90068-6)
2334
- 2335 Knox, R.A., 1976. On a long series of measurements of Indian Ocean equatorial currents near
2336 Addu Atoll. *Deep Sea Res. and Oceanographic Abstracts* 23, 211-IN1.
2337 [https://doi.org/10.1016/0011-7471\(76\)91325-5](https://doi.org/10.1016/0011-7471(76)91325-5)
2338
- 2339 Kobayashi, S., Ota, Y., Harada, Y., Ebata, A., Moriya, M., Onoda, H., Onogi, K., Kamahori, H.,
2340 Kobayashi, C., Endo, H., Miyaoka, K., Takahashi, K., 2015. The JRA-55 reanalysis: General
2341 specifications and basic characteristics. *J. Meteor. Soc. Japan* 93, 5–48. doi:10.2151/jmsj.2015-
2342 001.
2343
- 2344 Kurian, J., Vinayachandran, P.N., 2007. Mechanisms of formation of the Arabian Sea mini warm
2345 pool in a high-resolution Ocean General Circulation Model. *J. Geophys. Res.* 112.
2346 <https://doi.org/10.1029/2006JC003631>
2347
- 2348 Large, W., Yeager, S., 2004. Diurnal to decadal global forcing for ocean and sea ice models: the
2349 data sets and climatologies. Technical Report TN-460+STR, NCAR, 105 p.
2350
- 2351 Large, W.G., Yeager, S.G., 2009. The global climatology of an interannually varying air–sea
2352 flux data set. *Clim. Dyn.* 33, 341–364. <https://doi.org/10.1007/s00382-008-0441-3>
2353
- 2354 Lau, N.-C., Nath, M. J., 2004. Coupled GCM simulation of atmosphere-ocean variability
2355 associated with zonally asymmetric SST changes in the tropical Indian Ocean, *J. Clim.*, 17, 245–
2356 265.
2357
- 2358 Legg, S., Briegleb, B., Chang, Y., Chassignet, E.P., Danabasoglu, G., Ezer, T., Gordon, A.L.,
2359 Griffies, S., Hallberg, R., Jackson, L., Large, W., Özgökmen, T.M., Peters, H., Price, J.,

- 2360 Riemenschneider, U., Wu, W., Xu, X., Yang, J. 2009. Improving oceanic overflow
2361 representation in climate models. The gravity current entrainment climate process team.
2362 American Meteorological Society, Washington, DC, pp 657–670
2363
- 2364 Lee, J.-Y., Wang, B., Kang, I.-S., Shukla, J., Kumar, A., Kug, J.-S., Schemm, J.K.E., Luo, J.-J.,
2365 Yamagata, T., Fu, X., Alves, O., Stern, B., Rosati, T., Park, C.-K., 2010. How are seasonal
2366 prediction skills related to models' performance on mean state and annual cycle? *Clim. Dyn.* 35,
2367 267–283. <https://doi.org/10.1007/s00382-010-0857-4>
2368
- 2369 Lee, T., 2004. Decadal weakening of the shallow overturning circulation in the South Indian
2370 Ocean. *Geophys. Res. Lett.* 31. <https://doi.org/10.1029/2004GL020884>
2371
- 2372 Lee, T., Marotzke, J., 1998. Seasonal Cycles of Meridional Overturning and Heat Transport of
2373 the Indian Ocean. *J. Phys. Oceanogr.* 28, 923–943. [https://doi.org/10.1175/1520-](https://doi.org/10.1175/1520-0485(1998)028<0923:SCOMOA>2.0.CO;2)
2374 [0485\(1998\)028<0923:SCOMOA>2.0.CO;2](https://doi.org/10.1175/1520-0485(1998)028<0923:SCOMOA>2.0.CO;2)
2375
- 2376 Lee, T., Marotzke, J., 1997. Inferring meridional mass and heat transports of the Indian Ocean by
2377 fitting a general circulation model to climatological data. *J. Geophys. Res. Oceans* 102, 10585–
2378 10602. <https://doi.org/10.1029/97JC00464>
2379
- 2380 Levine, R.C., Turner, A.G., 2012. Dependence of Indian monsoon rainfall on moisture fluxes
2381 across the Arabian Sea and the impact of coupled model sea surface temperature biases. *Clim.*
2382 *Dyn.* 38, 2167–2190. <https://doi.org/10.1007/s00382-011-1096-z>
2383
- 2384 Levine, R.C., Turner, A.G., Marathayil, D., Martin, G.M., 2013. The role of northern Arabian
2385 Sea surface temperature biases in CMIP5 model simulations and future projections of Indian
2386 summer monsoon rainfall. *Clim. Dyn.* 41, 155–172. <https://doi.org/10.1007/s00382-012-1656-x>
2387

- 2388 Levitus, S., 1987. A comparison of the annual cycle of two sea surface temperature climatology
2389 of the World Ocean.
2390
- 2391 Levitus, S., 1983. Climatological Atlas of the World Ocean. Eos, Transactions American
2392 Geophysical Union 64, 962. <https://doi.org/10.1029/EO064i049p00962-02>
2393
- 2394 Li, G., Xie, S.-P., Du, Y., 2015. Monsoon-Induced Biases of Climate Models over the Tropical
2395 Indian Ocean. *J. Clim.* 28, 3058–3072. <https://doi.org/10.1175/JCLI-D-14-00740.1>
2396
- 2397 Li, G., Xie, S.-P., Du, Y., 2016. A robust but spurious pattern of climate change in model
2398 projections over the Tropical Indian Ocean. *J. Clim.* 29, 5589–5608.
2399 <https://doi.org/10.1175/JCLI-D-15-0565.1>.
2400
- 2401 Li, G., Xie, S.P., He, C., Chen, Z., 2017. Western Pacific emergent constraint lowers projected
2402 increase in Indian summer monsoon rainfall. *Nat. Clim. Chang.* 7, 708–712.
2403 <https://doi.org/10.1038/nclimate3387>.
2404
- 2405 Li, T., Zhang, Y., Chang, C.-P., Wang, Bin., 2001. On the relationship between Indian Ocean
2406 SST and Asian summer monsoon. *Geophys. Res. Lett.* 28. 2843-2846. [10.1029/2000GL011847](https://doi.org/10.1029/2000GL011847).
2407
- 2408 Locarnini, R. A., Mishonov, A. V., Antonov, J. I., Boyer, T. P., Garcia, H. E., 2010. World Ocean
2409 Atlas 2009, Volume 1: Temperature. S. Levitus, Ed., NOAA Atlas NESDIS 68, U.S.
2410 Government Printing Office, Washington, D.C., 184 pp.
2411
- 2412 Lumpkin, R., Johnson, G.C., 2013. Global ocean surface velocities from drifters: Mean,
2413 variance, El Niño-Southern Oscillation response, and seasonal cycle: Global Ocean Surface
2414 Velocities. *J. Geophys. Res. Oceans* 118, 2992–3006. <https://doi.org/10.1002/jgrc.20210>

- 2415 Luther, M.E., O'Brien, J.J., 1985. A model of the seasonal circulation in the Arabian Sea forced
2416 by observed winds. *Prog. Oceanogr.* 14, 353–385. [https://doi.org/10.1016/0079-6611\(85\)90017-](https://doi.org/10.1016/0079-6611(85)90017-5)
2417 5
- 2418 Lutjeharms, J. R. E., 2006. *The Agulhas Current*. Springer-Verlag, Berlin Heidelberg. 329pp.
2419
- 2420 Marathayil, D., Turner, A.G., Shaffrey, L.C., Levine, R.C., 2013. Systematic winter sea-surface
2421 temperature biases in the northern Arabian Sea in HiGEM and the CMIP3 models. *Environ. Res.*
2422 *Lett.* 8, 014028. <https://doi.org/10.1088/1748-9326/8/1/014028>
2423
- 2424 Masson, S., Delecluse, P., Boulanger, J.-P., Menkes, C., 2002. A model study of the seasonal
2425 variability and formation mechanisms of the barrier layer in the eastern equatorial Indian Ocean:
2426 barrier layer in the eastern Indian Ocean. *J. Geophys. Res. Oceans* 107, SRF 18-1-SRF 18-20.
2427 <https://doi.org/10.1029/2001JC000832>
2428
- 2429 Masson, S., Luo, J.-J., Madec, G., Vialard, J., Durand, F., Gualdi, S., Guilyardi, E., Behera, S.,
2430 Delecluse, P., Navarra, A., Yamagata, T., 2005. Impact of barrier layer on winter-spring
2431 variability of the southeastern Arabian Sea: barrier layer impact on the southeastern Arabian Sea.
2432 *Geophys. Res. Lett.* 32, n/a-n/a. <https://doi.org/10.1029/2004GL021980>
2433
- 2434 McCreary, J.P., Kohler, K.E., Hood, R.R., Smith, S., Kindle, J., Fischer, A.S., Weller, R.A.,
2435 2001. Influences of diurnal and intraseasonal forcing on mixed-layer and biological variability in
2436 the central Arabian Sea. *J. Geophys. Res. Oceans* 106, 7139–7155.
2437 <https://doi.org/10.1029/2000JC900156>
2438
- 2439
- 2440 McCreary, J.P., Kundu, P.K., Molinari, R.L., 1993. A numerical investigation of dynamics,
2441 thermodynamics and mixed-layer processes in the Indian Ocean. *Prog. Oceanogr.* 31, 181–244.
2442 [https://doi.org/10.1016/0079-6611\(93\)90002-U](https://doi.org/10.1016/0079-6611(93)90002-U)
2443

- 2444 McPhaden, M.J., 1986. The equatorial undercurrent: 100 years of discovery. *Eos, Transactions*
2445 *American Geophysical Union* 67, 762. <https://doi.org/10.1029/EO067i040p00762>
2446
- 2447 McPhaden, M.J., Wang, Y., Ravichandran, M., 2015. Volume transports of the Wyrтки jets and
2448 their relationship to the Indian Ocean Dipole: WYRTKI JET TRANSPORTS. *J. Geophys. Res.*
2449 *Oceans* 120, 5302–5317. <https://doi.org/10.1002/2015JC010901>
2450
- 2451 McWilliams, J. C., 1996. Modeling the Oceanic general circulation. *Annual Review of Fluid*
2452 *Mechanics*, 28(1), 215- 248.
2453
- 2454 Miller, J.R., 1976. The salinity effect in a mixed layer ocean model. *J. Phys. Oceanogr.*, 6, 29–
2455 35.
2456
- 2457 Mignot, J., de Boyer Montégut, C., Lazar, A., Cravatte, S., 2007. Control of salinity on the
2458 mixed layer depth in the world ocean: 2. Tropical areas. *J. Geophys. Res.*
2459 112. doi:10.1029/2006JC003954
2460
- 2461 Miyama, T., McCreary Jr., J. P., Jensen, T. G., Loschnigg, J., Godfrey, J. S., Ishida, A., 2003.
2462 Structure and dynamics of the Indian-Ocean cross equatorial cell, *Deep Sea Res.*, 50, 2023–2047.
2463
- 2464 Momin, I.M., Mitra, A.K., Mahapatra, D.K., Gera, A., Rajagopal, E.N., 2014. Impact of model
2465 resolutions on Indian ocean simulations from Global NEMO Ocean Model. *Ind. J. of Geo-*
2466 *Marine Sc.*, Vol.43(09), 1667-1674
2467
- 2468 Moshonkin, S. M., Harenduprakash, L. 1991. Effect of salinity and transparency on the mixed
2469 layer thermal structure in the Bay of Bengal, *Oceanology*, 31, 384–394.
2470
- 2471 Murtugudde, R., Seager, R., Busalacchi, A., 1996. Simulation of the Tropical Oceans with an
2472 ocean GCM coupled to an atmospheric mixed layer model, *J. Clim.*, 9, 1795–1815.

- 2473
- 2474 Murtugudde, R., Busalacchi, A.J., 1999. Interannual Variability of the Dynamics and
2475 Thermodynamics of the Tropical Indian Ocean. *J. Clim.* 12, 2300–2326.
2476 [https://doi.org/10.1175/1520-0442\(1999\)012<2300:IVOTDA>2.0.CO;2](https://doi.org/10.1175/1520-0442(1999)012<2300:IVOTDA>2.0.CO;2)
2477
- 2478 Murtugudde, R., Busalacchi, A.J., Beauchamp, J., 1998. Seasonal-to-interannual effects of the
2479 Indonesian throughflow on the tropical Indo-Pacific Basin. *J. Geophys. Res. Oceans* 103, 21425–
2480 21441. <https://doi.org/10.1029/98JC02063>
2481
- 2482 Murtugudde, R., McCreary, J., Busalacchi, A. J., 2000. Oceanic processes associated with
2483 anomalous events in the Indian Ocean with relevance to 1997-98. *J. Geophys. Res.*, 105, 3295-
2484 3306.
2485
- 2486 Murty, V.S., Sarma, Y.V., Babu, M.T., Rao, D.P., 1992. Hydrography and circulation in the
2487 northwestern Bay of Bengal during the retreat of southwest monsoon. *J. Earth Syst. Sci.* 101, 67–
2488 75.
2489
- 2490 Nagura, M., Sasaki, W., Tozuka, T., Luo, J.-J., Behera, S.K., Yamagata, T., 2013. Longitudinal
2491 biases in the Seychelles Dome simulated by 35 ocean-atmosphere coupled general circulation
2492 models. *J. Geophys. Res. Oceans* 118, doi:10.1029/2012JC008352
2493
- 2494 Narapusetty, B., Murtugudde, R., Wang, H., Kumar, A., 2015. Ocean–atmosphere processes
2495 driving Indian summer monsoon biases in CFSv2 hindcasts. *Clim Dyn.* doi: 10.1007/s00382-
2496 015-2910-9
2497
- 2498 Nauw, J. J., van Aken, H. M., Webb, A., Lutjeharms, J. R. E., de Ruijter, W. P. M., 2008.
2499 Observations of the southern East Madagascar Current and undercurrent and countercurrent
2500 system, *J. Geophys. Res.*, 113, C08006, doi:10.1029/2007JC004639.

- 2501
2502 Oberhuber, J. M., 1988. An atlas based on the COADS data set: The budgets of heat, buoyancy
2503 and turbulent kinetic energy at the surface of the global ocean. Max-Planck-Institut für
2504 Meteorologie Tech. Rep. 15, 20 pp. [Available from Max-Planck-Institut für Meteorologie,
2505 Bundesstrasse 55, 20146 Hamburg, Germany.
2506
- 2507 Palastanga, V., van Leeuwen, P., de Ruijter, W., 2006. A link between low-frequency mesoscale
2508 eddy variability around Madagascar and the large-scale Indian Ocean variability, *J. Geophys.*
2509 *Res.*, 111, C09,029, doi:10.1029/2005JC003081.
- 2510 Palastanga, V., van Leeuwen, P. J., Schouten, M. W., de Ruijter, W. P. M., 2007. Flow structure
2511 and variability in the subtropical Indian Ocean: Instability of the South Indian Ocean
2512 Countercurrent, *J. Geophys. Res.*, 112, C01001, doi:10.1029/2005JC003395.
- 2513
- 2514 Parampil, S., Bharathraj, G. N., Harrison, M., Sengupta, D., 2016. Observed subseasonal
2515 variability of heat flux and the SST response of the tropical Indian Ocean, *J. Geophys. Res.*
2516 *Oceans*, 121, 7290–7307, doi:10.1002/2016JC011948.
2517
- 2518 Parekh, A., Gnanaseelan, C., Jayakumar, A. 2011. Impact of improved momentum transfer
2519 coefficients on the dynamics and thermodynamics of the north Indian Ocean. *J Geophys Res*
2520 116:C01004. doi: 10.1029/2010JC006346
2521
- 2522 Perigaud, C., McCreary, J.P., Zhang, K.Q., 2003. Impact of interannual rainfall anomalies on
2523 Indian Ocean salinity and temperature variability. *J. Geophys. Res. Oceans* 108 (C10), 3319.
2524 <http://dx.doi.org/10.1029/2002JC001699>
2525
- 2526 Perez-Hernandez, M.D., Hernandez-Guerra, A., Joyce, T.M., Velez-Belchi, P., 2012. Wind-
2527 driven cross-equatorial flow in the Indian Ocean. *J. Phys. Oceanogr.*, 42, 2234-2253.
2528

- 2529 Philander, S. G. H., 1973. Equatorial undercurrent: Measurements and theories, *Rev.*
2530 *Geophys.*, 11(3), 513–570, doi:10.1029/RG011i003p00513.
- 2531
- 2532 Philander, S. G. H., Pacanowski, R. C., 1980. The generation of equatorial currents, *J. Geophys.*
2533 *Res.*, 85, 1123–1136
- 2534
- 2535 Pokhrel S, Chaudhari, H.S, Saha, S.K, Dhakate, A., Yadav, R.K., Salunke, K., Mahapatra, S.,
2536 Rao, S.A., 2012a. ENSO, IOD and Indian summermonsoon in NCEP climate forecast system.
2537 *Clim Dyn* 1–23. doi: 10.1007/s00382-012-1349-5
- 2538
- 2539 Pokhrel S., Rahaman, H., Parekh, A., Saha, S.K., Dhakate, A., Chaudhari, H.S., Gairola, R.M.,
2540 2012b. Evaporation–precipitation variability over Indian Ocean and its assessment in NCEP
2541 Climate Forecast System (CFSv2). *Clim. Dyn.* 39:2585–2608.
- 2542
- 2543 Pokhrel, S., Saha, S. K., Dhakate, A., Chaudhari, H. S., Salunke, K., Rahman, H., Krishna, S.,
2544 Hazra, A., Sikka, D. R. 2016. Seasonal prediction of Indian summermonsoon rainfall in NCEP
2545 CFSv2: Forecast and predictability error. *ClimDyn*, 46, 2305–
2546 2326. <https://doi.org/10.1007/s00382-015-2703-1>
- 2547
- 2548 Ponsoni, L., Aguiar-Gonzalez, B., Ridderinkhof, H., Maas, L. R. M., 2016. The East
2549 Madagascar Current: Volume Transport and Variability Based on Long-Term Observations. *J.*
2550 *Phys. Oceanogr.* 46(4), 1045–1065. <https://doi.org/10.1175/JPO-D-15-0154.1>
- 2551
- 2552 Prasanna, V., 2015. Regional climate change scenarios over South Asia in the CMIP5 coupled
2553 climate model simulations. *Meteorog. Atmos. Phys.* 127:561–578. doi: 10.1007/s00703-015-
2554 0379-z
- 2555

- 2556 Premkumar, K., Ravichandran, M., Kalsi, S. R., Sengupta, D., Gadgil, S., 2000. First results from
2557 a new observational system over the Indian seas, *Curr. Sci.*, 78, 323–331.
- 2558
- 2559 Praveen Kumar, B., Vialard, J., Lengaigne, M., Murty, V.S.N., McPhaden, M.J., Cronin, M.F.,
2560 Pinsard, F., Gopala Reddy, K., 2013. TropFlux wind stresses over the tropical oceans: evaluation
2561 and comparison with other products. *Clim. Dyn.* 40, 2049–2071. [https://doi.org/10.1007/s00382-](https://doi.org/10.1007/s00382-012-1455-4)
2562 012-1455-4
- 2563
- 2564 Qiu, B., Chen, S., Hacker, P., 2004. Synoptic-scale air–sea flux forcing in the western North
2565 Pacific: Observations and their impact on SST and the mixed layer. *J. Phys. Oceanogr.* 34, 2148–
2566 2159.
- 2567
- 2568 Qu, T., Meyers, G., Godfrey, J. S., Hu, D. X., 1994. Ocean dynamics in the region between
2569 Australia and Indonesia and its influence on the variation of sea surface temperature in a global
2570 general circulation model, *J. Geophys. Res.*, 99, 18,433–18,445.
- 2571
- 2572 Qiu, B., Chen, S., Hacker, P., 2004. Synoptic-scale air–sea flux forcing in the western North
2573 Pacific: Observations and their impact on SST and the mixed layer. *J. Phys. Oceanogr.* 34,
2574 2148–2159.
- 2575
- 2576 Rahaman, H., Ravichandran, M., Sengupta, D., Harrison, M.J., Griffies, S.M.,
2577 2014. Development of a regional model for the north Indian Ocean. *Ocean Model.* 75 1–19.
- 2578
- 2579 Rahaman, H., Ravichandran, M., 2013. Evaluation of near-surface air temperature and specific
2580 humidity from hybrid global products and their impact on latent heat flux in the North Indian
2581 Ocean: . *J. Geophys. Res. Oceans* 118, 1034–1047. doi:10.1002/jgrc.20085
- 2582

- 2583 Rajeevan, M., Unnikrishnan, C.K., Preethi, B., 2012. Evaluation of the ENSEMBLES multi-
2584 model seasonal forecasts of Indian summer monsoon variability. *Clim. Dyn.* 38 (11-12), 2257-
2585 2274.
- 2586
- 2587 Rajeevan, M., Pai, D.S., Kumar, R.A., Lal, B., 2007. New statistical models for long-range
2588 forecasting of southwest monsoon rainfall over India. *Clim. Dyn.* doi: 10.1007/s00382-006-
2589 019706.
- 2590
- 2591 Rao, R. R., Sanil Kumar, K. V., 1991. Evolution of salinity field in the upper layers of the east
2592 central Arabian Sea and northern Bay of Bengal during summer monsoon experiments, *Proc.*
2593 *Indian Acad. Sci.*, 100, 69–78, 1991.
- 2594
- 2595 Rao, R.R., Molinari, R. L., Festa, J. F., 1991. Surface meteorological and subsurface
2596 oceanographic atlas of the tropical Indian Ocean. NOAA Tech. Memor. ERL-AOML-69, 59pp.
- 2597
- 2598 Rao, R. R., Sivakumar, R., 1999. On the possible mechanisms of the evolution of a mini-warm
2599 pool during the pre-summer monsoon season and the onset vortex in the southeastern Arabian
2600 Sea, *Q. J. R. Meteorol. Soc.*, 125, 787– 809.
- 2601
- 2602 Rao, R.R., Jitendra, V., Girish Kumar, M.S., Ravichandran, M., Ramakrishna, S.S.V.S., 2015.
2603 Interannual variability of the Arabian Sea Warm Pool: observations and governing mechanisms.
2604 *Clim. Dyn.* 44, 2119–2136. doi:10.1007/s00382-014-2243-0
- 2605
- 2606 Rao, R.R., Sivakumar, R., 2000. Seasonal variability of the heat budget of the mixed layer and
2607 the near-surface layer thermal structure of the tropical Indian Ocean from a new global ocean
2608 temperature climatology. *J. Geophys. Res.* 105, 995– 1015.
- 2609

- 2610 Rao, R.R., Sivakumar, R., 2003. Seasonal variability of sea surface salinity and salt budget of the
2611 mixed layer of the north Indian Ocean. *J. Geophys. Res.* 108 (C1), 3009.
2612 <http://dx.doi.org/10.1029/2001JC000907>
2613
- 2614 Rao, R.R., 2015. Observed variability of near-surface salinity field on seasonal and interannual
2615 time scales and its impact on the evolution of sea surface temperature of the tropical Indian
2616 Ocean. *Int. J. Ocean Clim. Syst.* 6, 87–111.
2617
- 2618 Rao, R. R., Ramakrishna, S.S.V.S., 2017. Observed seasonal and interannual variability of the
2619 near-surface thermal structure of the Arabian Sea Warm Pool, *Dyn. of Atmospheres*
2620 *Oceans*, Vol.78,2017,121-136,<https://doi.org/10.1016/j.dynatmoce.2017.03.001>.
2621
2622
- 2623 Reppin, J., F. Schott, Fischer, J., 1999. Equatorial currents and transports in the upper central
2624 Indian Ocean: Annual cycle and interannual variability, *J. Geophys. Res.*, 104(C7), 15,495–
2625 15,514.
2626
- 2627 Reverdin, G. 1985. Convergence in the equatorial surface jets of the Indian Ocean. *J. Geophys.*
2628 *Res.* 90.[doi: 10.1029/JC080i014p11741](https://doi.org/10.1029/JC080i014p11741). issn: 0148-0227.
2629
- 2630 Reynolds, R.W., Rayner, N.A., . Smith, T.M., Stokes, D.C., Wang, W., 2002. An improved in
2631 situ and satellite SST analysis for climate. *J. Clim.*, 15, 1609-1625.
2632
- 2633 Ridderinkhof, W., Le Bars,D., von der Heydt, A. S., de Ruijter, W. P. M., 2013. Dipoles of the
2634 South East Madagascar Current. *Geophys. Res. Lett.*, **40**, 558–562,
2635 [doi:https://doi.org/10.1002/grl.50157](https://doi.org/10.1002/grl.50157).

- 2636 Roxy M., Tanimoto, Y., Preethi, B., Terray, P., Krishnan, R., 2012. Intraseasonal SST-
2637 precipitation relationship and its spatial variability over the tropical summer monsoon
2638 region. *Clim Dyn*, 41 (1), 45-61.
- 2639
- 2640 Rochford, D.J., 1964. Salinity maxima in the upper 1000 metres of the North Indian Ocean. *Aust*
2641 *J Mar Freshw Res* 15:1–24
- 2642
- 2643 Saha, S. K., Hazra, A., Pokhrel, S., Chaudhari, H. S., Sujith, K., Rai, A., Rahaman, H.,
2644 Goswami, B. N., 2019. Unraveling the mystery of Indian summer monsoon prediction: Improved
2645 estimate of predictability limit. *J. Geophys. Res. Atmos.*, 124, 1962–1974.
2646 <https://doi.org/10.1029/2018JD030082>
- 2647
- 2648 Sahai, A.K., Mandke, S.K., Shinde, M.A., Chattopadhyay, R., Joseph, S., Goswami, B.N., 2007.
2649 Experimental seasonal forecast of Indian summer monsoon 2007: statistical and dynamical
2650 models. *Res Rep RR 120*.
- 2651
- 2652 Saji, N.H., Xie, S.P., Yamagata, T., 2006. Tropical Indian Ocean variability in the IPCC
2653 twentieth-century climate simulations. *J. Clim.* 19:4397–4417
- 2654
- 2655 Saji, N.H., Yamagata, T., 2003. Possible impacts of Indian Ocean dipole mode events on global
2656 climate. *Clim. Res.* 25(2):151–169
- 2657
- 2658 Saji, N.H., Goswami, B. N., Vinayachandran, P. N., Yamagata, T., 1999. A dipole mode in the
2659 tropical Indian Ocean. *Nature*, 401, 360-363.
- 2660 Sanchez-Franks, A., Kent, E. C., Matthews, A. J., Webber, B. G., Peatman, S. C.,
2661 Vinayachandran, P. N., 2018. Intraseasonal variability of air–sea fluxes over the Bay of Bengal
2662 during the southwest monsoon. *J. Clim.* 31(17), 7087-7109.

2663

- 2664 Sandeep, S., Ajayamohan, R.S., 2014. Origin of cold bias over the Arabian Sea in Climate
2665 Models. *Sci. Rep.* 4, 6403. doi:10.1038/srep06403
2666
- 2667 Sastry, J.S., Rao, D.P., Murty, V.S.N., Sarma, Y.V.B., Suryanarayana, A., Babu, M.T., 1985.
2668 Watermass structure in the Bay of Bengal. *Mahasagar* 18:153–162
2669
- 2670 Sayantani, O., Gnanaseelan, C., Chowdary, J.S., Parekh, A., Rahul, S., 2016. Arabian Sea SST
2671 evolution during spring to summer transition period and the associated processes in coupled
2672 climate models: Arabian Sea SST biases in coupled climate models. *Int. J. Clim.* 36, 2541–2554.
2673 doi:10.1002/joc.4511
2674
- 2675 Schott, F., Swallow, J. C., Fieux, M., 1990. The Somali Current at the equator: Annual cycle and
2676 transports. *Deep Sea Res.*, 37A, 1825–1848
2677
- 2678 Schott, F., Dengler, M., Schoenefeldt, R., 2002a. The shallow overturning circulation of the
2679 Indian Ocean, *Prog. Oceanogr.*, 53, 57–103.
2680
- 2681 Schott, F., Dengler, M., Schoenefeldt, R., 2002b. Erratum to: The shallow overturning circulation
2682 of the Indian Ocean *Prog. Oceanogr.*, 55 . pp. 373-384. DOI 10.1016/S0079-6611(02)00117-9.
2683
- 2684 Schott, F.A., McCreary, J.P., 2001. The monsoon circulation of the Indian Ocean; *Prog.*
2685 *Oceanogr.* 51, 1–123.
2686
- 2687 Schott, F. A., McCreary, J. P., Johnson, G. C., 2004. Shallow overturning circulations of the
2688 tropical-subtropical oceans, in *Earth's Climate: The Ocean-Atmosphere Interaction*, *Geophys.*
2689 *Monogr. Ser.*, vol. 147, edited by C. Wang, S.-P. Xie, and J. A. Carton, pp. 261– 304, AGU,
2690 Washington, D. C.
2691

- 2692 Schott, F.A., Xie, S.-P., McCreary, J.P., 2009. Indian Ocean circulation and climate variability.
2693 Rev. Geophys. 47. doi:10.1029/2007RG000245
2694
- 2695 Seidel, H. F., Giese, B. S., 1999. Equatorial currents in the Pacific Ocean 1992–1997, J.
2696 Geophys. Res., 104(C4), 7849–7863, doi:10.1029/1999JC900036.
2697
- 2698 Sengupta, D., Raj, G.N.B., Shenoi, S.S.C., 2006. Surface freshwater from the Bay of Bengal
2699 runoff and Indonesian throughflow in the tropical Indian Ocean. Geophys. Res. Lett. 33
2700 (L22609), 2006G. <http://dx.doi.org/10.1029/L027573>.
2701
- 2702 Senan, R., Anitha, D. S., Sengupta, D., 2001. Validation of SST and WS from TRMM using
2703 north Indian Ocean moored buoy observations, CAOS Rep. 2001AS1, Cent. for Atmos. Sci.,
2704 Indian Inst. of Sci., Bangalore, India.
2705
- 2706 Shankar, D., Shenoi, S.S.C., Nayak, R.K., Vinayachandran, P.N., Nampoothiri, G.S., Almeida,
2707 A.M., Selvan, G., RameshKumar, M.R., Sundar, D., Sreejith, O.P., 2005. Hydrography of the
2708 eastern Arabian Sea during summer monsoon 2002. J Earth. Syst. Sci. 114:475–491
2709 doi: 10.1007/BF02702024
2710
- 2711 Shankar, D., Vinayachandran, P.N., Unnikrishnan, A.S., 2002. The monsoon currents in the
2712 north Indian Ocean. Prog. Oceanogr. 52, 63–120.
2713
- 2714 Sharma, R., Agarwal, N., Basu, S., Agarwal, V. K., 2007. Impact of satellite-derived forcings
2715 on numerical ocean model simulations and study of sea surface salinity variations in the Indian
2716 Ocean. *J. Clim.*, **20**, 871–890.
2717
- 2718 Sharma, R., Agarwal, N., Momin, I.M., Basu, S., Agarwal, V.K., 2010. Simulated Sea Surface
2719 Salinity Variability in the Tropical Indian Ocean. *J. Clim.* 23, 6542–6554.
2720 doi:10.1175/2010JCLI3721.

- 2721
2722 Shenoi, S.S.C., Shankar, D., Michael, G.S., Kurian, J., Varma, K.K., Ramesh Kumar, M.R.,
2723 Almeida, A.M., Unnikrishnan, A.S., Fernandes, W., Barreto, N., Gnanaseelan, C., Mathew, R.,
2724 Praju, K.V., Mahale, V., 2005. Hydrography and water masses in the southeastern Arabian Sea
2725 during March–June 2003. *J Earth Syst Sci* 114(5):475–491
2726
- 2727 Shenoi, S.S.C., Shankar, D., Shetye, S., 1999. On the seas surface temperature high in the
2728 Lakshadweep Sea before the onset of the summer monsoon. *J. Geophys. Res.* 104(C7):15703–
2729 15712
2730
- 2731 Shenoi, S.S.C., Shetye, S.R., Gouveia, A.D., Michael, G.S., 1993. Salinity extrema in the
2732 Arabian Sea. In: Ittekkot V, Nair RR (eds) *Monsoon biogeochemistry*, *Mitteilungen des*
2733 *Geologisch-Paläontologischen Instituts der Universität Hamburg*, University of Hamburg,
2734 Germany, pp 37–49
2735
- 2736 Shenoi, S.S.C., Shankar, D., Shetye, S.R., 2002. Differences in heat budgets of the near-surface
2737 Arabian Sea and Bay of Bengal: implications for the summer monsoon. *J. Geophys. Res.* 107
2738 (C6), 3052. <http://dx.doi.org/10.1029/2000JC000679>
2739
- 2740 Shenoi, S.S.C., Shankar, D., Shetye, S.R., 2004. Remote forcing annihilates barrier layer in
2741 southeastern Arabian Sea. *Geophys. Res. Lett.* 31.
2742
- 2743 Shetye, S.R., Gouveia, A.D., Shenoi, S.S.C., 1994. Circulation and water masses of the Arabian
2744 Sea. *Proc Indian Acad Sci (Earth Planet Sci)* 103:107–123.[doi:10.1007/BF02839532](https://doi.org/10.1007/BF02839532)
2745
- 2746 Shetye, S.R., Gouveia, A.D., Shankar, D., Shenoi, S.S.C., Vinayachandran, P.N., Sundar, D.,
2747 Michael, G.S., Nampoothiri, G., 1996. Hydrography and circulation in the western Bay of
2748 Bengal during the northeast monsoon. *J. Geophys. Res.* 101 (C6), 14,011–14,025.
2749

- 2750 Shetye, S.R., Gouveia, A.D., Shankar, D., Shenoi, S.S.C., Vinayachandran, P.N., Sundar, D.,
2751 Michael, G.S., Nampoothiri, G., 1996. Hydrography and circulation in the western Bay of
2752 Bengal during the northeast monsoon. *J. Geophys. Res.* 101 (C6), 14,011–14,025.
2753
- 2754 Siedler, G., Rouault, M., Biastoch, A., Backeberg, B., Reason, C., Lutjeharms, J., 2009. Modes of
2755 the southern extension of the East Madagascar Current, *J. Geophys. Res.*, 114,
2756 doi:10.1029/2008JC004921.
- 2757
- 2758 Singh, S., Valsala, V., 2018. Role of Subsurface ocean bias in coupled models in simulated
2759 interannual variability: A case study for Indian Ocean. *Dyn. Atmos and Ocean*,
2760 doi.org/10.1016/j.dynatmoce.2018.10.001.
- 2761
- 2762 Sitz, L. E., Sante, F., Farneti, R., Fuentes-Franco, R., Coppola, E., Mariotti, L., Reale, M., et
2763 al., 2017. Description and Evaluation of the Earth System Regional Climate Model (RegCM–
2764 ES). *Journal of Advances in Modeling Earth Systems*. doi:10.1002/2017MS000933
2765
- 2766 Sperber, K.R., Palmer, T.N., 1996. Interannual tropical rainfall variability in general circulation
2767 model simulations associated with the atmospheric model intercomparison project. *J Clim*
2768 9:2727–2750.
2769
- 2770 Sprintall, J., Tomczak, M., 1992. Evidence of the barrier layer in the surface layer of the tropics,
2771 *J. Geophys. Res.*, 97, 7305–7316
2772
- 2773 Srinivasu U., Ravichandran, M., Han, W., Sivareddy, S., Rahaman, H., Nayak, S., 2017. Causes for
2774 decadal reversal of North Indian Ocean sea level in recent two decades *Clim. Dyn.* (2017).
2775 doi:10.1007/s00382-017-3551-y
2776

- 2777 Stull R, Meteorology for Scientists and Engineers, 3rd Edition, 2011.
2778
- 2779 Stocker, T.F., Qin,D., Plattner,G.-K., Tignor, M., Allen, S.K., Boschung, J., Nauels,A., Xia, Y.,
2780 Bex, V., Midgley P.M., (eds.) IPCC, 2013. Climate Change 2013: The Physical Science Basis.
2781 Contribution of Working Group I to the Fifth Assessment Report of the Intergovernmental Panel
2782 on Climate Change []. Cambridge University Press, Cambridge, United Kingdom and New York,
2783 NY, USA, 1535 pp.
- 2784
- 2785 Swallow, J. C., Equatorial Undercurrent in western Indian Ocean, *Nature*, 20•, 436-437, 1964.
2786
- 2787 Swallow, J.C., 1967. The Equatorial Undercurrent in the western Indian Ocean in 1964. *Studies*
2788 *in Tropical Oceanography*, no. 5, pp. 15-36, Univ. of Miami Press, Coral Gables, Fla., 1967
2789
- 2790 Swapna P.,Jyoti,J., Krishnan,R., Narayan Setti, S., Griffies, S.M., 2017. Multi-decadal
2791 weakening of Indian summer monsoon circulation induces an increasing northern Indian
2792 Ocean sea level. *Geophys. Res. Lett.*, October, 2017, doi: 10.1002/2017GL074706.
2793
- 2794 Swapna, P., Krishnan, R., Wallace, J., 2014.Indian Ocean and monsoon coupled interactions in a
2795 warming environment. *Clim. Dyn.* 42, 2439–2454.
2796
- 2797 Swain, D., Rahman, S.H., Ravichandran, M., 2009. Comparison of NCEP turbulent heat fluxes
2798 with in-situ observations over the south-eastern Arabian Sea. *Meteorol. Atmos. Phys.* 104:163–
2799 175. doi: 10.1007/s00703-009-0023-x
2800
- 2801 Sujith, K, Saha,S.K., Rai,A., Pokhrel,S., Chaudhari, H.S., Hazra,A., Murtugudde, R., Goswami,
2802 B.N., 2019.Effects of a multilayer snow scheme on the global teleconnections of the Indian
2803 summer monsoon. *Q J R Meteorol Soc.* 145: 1102- 1117.<https://doi.org/10.1002/qj.3480>

2804

- 2805 Tao W, Huang, G., Hu, K., Gong, H., Wen, G., Liu, L., 2015. A study of biases in simulation
2806 of the Indian Ocean basin mode and its capacitor effect in CMIP3/CMIP5 models. *Clim. Dyn.*
2807 doi: 10.1007/s00382-015-2579-0
2808
- 2809 Taylor, K.E., Stouffer, R.J, Meehl, G.A., 2012. An overview of CMIP5 and the experiment
2810 design. *Bull Am Meteorol Soc* 93(4):485–498. doi: 10.1175/BAMS-D-11-00094.1
2811
- 2812 Tseng, Y.-H., H. Lin; H.-C. Chen, K. Thompson, M. Bentsen, C. Boning, A. Bozec, C. Cassou,
2813 E. Chassignet, C. H. Chow, G. Danabasoglu, S. Danilov, R. Farneti, Y. Fujii, S. Griffies, M.
2814 Ilicak, T. Jung, S. Masina, A. Navarra, L. Patara, B. Samuels, M. Scheinert, D. Sidorenko, C.-H
2815 Sui, H. Tsujino, S. Valcke, A. Voldoire, Q. Wang. North and Equatorial Pacific Ocean
2816 Circulation in the CORE-II Hindcast Simulations. (2017), *Ocean Modelling* 104 (2016) 143–170
2817
- 2818 Thadathil, P., Muraleedharan, P.M., Rao, R.R., Somayajulu, Y.K., Reddy, G.V., Revichandran,
2819 C., 2007. Observed seasonal variability of barrier layer in the Bay of Bengal. *J. Geophys. Res.* 112
2820 (C2), C02009.
2821
- 2822 Thangaprakash, V. P., Girishkumar, M. S., Suprit, K., Sureshkumar, N., Dipanjan, C., Dinesh, K.,
2823 Ashok, K., Shivaprasad, S., Ravichandran, M., Thomas Farrar, J., Sundar, N., Weller, R.A., 2015.
2824 What controls seasonal evolution of SST in the Bay of Bengal? Mixed layer heat budget analysis
2825 using Moored buoy observations along 90°E. *Oceanography* 29(2):202-213,
2826 <http://dx.doi.org/10.5670/oceanog.2016.52>.
2827
- 2828 Tozuka T, Cronin, M.F., Tomita, H., 2017. Surface frontogenesis by surface heat fluxes in the
2829 upstream Kuroshio Extension region. *Sci Rep* 7:10258
2830
- 2831 Tsujino, H., Shogo, U., Nakano, H., Small, R. J., Kim, W.M., Yeager, S. G., Danabasoglu, G.,
2832 Suzuki, T., Bamber, J. L., Bentsen, M., Böning, C.W., Bozec, A., Chassignet, E.P., Curchitser, E.,
2833 Dias, F. B., Durack, P.J., Griffies, S. M., Harada, Y., Ilicak, M., Josey, S. A., Kobayashi, C.,

- 2834 Kobayashi,S., Komuro,Y., Large,W.G., Sommer,J.L., Marsland,S. J., Masina,S., Scheinert,M.,
2835 Tomita,H., Valdivieso, M., Yamazaki,D., 2018. JRA-55 based surface dataset for driving ocean–
2836 sea-ice models (JRA55-do), *Ocean Model.*,130,2018,79-
2837 139,<https://doi.org/10.1016/j.ocemod.2018.07.002>.
2838
- 2839 Varadachari, V.V.R., Murty, C.S., Reddy, C.V.G., 1968. Salinity maxima associated with some
2840 sub-surface water masses in the upper layers of the Bay of Bengal. *Bull. Natl. Inst. Sci. India*
2841 38:338–343
2842
- 2843 Venugopal T and Hasibur Rahaman, (2019) Evaluation of hybrid and satellite derived surface
2844 downwelling shortwave and long wave radiation over tropical global oceans.
2845 *SN Appl. Sci.* (2019) 1: 1171. <https://doi.org/10.1007/s42452-019-1172-2>
2846
- 2847 Vialard, J., Duvel, J.-P., Mcphaden, M.J., Bouruet-Aubertot, P., Ward, B., Key, E., Bourras, D.,
2848 Weller, R.A., Minnett, P., Weill, A., others, 2009. Cirene: air-sea Interactions in the Seychelles-
2849 Chagos thermocline ridge region. *Bull. Am. Meteorol. Soc.* 90:45–61
- 2850 Vialard, J., Jayakumar, A., Gnanaseelan, C., Lengaigne, M., Sengupta, D., Goswami, B. N.,
2851 2012. Processes of 30–90 days sea surface temperature variability in the northern Indian Ocean
2852 during boreal summer. *Clim.Dyn.* 38(9-10), 1901-1916.
- 2853
- 2854 Vinayachandran, P. N., Shetye, S. R., 1991. The warm pool in the Indian Ocean, *Proc. Indian*
2855 *Acad. Sci. (Earth Planet. Sci.)*, 100(2), 165–175.
2856
- 2857 Vinayachandran, P. N., Masumoto, Y., Mikawa, T., Yamagata, T., 1999. Intrusion of the Southwest
2858 Monsoon Current into the Bay of Bengal, *J. Geophys. Res.*, 104(C5), 11077–11085,
2859 doi:10.1029/1999JC900035.
2860

- 2861 Vinayachandran, P.N., Murty, V.S.N., Ramesh Babu, V., 2002. Observations of barrier layer
2862 formation in the Bay of Bengal during summer monsoon: barrier layer in the bay of bengal. *J.*
2863 *Geophys. Res. Oceans* 107, SRF 19-1-SRF 19-9. doi:10.1029/2001JC000831
2864
- 2865 Vinayachandran, P.N., Nanjundiah, R.S., 2009. Indian Ocean sea surface salinity variations in a
2866 coupled model. *Clim. Dyn.* 33, 245–263. doi:10.1007/s00382-008-0511-6
2867
- 2868 Vipin, P., Sarkar, K., Aparna, S.G., Shankar, D., Sarma, V.V.S.S., Gracias, D.G., Krishna, M.S.,
2869 Srikanth, G., Mandal, R., Rama Rao, E.P., Srinivasa Rao, N., 2015. Evolution and sub-surface
2870 characteristics of a sea-surface temperature filament and front in the northeastern Arabian Sea
2871 during November–December 2012. *J. Mar. Syst.* 150, 1–11. doi:10.1016/j.jmarsys.2015.05.003
2872
- 2873 Wacongne, S., Pacanowski, R.C., 1996. Seasonal heat transport in a primitive equation model of
2874 the tropical Indian Ocean, *J. Phys. Oceanogr.*, 26, 2666–2699.
2875
- 2876 Wang, H., Murtugudde, R., Kumar, A., 2016. Evolution of Indian Ocean dipole and its forcing
2877 mechanisms in the absence of ENSO, *Clim. Dyn.* 47 (7), 2481-2500.
2878
- 2879 Wang, X., Wang, C., 2014. Different impacts of various El Niño events on the Indian Ocean
2880 dipole. *Clim. Dyn.*, 42, 991–1005, doi:https://doi.org/10.1007/s00382-013-1711-2.
2881
- 2882 Wang, Y., McPhaden, M. J., 2017. Seasonal cycle of cross-equatorial flow in the central Indian
2883 Ocean, *J. Geophys. Res. Oceans*, 122, 3817–3827, doi:10.1002/2016JC012537.
2884
- 2885 Warren, B. A., 1981. Transindian hydrographic section at Lat. 18S: Property distributions and
2886 circulation in the South Indian Ocean, *Deep Sea Res., Part A*, 28, 759 – 788.
2887
- 2888 Waite, A. M., Thompson, P. A., Pesant, S., Feng, M., Beckley, L. E., Domingues, C. M.,
2889 Gaughan, D., Hanson, C. E., Holl, C. M., Koslow, T., Mueleners, M., Montoya, J. P., Moore, T.,

- 2890 Muhling, B. A., Paterson, H., Rennie, S., Strzelecki, J., Twomey, L., 2007. The Leeuwin Current
2891 and its eddies: An introductory overview. *Deep-Sea Research II* 54: 789–
2892 796. doi:10.1016/j.dsr2.2006.12.008
- 2893
- 2894 Webster, P.J., Andrew M. Moore, Johannes P. Loschnigg, D.N., Robert R., L., 1999. Coupling
2895 strength of charge carriers to spin fluctuations in high-temperature superconductors. *Nature* 401,
2896 354–356.
- 2897
- 2898 Webster, P.J., Magaña, V.O., Palmer, T.N., Shukla, J., Tomas, R.A., Yanai, M., Yasunari, T.,
2899 1998. Monsoons: Processes, predictability, and the prospects for prediction. *J. Geophys. Res.*
2900 *Oceans* 1978–2012 103, 14451–14510. doi:10.1029/97JC02719.
- 2901
- 2902 Weller, R. A., Anderson, S. P., 1996. Surface meteorology and air-sea fluxes in the western
2903 equatorial Pacific warm pool during the TOGA Coupled Ocean-Atmosphere Response
2904 Experiment, *J. Clim.*, 9, 1959-1990.
- 2905
- 2906 Wyrki, K., 1973. An equatorial jet in the Indian Ocean. *Science* 181, 262–264.
- 2907
- 2908 Xie, S-P., Annamalai, H., Schott, F.A., McCreary, J.P., 2002. Structure and mechanisms of South
2909 Indian Ocean climate variability. *J. Clim.* 15:864–878
- 2910
- 2911 Xie S.P., Hu, K., Hafner, J., Tokinaga, H., Du, Y., Huang, G., Sampe, T., 2009. Indian Ocean
2912 capacitor effect on Indo-western Pacific Climate during the summer following El Niño. *J.*
2913 *Clim.* 22: 730–747.
- 2914 Yamagami, Y., Tozuka, T., 2015. Interannual variability of South Equatorial Current bifurcation
2915 and western boundary currents along the Madagascar coast, *J. Geophys. Res. Oceans*, 120, 8551-
2916 8570, doi:10.1002/2015JC011069.

2917

- 2918
2919 Yang, J., Liu, Q., Xie, S.-P., Liu, Z., Wu, L., 2007. Impact of the Indian Ocean SST basin mode
2920 on the Asian summer monsoon. *Geophys. Res. Lett.* 34. doi:10.1029/2006GL028571
2921
2922 Yokoi, T., Tozuka, T., Yamagata, T., 2012. Seasonal and interannual variations of the SST
2923 above the Seychelles Dome. *J. Clim.* 25:800–814
2924
2925 Yokoi, T., Tozuka, T., Yamagata, T., 2008. Seasonal variation of the Seychelles Dome. *J. Clim.*,
2926 21, 3740–3754.
2927
2928 Yokoi, T., Tozuka, T., Yamagata, T., 2009. Seasonal Variations of the Seychelles Dome
2929 Simulated in the CMIP3 Models. *J. Phys. Oceanogr.* 39, 449–457. doi:10.1175/2008JPO3914.1
2930
2931 Yu, L., 2011. A global relationship between the ocean water cycle and near-surface salinity. *J.*
2932 *Geophys. Res.* 116. doi:10.1029/2010JC006937
2933
2934 Yu, L., Jin, X., Weller, R.A., 2007. Annual, Seasonal, and Interannual Variability of Air–Sea
2935 Heat Fluxes in the Indian Ocean. *J. Clim.*, Special issue on the Climate Variability and
2936 Predictability of the Indian Ocean, 20, 3190–3209.
2937
2938 Zhang, K.Q., Marotzke, J., 1999. The importance of open-boundary estimation for an Indian
2939 Ocean GCM-data synthesis. *J. Mar. Res.* 57, 305–334.

2940

2941 Conflict of Interest

2942 The authors declare that they have no conflict of interest associated with this publication.

2943 Highlights:

- 2944 • Assessment of the Indian Ocean mean state and seasonal cycle from 16 global forced sea-
2945 ice model.

- 2946
- 2947
- 2948
- 2949
- 2950
- 2951
- 2952
- 2953
- Sea Surface Temperature biases are ~2 times smaller in forced simulations than the coupled simulations.
 - Coupled model shows large inter-model spread over the eastern equatorial Indian Ocean.
 - Refinement in model horizontal resolution does not significantly improve simulations.
 - Uncover a secondary pathway of northward cross-equatorial transport along 75 °E in the Indian Ocean.
 - All models are unable to capture the observed thick barrier layer over the north Bay of Bengal.

2954

2955

2956